Atomistic Simulation of Fluid Structure and Diffusion in Functionalized Mesoporous Silica

Von der Fakultät Energie-, Verfahrens- und Biotechnik der Universität Stuttgart und dem Stuttgart Center for Simulation Science (SC SimTech) zur Erlangung der Würde eines Doktors der Ingenieurwissenschaft (Dr.-Ing.) genehmigte Abhandlung

Vorgelegt von
Hamzeh Kraus
aus Aidlingen

Hauptberichter: Prof. Dr.-Ing. Niels Hansen
Mitberichter: Prof. Dr.-Ing. Andreas Heyden

Tag der mündlichen Prüfung: 07.07.2023

Institut für Technische Thermodynamik und Thermische Verfahrenstechnik der Universität Stuttgart

2023

EIDESSTATTLICHE ERKLÄRUNG

Hiermit versichere ich, dass ich die vorliegende Arbeit mit dem Titel

„Atomistic Simulation of Fluid Structure and Diffusion in Functionalized Mesoporous Silica“

selbstständig verfasst und keine anderen als die angegebenen Quellen und Hilfsmittel benutzt habe, dass alle Stellen der Arbeit, die wörtlich oder sinngemäß aus anderen Quellen übernommen wurden, als solche kenntlich gemacht sind.
Ich versichere außerdem, dass die vorliegende Dissertation nur in diesem und keinem anderen Promotionsverfahren eingereicht wurde und dass diesem Promotionsverfahren keine endgültig gescheiterten Promotionsverfahren vorausgegangen sind.

I herewidth duly declare that I have authored the dissertation

“Atomistic Simulation of Fluid Structure and Diffusion in Functionalized Mesoporous Silica”

independently and only with use of specified aids. I have mentioned all sources used and cited correctly according to scientific rules.

Stuttgart,

Hamzeh Kraus

TABLE OF CONTENTS

ABSTRACT

Despite the importance of supported catalysts in industrial applications a rational design based on an understanding of molecular-level processes is still a challenging endeavor, in particular for liquid phase reactions. Ordered mesoporous silicas are common support materials for hosting organometallic catalysts and provide a tailored microenvironment that may lead to enhanced selectivities, productivities and activities. In the present work a computational tool box was developed that facilitates rapid model building of functionalized silica pores and, together with pre- and post-analysis tools, allows for systematic molecular simulation studies of confinement effects in various applications. The tool box was subsequently applied to different research questions including modelling of the uptake of aromatic compounds from the aqueous phase on cyclodextrin-functionalized silica and a detailed investigation of diffusion in cylindrical mesopores allowing to assess the discrepancy among recent experimental diffusion measurements.

KURZFASSUNG

Trotz der Bedeutung von Trägerkatalysatoren für industrielle Anwendungen ist ein rationales Design auf der Grundlage eines Verständnisses der Prozesse auf molekularer Ebene immer noch ein schwieriges Unterfangen, insbesondere bei Flüssigphasenreaktionen. Geordnete mesoporöse Siliziumdioxide sind gängige Trägermaterialien für metallorganische Katalysatoren und bieten eine maßgeschneiderte Mikroumgebung, die zu verbesserten Selektivitäten, Produktivitäten und Aktivitäten führen kann. In der vorliegenden Arbeit wurde eine computergestützte Toolbox entwickelt, die den schnellen Aufbau von Modellen funktionalisierter Siliziumdioxidporen erleichtert und zusammen mit Pre- und Post-Analyse-Tools systematische molekulare Simulationsstudien von Confinement-Effekten in verschiedenen Anwendungen ermöglicht. Die Toolbox wurde anschließend auf verschiedene Forschungsfragen angewandt, darunter die Modellierung der Aufnahme aromatischer Verbindungen aus der wässrigen Phase auf Cyclodextrin-funktionalisiertem Siliziumdioxid und eine detaillierte Untersuchung der Diffusion in zylindrischen Mesoporen, um die Diskrepanz zwischen den jüngsten experimentellen Diffusionsmessungen zu bewerten.

JOURNAL PUBLICATIONS

This thesis led to the following publications

- Chapter 2: H. Kraus, J. Rybka, A. Höltzel, N. Trebel, U. Tallarek and N. Hansen: PoreMS: a software tool for generating silica pore models with user-defined surface functionalisation and pore dimensions, *Molecular Simulation*, 47(4), 306-316, 2021
- Chapter 3: H. Kraus and N. Hansen: An atomistic view on the uptake of aromatic compounds by cyclodextrin immobilized on mesoporous silica, *Adsorption*, 28(3-4), 125-136, 2022
- Chapter 5: H. Kraus, M. Högler and N. Hansen: Axial diffusion in liquid-saturated cylindrical silica pore models, *The Journal of Physical Chemistry C*, DOI: 10.1021/acs.jpcc.3c01974

The chapters 2 and 3 present literal quotes of the published work. Any addition with respect to the published work is marked. Any deletion is indicated with square brackets as ‚[...]'. Chapter 5 represents a preliminary version of the published work. Crossreferences between chapters of this thesis, which are added to the published version of the text to increase readability, are marked by square brackets. The supporting informations to the single chapters are presented in the Appendix of this thesis.

Related publications:

- D. Markthaler, H. Kraus and N. Hansen: Overcoming Convergence Issues in Free-Energy Calculations of Amide-to-Ester Mutations in the Pin1-WW Domain, *Journal of Chemical Information and Modeling*, 58(11), 2305-2318, 2018
- J. Baz, J. Gebhardt, H. Kraus, D. Markthaler and N. Hansen: Insights into noncovalent binding obtained from molecular dynamics simulations, *Chemie Ingenieur Technik*, 90(11), 1864-1875, 2018
- B. Selent, H. Kraus, N. Hansen, B. Schembera, A. Seeland and D. Iglezakis, Management of Research Data in Computational Fluid Dynamics and Thermodynamics. In: Heuveline, V., Gebhart, F. and Mohammadianbisheh, N. (eds): *E-Science-Tage* 2019 – Data to Knowledge, Heidelberg: heiBOOKS, 2020, 128–139. DOI: 10.11588/heibooks.598.c8422
- F. Ziegler, J. Teske, I. Elser, M. Dyballa, W. Frey, H. Kraus, N. Hansen, J. Rybka, U. Tallarek and M. R. Buchmeiser: Olefin metathesis in confined geometries: a biomimetic approach toward selective macrocyclization, *Journal of the American Chemical Society*, 141(48), 19014-19022, 2019
- T. Kobayashi, H. Kraus, N. Hansen and M. Fyta: Confined Ru-catalysts in a two-phase heptane/ionic liquid solution: modeling aspects, *ChemCatChem*, 13(2), 739-746, 2021
- F. Ziegler, H. Kraus, M. J. Benedikter, D. Wang, J. R. Bruckner, M. Nowakowski, K. Weißer, H. Solodenko, G. Schmitz, M. Bauer, N. Hansen, and M. R. Buchmeiser: Confinement effects for efficient macrocyclization reactions with supported cationic molybdenum imido alkylidene n-heterocyclic carbene complexes, *ACS Catalysis*, 11(18), 11570–11578, 2021
- H. Kraus, J. Rybka, U. Tallarek and N. Hansen, Computational study of confinement effects in molecular heterogeneous catalysis. In: Nagel, W. E., Kröner, D. H., Resch, M. M. (eds): High Performance Computing in Science and Engineering '20, *Springer*, Cham, 2021.

- D. Markthaler, H. Kraus and N. Hansen: Binding free energies for the SAMPL8 CB8 “Drugs of Abuse” challenge from umbrella sampling combined with Hamiltonian replica exchange, *Journal of Computer-Aided Molecular Design*, 36(1), 1-9, 2022

ACKNOWLEDGEMENT

A doctoral thesis is an extensive effort demanding many crucial skills such as deep understanding, tenacity, and patience - of which almost none were present when I started on this odyssey, and at times their existence is still questionable. However, it is exactly this, that teaches humility and respect towards others on the same scientific journey. Especially towards my mentor Niels whose profound analytic insightfulness still amazes me, and I would like to thank him for his continuous and skillful help and guidance. Next to personal dedication, the work environment can be seen as the most important factor for any kind of profession. I did not realize how lucky I was with my coworkers, and took it for granted, until I heard what an actual awful workplace looks like. Therefore, I would also like to extend my gratitude to all my colleagues, especially Daniel, Gernot, and Julia, the latter from the Marburg University, whose advice and support was invaluable.

Since this work was carried out at a university institute, teaching students was a main assignment. An assignment for which I was excited, and one of the reasons I joined this institute. This excitement however turned into exhaustion once realizing what tutoring actually entails. Apart from time consuming organization and repeatedly answering the same student question, whether they can use a specific calculator, one recognizes the huge difference between understanding a subject, and understanding a subject well enough to teach. The latter requiring a strong foundation in the area and the ability to simplify a topic well enough, so someone without prior knowledge is able comprehend an explanation. It is often said, that if you cannot explain something in a simple way, your understanding is still lacking. During my student years, very few professors had this ability, one of which is our institute director Joachim, whom I consider a shining example for what it means to teach, and someone I admire deeply and tried to learn from as much as possible. The simplicity and excitement in his explanations was always intoxicating and made me fall in love with lecturing, which I will certainly miss. Hence, I would like to thank him for his teachings during both my student and doctoral years.

As for any well-behaved doctoral student, mentoring bachelor and master theses is an expected practice. Something I tried avoiding as much as possible, since it is an extensive amount of work, especially when picking the wrong people. Luckily, my two ~~slaves~~ students Marc and Maksim proved me mostly wrong and probably helped me more than I helped them, both from a knowledge and work basis, for which I am very thankful.

Finally, something that should have been the at the very top, I am deeply grateful to my dearest parents for providing me a home both, physically and emotionally, and for keeping me sane, during all these years.

1. Introduction

Catalytic reactions occurring in a directing confinement often show unexpected selectivities [1, 2], productivities and activities [3]. Typical inorganic mesoporous materials such as silicates or aluminosilicates are often used as confining support materials in either surface organometallic chemistry (SOMC) [4–8] or molecular heterogeneous catalysis (MHC), respectively [9–12]. The properties of fluid mixtures composed of solvent, reactant and product molecules within such tailored microenvironments and the local composition of reacting species around the catalytically active complex within the inner pore space are important factors determining the activity of catalytic reactions. Selectivity and conversion of reactions can be affected due to controlling the factors that influence the mobility of reactants and products including molecular size, shape, configuration, degree of confinement, pore topology, strength of adsorption on pore walls, and the possibility of hydrogen bonding between reactants or/and products. In the simplest case of MHC, the catalysis itself is not influenced by the support material, which then solely provides high surface area and facile removal. As compared to SOMC, catalyst loadings can often be increased at least by a factor of two. Provided that sufficiently long linkers are used the catalyst reacts in a so-called interphase, which, in a simplified way, can be understood as a solution-like environment [13, 14]. In this context, a layer of solvent molecules is relevant, which is no longer in direct contact ($\geq$ 1 nm distance) with the support, see Figure 1.1.1. According to the IUPAC definition [15] porous solids are referred to as mesoporous if the pore diameter is between 2 and 50 nm. However, confinement effects in MHC are particularly effective for pore diameters below 10 nm while a certain minimum diameter is required to allow for transport of bulky species [16, 17].

The discovery of the M41S family of silicate/aluminosilicate ordered mesoporous silica (OMS) with exceptionally large uniform pore structures at Mobil Corporation in 1992 has attracted increasing attention in multiple research areas [18]. By using micelles as templating agent, the preparation of solids with constant pore sizes in the range of 2 to 10 nm became possible [19]. However, M41S materials exhibit relatively low hydrothermal and mechanical stability [20]. A new family of OMS materials denoted as Santa Barbara Amorphous (SBA) was introduced in 1998 that demonstrated improved hydrothermal and mechanical stability [21–23]. Subsequently, a large number of materials with different compositions, symmetries, architectures and functionalities was developed [24]. Popular mesoporous silica materials, for which also verified synthesis recipes exist, exhibit pore sizes between 2 and 4 nm for MCM-41 and MCM-48 and between 4 and 8 nm for SBA-15 and SBA-16. Only for Al-SBA-15, pore diameters larger than 10 nm are reported in the verified synthesis recipes [25]. Thus, the range of accessible mesopore sizes is limited. In addition, the control of the pore size is often difficult.

By using a synthesis procedure referred to as “true liquid crystal templating” (TLCT) [26] the production of highly precise OMS materials is possible that exhibit straight, almost defect free pores, which increases the accessibility of the pores and facilitates the diffusion within [16]. This is reflected by a Gaussian pore width distribution and the absence of pores with deviating pore widths [27]. Therefore, OMS materials produced by TLCT are perfectly feasible to study confinement effects, which requires uniform pore widths.

The availability of a materials pool is a prerequisite for a systematic investigation of confinement effects [28, 29]. However, experimental studies alone do not provide sufficient high-resolution data to rationalize the effect of confinement on complex mixtures on a molecular basis. Thus, integral to the use and rational design of functionalized mesoporous materials is the existence of a model for predicting how pore dimension and surface functionalization influence the fluid properties under confinement. Fluids confined in mesoporous materials present a particular challenge to empirical tuning, as it is difficult to experimentally probe such properties as composition and phase behavior within the mesopores. For this reason, there is interest in computational modeling studies to provide a fundamental molecular-level description of the systems. The elementary steps involved in a catalytic process taking place under mesoporous confinement are illustrated in Figure 1.1.1. Several transport barriers and adsorption/desorption steps are taking place that are influenced in a complex manner by the fine structure of the porous material.

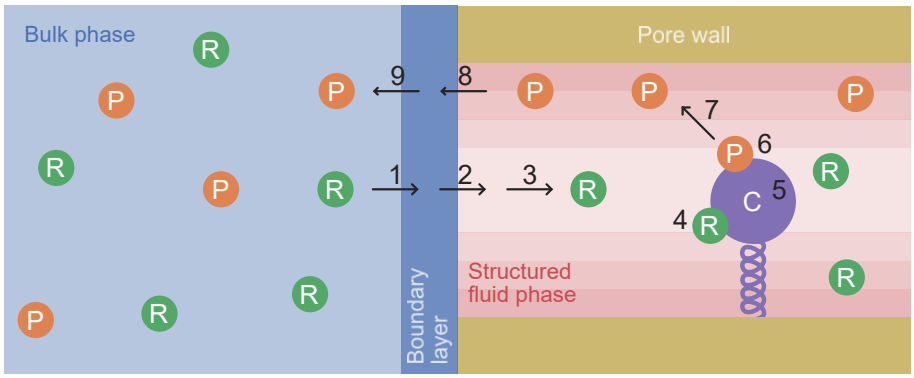

Figure 1.1.1.: Elementary steps in molecular heterogeneous catalysis in the liquid phase consisting of solvent, reactant (R) and product (P) molecules. (1) Mass transport through the boundary layer separating bulk and confined phase, (2) mass transport through the pore entrance and partitioning of bulk phase, (3) diffusion within the pore, (4) adsorption at the catalytically active complex (C), (5) catalytic reaction, (6) product desorption from the catalytically active complex, (7) product diffusion towards the pore entrance, (8) product exit, (9) product diffusion through the boundary layer into the bulk phase.

As opposed to e.g., zeolites, the structure of mesoporous silica materials is usually amorphous, so a suitable model is one that is representative from a statistical point of view, rather than correct atom by atom. X-ray diffraction (XRD) patterns reveal the average characteristic distances as the unit cell size of the regular structure, which are expressed as distinct peaks in X-ray powder diffraction patterns, but also information about pore diameters [30]. Agreement in the unit cell size is a fundamental requirement to model for periodic mesoporous silicas. X-ray results are usually interpreted with the aid of parametrized structural models, which give rise to a "best fit model" paradigm [31]. This indirect approach yields good qualitative and quantitative results when the behavior of the surface groups is reasonably well known and the structure arising at the interface is stable. However, with more complex systems and limited initial information on the expected structures, results can become ambiguous and several physically sound models, or several parametrizations of the same model, can be found to adequately describe the experimental data. Thus, although general features such as layer thickness are usually unambiguously described across the models, and can therefore be extracted with confidence, the detailed molecular structure of the interface is more difficult to obtain. In a recent study the

fundamental importance of the direct comparison between MD simulations with X-ray reflectivity measurements was demonstrated using an ionic liquid at a neutral sapphire interface as example. This comparison enabled one to use detailed description obtained from simulation with confidence [32]. Besides X-ray diffraction other characterization methods deliver useful structural information. ^{29}Si-nuclear magnetic resonance (NMR) spectroscopy measures the distribution of silicate tetrahedra with n bridging oxygens (shared between two tetrahedra), labelled as Q_n (n from 0 to 4), i.e., the connectivity of the silicon atoms in the silica network. Transmission electron microscopy (TEM) pictures are of help to reveal pore shape and regularity of mesoporous materials. The degree of realism of a model can further be investigated by its ability to predict experimental data such as adsorption isotherms of probe molecules. Adsorption experiments with different adsorptives give information about the porosity, the pore size distribution, the surface area, and surface chemistry. The agreement of experimental and simulated adsorption isotherms is a key criterion in the evaluation of the developed models for mesoporous materials. Multidimensional MAS NMR experiments provide information on the spatial arrangement of solvent molecules inside the pores [33]. However, regarding liquid phase processes in mesopores it is an open question of how close the structural model needs to be to reality in order to obtain sensible insight.

Mass transport of molecular compounds through porous solids is an important step in molecular heterogeneous catalysis. It is a multi-scale, hierarchical phenomenon: Macrodiffusion (> µm) is influenced, in addition to parameters like grain boundaries and particle packing, by meso-scale (>10 nm, < µm) factors like particle size and the connectivity of pores. More importantly, meso-scale diffusion and macro-scale diffusion are first and foremost determined directly by processes on the molecular scale (<10 nm), which depend on numerous factors such as pore-size, interactions of the reactants and products with the solid surfaces and with the solvent. Due to high complexity of the latter and the fact that current analytical techniques such as MAS PFG NMR or spatially and time-resolved electron paramagnetic resonance (EPR) spectroscopy, respectively [34, 35], enable only limited insights into solvent filled pores with sufficient spatial and temporal resolution, the knowledge about the molecular origins of diffusive processes in porous materials is still restricted. Molecular dynamics therefore offers complementary information for interpreting NMR measurement of diffusion [36].

Molecular dynamics simulations have been used to investigate the characteristics of diffusion of a variety of alkanes in unfunctionalized silica mesopores. Even for such relatively simple systems, a complex concentration dependent diffusion behavior may be present [37], that can be cast into the Maxwell-Stefan formulation [38]. Methodology to calculate the required thermodynamic correction factor for confined fluids has been reported recently [39]. As in simulations of bulk fluids, finite-size effects have to be considered carefully if comparison to experiment is intended [40]. Moreover, when fixing the positions of the pore wall atoms, proper thermostating of the confined fluid has to be carried out to avoid artefacts, in particular in the context of non-equilibrium simulations [41, 42]. Simulations of water dynamics in MCM-41 have been interpreted with the core-shell model in which the first water monolayer is immobile on diffusive time scales while the core water exhibits essentially bulk behavior [43]. MD simulation have also been used to interpret NMR measurements of partly and fully filled MCM-41 pores [44]. In inhomogeneous and anisotropic media mass transport is described by an anisotropic diffusion tensor that depends on the position in the pore. Diffusion parallel to the pore axis might differ from diffusion normal to the pore axis. A proper description of these effects requires the position dependent free-energy profiles of the various species [45]. Functionalized mesopores such as MCM-41 have been studied using molecular dynamics simulations with the

aim to determine the spatial distribution of two co-adsorbed molecules such as N_2 and CO_2. The strong effect of aminophenyl surface groups on the selectivity and the importance of calculating cross-term diffusion was demonstrated. Insights from these simulations allow for the design of tailor made surface groups [46–48].

A substantial number of simulation studies appeared over the last 30 years with the aim to provide a molecular-level description of physical processes underlying the reversed-phase liquid chromatography (RPLC), in particular (i) the structure and dynamics of the bonded phase and its interface with the mobile phase, (ii) the interactions of analytes with the bonded phase, and (iii) the retention mechanism for different analytes [49]. By simulations it was shown, for example, that retention into octyl (C_8) phases is best described as an adsorption process, while for octadecyl (C_{18}) phases both adsorption and partition play a role for nonpolar analytes, whereas adsorption is always the major mechanism for analyte molecules with polar groups that lead to an amphiphilic character. A recent MD study investigated the surface diffusion of four typical aromatic hydrocarbon analytes in RPLC through molecular dynamics simulations in a slit-pore RPLC model consisting of a silica-supported end-capped, C_{18} stationary phase and a 70/30 (v/v) water/acetonitrile mobile phase. The results show that the lateral (surface-parallel) diffusive mobility of the analytes goes through a maximum in the acetonitrile ditch, an acetonitrile-rich border layer around the terminal part of the bonded-phase chains [50]. The latter study illustrates the state of the art in model building and simulation methodology that can be used as starting point to study molecular processes in the context of liquid phase catalysis under confinement.

A multiscale modelling (MSM) approach enables the consideration of phenomena occurring at different scales in a single, pseudo-homogeneous model by incorporating information from sub-models that describe only one scale of the system [51, 52]. However, no universal model is capable of predicting transport and reaction in porous media due to the heterogeneity of porous structures and the complexity of the underlying microscopic mechanisms. The choice of the different scales is by no means unique but depends on the scientific questions [53]. The information from the various levels can be combined by a hierarchical MSM procedure [54, 55], that is, results from calculations at smaller scales are used as input information for calculations with parameterized or coarse-grained models on larger scales. This sequential strategy is possible if the length and time scales of the problem under study are well separated and if suitable models for linking the levels of modeling are available. For gas-phase catalysis on metal surfaces a bottom-up multiscale modeling framework based on first-principles microkinetic models has been established that condenses all short-term dynamical information into kinetic rate constants [56]. The chemical reaction has been coupled with a flow field allowing scale-up to the reactor level [57]. In zeolite catalysis such an approach works as well if small molecules are concerned such that transport limitations are not relevant [58, 59]. If transport in the micropores is the limiting factor, an explicit description in the multiscale model is required [60, 61]. For 'stop-and-go', i.e., intermittent diffusion, the atomistic data can be analyzed using the framework of intermittent Brownian dynamics [62]. Liquid phase processes that occur in silica particles of hierarchical porosity with mesopores of a few nm in diameter as the smallest scale and macropores of μm at the largest scale show a more continuous diffusion behavior such that the interplay of interfacial dynamics resolved at the single mesopore level, surface, effective meso-pore and overall bed diffusion is rather complex to describe [63]. Diffusion limitations are common in mesoporous catalysts due to the strong interactions with the pore walls [36]. The assumptions underlying viscous hydrodynamics may not be valid in such pores because the transverse momentum fluctuation shows a different relaxation behavior compared to the

bulk phase [64–66]. In the context of reversed-phase liquid chromatography (RPLC) a powerful bottom-up multiscale modeling framework has been developed by Tallarek and co-workers that describes the important mesopore scale based on physical reconstruction of the real material [67–71]. The approach is general and allows to determine effective transport properties over a hierarchy of length scales, from the molecular-detail interfacial dynamics to effective diffusion in hierarchically porous materials. Information on interfacial dynamics from atomistic MD simulations are incorporated into random-walk particle tracking (RWPT) Brownian dynamics (BD) simulations used to extract the effective diffusion coefficient. This reduces the dimensionality of the problem, making BD more computationally effective than the corresponding MD simulation. It could be shown that interfacial phenomena have a strong influence on effective diffusivities in the hierarchical material [68]. For reacting systems, the field has not yet evolved that far. In a recent study the conversion of ethanol to butadiene was considered. However, the mesoscale transport was not described explicitly but replaced by a Thiele modulus adjusted to experimental data. Moreover, the reaction was modeled in the gas phase [72]. Recently, Tallarek et al., applied the multiscale approach to the transport properties of catalyst, reactant, product and side product in the ring-closing olefin metathesis [73] paving the way to take the final step towards a holistic modeling approach i.e., by implementing chemical reactivity.

It can be concluded that methodological advances in obtaining computational models of mesoporous materials, in calculating adsorption and diffusion of various molecules in such materials as well as in applying fluid-theoretical approaches to porous materials have reached a level that allows for combining these methods with the goal to study reactive systems in confined media. However, in contrast to studies investigating reactions in ordered microporous materials such as zeolites or metal-organic frameworks, computational studies that have showcased their potential as a useful tool in the rational design of mesoporous environments are very rare. Although focusing on the single pore scale the present work represents an important step towards a consistent multi-scale description [51] with the ultimate goal to gain understanding how structurally defined pore geometry interacts with functional surface groups in order to guide the catalytic process towards higher activity, productivity and selectivity.

In Chapter 2 of this thesis a program package, referred to as PoreMS, is described which provides customizable yet simple tools for rapid model building of functionalized mesoporous silica materials. Chapter 3 illustrates the capabilities of the developed toolbox by investigating the effect of immobilized β-cyclodextrin (bCD) molecules inside a mesoporous silica support on the uptake of benzene and *p*-nitrophenol from aqueous solution using all-atom molecular dynamics (MD) simulations. In Chapter 4 the impact of different surface hydroxylation degrees as well as of the Lennard-Jones parameters of the silicon and oxygen atoms that constitute the porous material on molecular density profiles within the pore are investigated. Moreover, the Einstein and Smoluchowski approaches for calculating the self-diffusion coefficient of water and solutes in aqueous solution within the pore are compared. This comparison is extended in Chapter 5 by considering 14 different solvents. Here, particular emphasis is devoted to internal consistency of the simulation results, taking into account finite size effects. Finally, Chapter 6 contains the conclusion of this thesis and an outlook to future work.

References

[1] T. M. Bräuer, Q. Zhang, and K. Tiefenbacher. “Iminium Catalysis inside a Self-Assembled Supramolecular Capsule: Modulation of Enantiomeric Excess”. In: *Angew. Chem. Int. Ed.* 55.27 (2016), pp. 7698–7701. DOI: 10.1002/anie.201602382.

[2] C. Zhao et al. “Nucleophilic Substitution Catalyzed by a Supramolecular Cavity Proceeds with Retention of Absolute Stereochemistry”. In: *J. Am. Chem. Soc.* 136.41 (2014), pp. 14409–14412. DOI: 10.1021/ja508799p.

[3] S.-G. Shyu, S.-W. Cheng, and D.-L. Tzou. “Immobilization of Rh(PPh3)3Cl on phosphinated MCM-41 for catalytic hydrogenation of olefins”. In: *Chem. Commun.* 23 (1999), pp. 2337–2338. DOI: 10.1039/a907207a.

[4] R. Anwander. “SOMC@PMS. Surface Organometallic Chemistry at Periodic Mesoporous Silica”. In: *Chem. Mater.* 13.12 (2001), pp. 4419–4438. DOI: 10.1021/cm0111534.

[5] C. Copéret, A. Fedorov, and P. A. Zhizhko. “Surface Organometallic Chemistry: paving the Way Beyond Well-Defined Supported Organometallics and Single-Site Catalysis”. In: *Catal. Lett.* 147.9 (2017), pp. 2247–2259. DOI: 10.1007/s10562-017-2107-4.

[6] C. Copéret et al. “Bridging the Gap between Industrial and Well-Defined Supported Catalysts”. In: *Angew. Chem. Int. Ed.* 57.22 (2018), pp. 6398–6440. DOI: 10.1002/anie.201702387.

[7] M. K. Samantaray et al. “Surface organometallic chemistry in heterogeneous catalysis”. In: *Chem. Soc. Rev.* 47.22 (2018), pp. 8403–8437. DOI: 10.1039/C8CS00356D.

[8] R. J. Witzke et al. “Nontraditional Catalyst Supports in Surface Organometallic Chemistry”. In: *ACS Catal.* 10.20 (2020), pp. 11822–11840. DOI: 10.1021/acscatal.0c03350.

[9] A. Choplin and F. Quignard. “From supported homogeneous catalysts to heterogeneous molecular catalysts”. In: *Coord. Chem. Rev.* 178-180 (1998), pp. 1679–1702. DOI: 10.1016/S0010-8545(98)00062-9.

[10] R. A. van Santen and M. Neurock. *Molecular Heterogeneous Catalysis: a Conceptual and Computational Approach*. 1st ed. Wiley, 2006. ISBN: 9783527296620 9783527610846. DOI: 10.1002/9783527610846.

[11] P. W. Kletnieks et al. “Molecular Heterogeneous Catalysis: a Single-Site Zeolite-Supported Rhodium Complex for Acetylene Cyclotrimerization”. In: *Chemistry* 13.26 (2007), pp. 7294–7304. DOI: 10.1002/chem.200700721.

[12] S. Zhang et al. “Molecular heterogeneous catalysts derived from bipyridine-based organosilica nanotubes for C-H bond activation”. In: *Chem. Sci.* 8.6 (2017), pp. 4489–4496. DOI: 10.1039/C7SC00713B.

[13] E. Lindner et al. “Chemistry in Interphases - a New Approach to Organometallic Syntheses and Catalysis”. In: *Angew. Chem. Int. Ed.* 38.15 (1999), pp. 2154–2174. DOI: 10.1002/(SICI)1521-3773(19990802)38:15<2154::AID-ANIE2154>3.0.CO;2-T.

[14] E. Lindner et al. “Supported organometallic complexes. part 27: novel sol-gel processed rhodium(I) complexes: synthesis, characterization, and catalytic reactions in interphases”. In: *Inorganica Chim. Acta* 327.1 (2002), pp. 54–65. DOI: 10.1016/S0020-1693(01)00675-2.

[15] J. Rouquerol et al. “Recommendations for the characterization of porous solids (Technical Report)”. In: *Pure Appl. Chem.* 66.8 (1994), pp. 1739–1758. DOI: 10.1351/pac199466081739.

[16] F. Ziegler et al. “Confinement Effects for Efficient Macrocyclization Reactions with Supported Cationic Molybdenum Imido Alkylidene *N*-Heterocyclic Carbene Complexes”. In: *ACS Catal.* 11.18 (2021), pp. 11570–11578. DOI: 10.1021/acscatal.1c03057.

[17] S. T. Emmerling et al. “Olefin Metathesis in Confinement: towards Covalent Organic Framework Scaffolds for Increased Macrocyclization Selectivity”. In: *Chemistry* 28.8 (2022). DOI: 10.1002/chem.202104108.

[18] Z. ALOthman. “A Review: fundamental Aspects of Silicate Mesoporous Materials”. In: *Materials* 5.12 (2012), pp. 2874–2902. DOI: 10.3390/ma5122874.

[19] F. Di Renzo et al. “Micelle-Templated Materials”. In: *Handbook of Porous Solids*. Ed. by F. Schth, K. S. W. Sing, and J. Weitkamp. Weinheim, Germany: Wiley-VCH Verlag GmbH, 2002, pp. 1311–1395. ISBN: 9783527618286 9783527302468. DOI: 10.1002/9783527618286.ch21a.

[20] K. Cassiers et al. “A Detailed Study of Thermal, Hydrothermal, and Mechanical Stabilities of a Wide Range of Surfactant Assembled Mesoporous Silicas”. In: *Chem. Mater.* 14.5 (2002), pp. 2317–2324. DOI: 10.1021/cm0112892.

[21] D. Zhao et al. “Triblock Copolymer Syntheses of Mesoporous Silica with Periodic 50 to 300 Angstrom Pores”. In: *Science* 279.5350 (1998), pp. 548–552. DOI: 10.1126/science.279.5350.548.

[22] D. Zhao et al. “Nonionic Triblock and Star Diblock Copolymer and Oligomeric Surfactant Syntheses of Highly Ordered, Hydrothermally Stable, Mesoporous Silica Structures”. In: *J. Am. Chem. Soc.* 120.24 (1998), pp. 6024–6036. DOI: 10.1021/ja974025i.

[23] D. Zhao et al. “Correction to “nonionic Triblock and Star Diblock Copolymer and Oligomeric Surfactant Syntheses of Highly Ordered, Hydrothermally Stable, Mesoporous Silica Structures””. In: *J. Am. Chem. Soc.* 136.29 (2014), pp. 10546–10546. DOI: 10.1021/ja506344k.

[24] B. Karimi et al. “Periodic mesoporous organosilicas (PMOs): from synthesis strategies to applications”. In: *Prog. Mater. Sci.* 125 (2022), p. 100896. DOI: 10.1016/j.pmatsci.2021.100896.

[25] V. Meynen, P. Cool, and E. Vansant. “Verified syntheses of mesoporous materials”. In: *Microporous Mesoporous Mater.* 125.3 (2009), pp. 170–223. DOI: 10.1016/j.micromeso.2009.03.046.

[26] M. E. Raimondi et al. “One-pot incorporation of titanium catalytic sites into mesoporous true liquid crystal templated (TLCT) silica”. In: *Chem. Commun.* 1 (1999), pp. 87–88. DOI: 10.1039/a806700g.

[27] J. R. Bruckner et al. “Mechanisms and Intermediates in the True Liquid Crystal Templating Synthesis of Mesoporous Silica Materials”. In: *J. Phys. Chem. B* 125.12 (2021), pp. 3197–3207. DOI: 10.1021/acs.jpcb.0c11005.

[28] F. Markus et al. “Ordered Mesoporous Carbons via Self-Assembly of Tailored Block Copolyethers for Pore Size-Dependent Applications”. In: *ACS Appl. Nano Mater.* 4.4 (2021), pp. 3486–3492. DOI: 10.1021/acsanm.0c03467.

[29] A.-K. Beurer et al. “Efficient and Spatially Controlled Functionalization of SBA-15 and Initial Results in Asymmetric Rh-Catalyzed 1,2-Additions under Confinement”. In: *Chem. Cat. Chem.* 13.10 (2021), pp. 2407–2419. DOI: 10.1002/cctc.202100229.

[30] Y. Ishii et al. “Pore Size Determination in Ordered Mesoporous Materials Using Powder X-ray Diffraction”. In: *J. Phys. Chem. C* 117.35 (2013), pp. 18120–18130. DOI: 10.1021/jp4057362.

[31] C. Schumacher et al. “Generation of Atomistic Models of Periodic Mesoporous Silica by Kinetic Monte Carlo Simulation of the Synthesis of the Material”. In: *J. Phys. Chem. B* 110.1 (2006), pp. 319–333. DOI: 10.1021/jp0551871.

[32] Z. Brkljača et al. “Complementary Molecular Dynamics and X-ray Reflectivity Study of an Imidazolium-Based Ionic Liquid at a Neutral Sapphire Interface”. In: *J. Phys. Chem. Lett.* 6.3 (2015), pp. 549–555. DOI: 10.1021/jz5024493.

[33] J. B. Mietner et al. “Properties of Water Confined in Periodic Mesoporous Organosilicas: nanoimprinting the Local Structure”. In: *Angew. Chem. Int. Ed.* 56.40 (2017), pp. 12348–12351. DOI: 10.1002/anie.201705707.

[34] J. Kärger and R. Valiullin. “Mass transfer in mesoporous materials: the benefit of microscopic diffusion measurement”. In: *Chem. Soc. Rev.* 42.9 (2013), p. 4172. DOI: 10.1039/c3cs35326e.

[35] M. Wessig et al. “Multiple scale investigation of molecular diffusion inside functionalized porous hosts using a combination of magnetic resonance methods”. In: *Phys. Chem. Chem. Phys.* 17.24 (2015), pp. 15976–15988. DOI: 10.1039/C5CP01369K.

[36] B. C. Bukowski et al. “Connecting theory and simulation with experiment for the study of diffusion in nanoporous solids”. In: *Adsorption* 27.5 (2021), pp. 683–760. DOI: 10.1007/s10450-021-00314-y.

[37] R. Krishna and J. M. van Baten. “A molecular dynamics investigation of the unusual concentration dependencies of Fick diffusivities in silica mesopores”. In: *Microporous Mesoporous Mater.* 138.1-3 (2011), pp. 228–234. DOI: 10.1016/j.micromeso.2010.09.032.

[38] R. Krishna and J. van Baten. “Unified Maxwell-Stefan description of binary mixture diffusion in micro- and meso-porous materials”. In: *Chem. Eng. Sci.* 64.13 (2009), pp. 3159–3178. DOI: 10.1016/j.ces.2009.03.047.

[39] J. Collell and G. Galliero. “Determination of the thermodynamic correction factor of fluids confined in nano-metric slit pores from molecular simulation”. In: *J. Chem. Phys.* 140.19 (2014), p. 194702. DOI: 10.1063/1.4875703.

[40] P. Simonnin et al. “Diffusion under Confinement: hydrodynamic Finite-Size Effects in Simulation”. In: *J. Chem. Theory Comput.* 13.6 (2017), pp. 2881–2889. DOI: 10.1021/acs.jctc.7b00342.

[41] S. Bernardi, B. D. Todd, and D. J. Searles. “Thermostating highly confined fluids”. In: *J. Chem. Phys.* 132.24 (2010), p. 244706. DOI: 10.1063/1.3450302.

[42] S. De Luca et al. “A new and effective method for thermostatting confined fluids”. In: *J. Chem. Phys.* 140.5 (2014), p. 054502. DOI: 10.1063/1.4862544.

[43] I. C. Bourg and C. I. Steefel. “Molecular Dynamics Simulations of Water Structure and Diffusion in Silica Nanopores”. In: *J. Phys. Chem. C* 116.21 (2012), pp. 11556–11564. DOI: 10.1021/jp301299a.

[44] A. Pajzderska et al. “Water Behavior in MCM-41 as a Function of Pore Filling and Temperature Studied by NMR and Molecular Dynamics Simulations”. In: *J. Phys. Chem. C* 118.41 (2014), pp. 23701–23710. DOI: 10.1021/jp505490c.

[45] A. Ghysels et al. “Position-Dependent Diffusion Tensors in Anisotropic Media from Simulation: oxygen Transport in and through Membranes”. In: *J. Chem. Theory Comput.* 13.6 (2017), pp. 2962–2976. DOI: 10.1021/acs.jctc.7b00039.

[46] J. J. Williams et al. “Effect of Surface Group Functionalization on the CO_2/N_2 Separation Properties of MCM-41: a Grand-Canonical Monte Carlo Simulation Study”. In: *J. Phys. Chem. C* 114.43 (2010), pp. 18538–18547. DOI: 10.1021/jp105464u.

[47] J. J. Williams, N. A. Seaton, and T. Düren. “Influence of Surface Groups on the Diffusion of Gases in MCM-41: a Molecular Dynamics Study”. In: *J. Phys. Chem. C* 115.21 (2011), pp. 10651–10660. DOI: 10.1021/jp112073z.

[48] Y. Zhu et al. “The effect of grafted amine group on the adsorption of CO_2 in MCM-41: a molecular simulation”. In: *Catal. Today* 194.1 (2012), pp. 53–59. DOI: 10.1016/j.cattod.2012.02.022.

[49] R. K. Lindsey et al. “Molecular simulation studies of reversed-phase liquid chromatography”. In: *J. Chromatogr. A* 1287 (2013), pp. 60–82. DOI: 10.1016/j.chroma.2013.02.040.

[50] J. Rybka, A. Höltzel, and U. Tallarek. “Surface Diffusion of Aromatic Hydrocarbon Analytes in Reversed-Phase Liquid Chromatography”. In: *J. Phys. Chem. C* 121.33 (2017), pp. 17907–17920. DOI: 10.1021/acs.jpcc.7b04746.

[51] U. Tallarek, D. Hlushkou, and A. Höltzel. “Solute Sorption, Diffusion, and Advection in Macro-Mesoporous Materials: toward a Realistic Bottom-Up Simulation Strategy”. In: *J. Phys. Chem. C* 126.5 (2022), pp. 2336–2348. DOI: 10.1021/acs.jpcc.1c10137.

[52] G. D. Wehinger et al. “Quo vadis multiscale modeling in reaction engineering? - a perspective”. In: *Chem. Eng. Res. Des.* 184 (2022), pp. 39–58. DOI: 10.1016/j.cherd.2022.05.030.

[53] D. G. Vlachos. “Multiscale modeling for emergent behavior, complexity, and combinatorial explosion”. In: *AIChE J.* 58.5 (2012), pp. 1314–1325. DOI: 10.1002/aic.13803.

[54] A. Uhlherr and D. N. Theodorou. “Hierarchical simulation approach to structure and dynamics of polymers”. In: *Curr. Opin. Solid State Mater. Sci.* 3.6 (1998), pp. 544–551. DOI: 10.1016/S1359-0286(98)80023-5.

[55] D. N. Theodorou. “Hierarchical modeling of amorphous polymers”. In: *Comput. Phys. Commun.* 169.1-3 (2005), pp. 82–88. DOI: 10.1016/j.cpc.2005.03.020.

[56] A. Bruix et al. “First-principles-based multiscale modelling of heterogeneous catalysis”. In: *Nat. Catal.* 2.8 (2019), pp. 659–670. DOI: 10.1038/s41929-019-0298-3.

[57] M. Hettel, M. Wörner, and O. Deutschmann. “Computational Fluid Dynamics of Catalytic Reactors”. In: *Handbook of Materials Modeling*. Ed. by W. Andreoni and S. Yip. Cham: Springer International Publishing, 2018, pp. 1–34. ISBN: 9783319502571. DOI: 10.1007/978-3-319-50257-1_6-1.

[58] A. Heyden, A. Bell, and F. Keil. “Kinetic modeling of nitrous oxide decomposition on Fe-ZSM-5 based on parameters obtained from first-principles calculations”. In: *J. Catal.* 233.1 (2005), pp. 26–35. DOI: 10.1016/j.jcat.2005.04.003.

[59] S. Aranifard et al. “Kinetic modeling of nitrous oxide decomposition on Fe-ZSM-5 in the presence of nitric oxide based on parameters obtained from first-principles calculations”. In: *Catal. Sci. Technol.* 11.10 (2021), pp. 3539–3555. DOI: 10.1039/D1CY00252J.

[60] N. Hansen et al. “Analysis of Diffusion Limitation in the Alkylation of Benzene over H-ZSM-5 by Combining Quantum Chemical Calculations, Molecular Simulations, and a Continuum Approach”. In: *J. Phys. Chem. C* 113.1 (2009), pp. 235–246. DOI: 10.1021/jp8073046.

[61] N. Hansen and F. J. Keil. “Multiscale Modeling of Reaction and Diffusion in Zeolites: from the Molecular Level to the Reactor”. In: *Soft Mater.* 10.1-3 (2012), pp. 179–201. DOI: 10.1080/1539445X.2011.599708.

[62] C. Bousige, P. Levitz, and B. Coasne. “Bridging scales in disordered porous media by mapping molecular dynamics onto intermittent Brownian motion”. In: *Nat. Commun.* 12.1 (2021), p. 1043. DOI: 10.1038/s41467-021-21252-x.

[63] A. Phan, D. Fan, and A. Striolo. “Fluid transport through heterogeneous pore matrices: multiscale simulation approaches”. In: *Phys. Fluids* 32.10 (2020), p. 101301. DOI: 10.1063/5.0022481.

[64] L. Bocquet and E. Charlaix. “Nanofluidics, from bulk to interfaces”. In: *Chem. Soc. Rev.* 39.3 (2010), pp. 1073–1095. DOI: 10.1039/B909366B.

[65] K. Falk et al. “Subcontinuum mass transport of condensed hydrocarbons in nanoporous media”. In: *Nat. Commun.* 6.1 (2015), p. 6949. DOI: 10.1038/ncomms7949.

[66] B. Coasne. “Multiscale adsorption and transport in hierarchical porous materials”. In: *New J. Chem.* 40.5 (2016), pp. 4078–4094. DOI: 10.1039/C5NJ03194J.

[67] S.-J. Reich et al. “Transport under confinement: hindrance factors for diffusion in core-shell and fully porous particles with different mesopore space morphologies”. In: *Microporous Mesoporous Mater.* 282 (2019), pp. 188–196. DOI: 10.1016/j.micromeso.2019.02.036.

[68] U. Tallarek et al. “Multiscale Simulation of Diffusion in Porous Media: From Interfacial Dynamics to Hierarchical Porosity”. In: *J. Phys. Chem. C* 123.24 (2019), pp. 15099–15112. DOI: 10.1021/acs.jpcc.9b03250.

[69] J. Hochstrasser et al. “Morphology-transport relationships for SBA-15 and KIT-6 ordered mesoporous silicas”. In: *Phys. Chem. Chem. Phys.* 22.20 (2020), pp. 11314–11326. DOI: 10.1039/D0CP01861A.

[70] B. Prifling et al. “Generating digital twins of mesoporous silica by graph-based stochastic microstructure modeling”. In: *Comput. Mater. Sci.* 187 (2021), p. 109934. DOI: 10.1016/j.commatsci.2020.109934.

[71] D. Enke, R. Gläser, and U. Tallarek. “Sol-Gel and Porous Glass-Based Silica Monoliths with Hierarchical Pore Structure for Solid-Liquid Catalysis”. In: *Chem. Ing. Tech.* 88.11 (2016), pp. 1561–1585. DOI: 10.1002/cite.201600049.

[72] V. S. Bharadwaj et al. “Multi-scale simulation of reaction, transport and deactivation in a SBA-16 supported catalyst for the conversion of ethanol to butadiene”. In: *Catal. Today* 338 (2019), pp. 141–151. DOI: 10.1016/j.cattod.2019.05.042.

[73] U. Tallarek et al. “Olefin Ring-closing Metathesis under Spatial Confinement: morphology-Transport Relationships”. In: *Chem. Cat. Chem.* 13.1 (2021), pp. 281–292. DOI: 10.1002/cctc.202001495.

2. PoreMS: A software tool for generating silica pore models with user-defined surface functionalization and pore dimensions

The content of this chapter is a literal quote of the publication

H. Kraus, J. Rybka, A. Höltzel, N. Trebel, U. Tallarek and N. Hansen, Molecular Simulation, 47(4), 306-316, 2021

J. Rybka was involved in developing the pore generation procedure. A. Höltzel was involved in the RPLC topic and in editing the manuscript. N. Trebel helped constructing the RPLC-pore discussed in the manuscript. U. Tallarek had an advisory role and was involved in editing the manuscript. N. Hansen had the role of a daily supervisor and was involved in editing the manuscript. Additions or deletions compared to the published work are marked with square brackets.

Mass transport under confinement is at the heart of all processes employing functionalized mesoporous silica materials, such as liquid chromatography, heterogeneous catalysis, and gas adsorption. Molecular simulation studies of mass transport in such settings require pore models that replicate the geometry, dimensions, and chemical structure of a surface-functionalized silica mesopore. We present a software tool that facilitates rapid model building of functionalized silica pores for systematic studies of confinement effects in various applications of relevant materials. The tool allows to choose the chemical structure and density of the ligands and to control the residual hydroxylation of the silica surface. Individual ligands can be placed at a user-defined position on the surface. Moreover, the tool supports an independent functionalization of the interior and exterior pore surface. We explain each step of the pore generation, discuss the underlying assumptions and limitations, and introduce examples of generated cylindrical pore models for chromatography and catalysis.

2.1. Introduction

Mesoporous silica materials are ubiquitous in technical applications ranging from (gas) adsorption over chromatography and catalysis to drug delivery [1–8]. Key to a successful design of technical processes employing such materials is an understanding of mass transport in the confined environment, ideally based on molecular-level information about the composition, structure, and dynamics of the components present inside the silica mesopore [9]. These typically include gas or solvent molecules, solute molecules, and the ligands and surface atoms of the functionalized or bare silica surface. Molecular simulations, particularly atomistic molecular dynamics (MD) simulations, have already been used to elucidate the mass transport characteristics of different liquid chromatography modes [10–16] and recently to model catalytic [17–19] and drug delivery systems [20]. This suggests that molecular simulations are increasing in importance as an essential building block in multiscale modelling of heterogeneous catalysis [21] and the selection and development of chromatographic columns [22–25]. The molecular insight gained by such studies was used, for example, to obtain a unified description of diffusion inside mesoporous and microporous structures [26], to rationalize the effect of surface chemistry on olefin metathesis in confined geometries [17], and to provide fundamental insight into reactive ionic liquid films for supported ionic liquid phase (SILP) catalysis relevant for electrochemical systems or the water-gas shift reaction [27–29]. Moreover, such simulations may be used to generate parameters for coarse-grained models that span significantly larger length and time scales than models with atomistic resolution [30–32]. It is therefore desirable to further widen the scope of such simulations by increasing the complexity of the studied systems.

Confinement effects on fluid structure and mass transport in silica mesopores are related to the size, geometry, surface properties and functionalization of the pore. In molecular simulation studies, these effects can be investigated independent of each other by using pore models that incorporate only one or two aspects of the relevant properties, as exemplified by the standard slit pore model [10, 33, 34]. In reality, the effects of size, geometry, and surface functionalization are intrinsically coupled. The mesopore shape of sol-gel processed silica adsorbents, used in liquid chromatography, is typically assumed as cylindrical, which also applies to certain templated ordered mesoporous silicas, such as MCM-41 [35], SBA-15 [36] and KIT-6 [37], used in heterogeneous catalysis. The cylindrical pore shape of SBA-15 and KIT-6 was confirmed by recent physical reconstructions of these materials [38, 39]. At equal pore width or diameter, the area available to ligands, solvent, and solute molecules is constant over the pore width for a planar (slit) geometry, but decreases towards the pore centre for a cylindrical geometry. Consequently, a curved silica surface influences the properties of the fluid filling the pore over a wider distance (measured from the surface) than a planar slit pore [40, 41]. The critical diameter, at which bulk fluid properties cannot be recovered within the pore, is larger for a cylindrical than a comparable slit pore [9]. For most pore sizes of interest ($\leq 10\,\mathrm{nm}$) the divergence between cylindrical and planar pore geometry is expected to increase with the degree of surface functionalization and the spatial requirements of the ligands. Nevertheless, molecular simulation studies in cylindrical silica pores with an explicit surface functionalization that goes beyond a simple hydrophobic capping of the surface OH groups are still rare [17, 40, 42–45]. The model generation for cylindrical silica pores without surface functionalization targets a realistic representation of the silica surface, including roughness and amorphicity, as the focus is on the direct interaction of gas, solvent, and solute molecules with the atoms of the silica surface. Two different strategies for the generation of computational models of porous silica materials can be envisioned. The first starts from a sample of bulk material and drills a pore by removing

atoms. Subsequently dangling bonds need to be removed or appropriately saturated. The starting bulk material may be either crystalline [46] or amorphous and can for example be generated by molecular dynamics [47, 48] or reverse Monte Carlo sampling [49]. The second strategy attempts to resemble the synthesis process by lattice Monte Carlo [50–52], kinetic Monte Carlo [53, 54] or molecular dynamics simulations [55]. The different approaches have been discussed recently by Han et al. [56].
The purpose of functionalized mesoporous silica materials is to direct the interaction towards the ligands. Therefore, the pore model generation in this case must emphasize a realistic representation of the surface functionalization (the chemistry, density, and spatial distribution of the ligands) while preserving the essential properties of the silica surface, mainly the degree of residual surface hydroxylation (i.e., the amount of unreacted OH groups on the silica surface). Additionally, the pore model generation must allow an independent functionalization of the interior and exterior pore surface to replicate experimental conditions in certain applications. Moreover, the pore model generation should enable the study of increasingly complex systems through supporting the inclusion of non-standard ligands (such as organometallic catalysts), and finally, foster reproducibility, transferability and extensibility of molecular simulation studies throughout the scientific community [57].

This work shows a straightforward way to functionalized silica pore models that meet the criteria outlined above. We introduce PoreMS, an open-source Python tool that offers a seamless workflow from the generation of coordinates to the input files required for molecular dynamics simulation codes such as GROMACS [58]. The remainder of the article is organized as follows. Section 2 describes the main functionality of the pore generation tool. Section 3 provides and discusses examples of generated cylindrical pore models for chromatography and catalysis settings. Further developments are discussed in the conclusion and outlook. A step-by-step guide for generating the discussed pore systems is provided in the Supplementary Material accompanying the present work.

2.2. Methodology

In the following the design of the code is outlined along with some technical aspects of the parallelization. For a detailed overview we refer to the online documentation [59]. There, a complete workflow for the generation of a functionalized pore model is provided, including the generation of functional groups from scratch. The two pore models presented in Section 3 of the present work can be replicated with the Jupyter notebooks provided in the Supplementary Material. For an extension of the code basic Python knowledge is advantageous.

2.2.1. Pore generation

The PoreMS package consists of several independent modules designed for a specific task, such as building ligand structures from scratch or carving a pore of specified geometry. A functionalized pore system is generated by executing all modules sequentially, in the appropriate order for the specific problem. In this way, the user has insight into all steps, ensuring simple, individual customization as well as the possibility to utilize ready-to-use pore generation classes for specific pore geometries.

At the core of the package resides the `Molecule` module containing functions to place, translate, and rotate atoms in the three-dimensional space. Based on this module a pattern class has been devised to construct a crystal lattice consisting of O and Si atoms. As of version 0.2.0, only

the structure of β-cristobalite SiO_2 has been implemented. Simulations in slit-pore models have proved that the faces of β-cristobalite SiO_2, particularly its (111) face, support the envisioned ligand density and residual hydroxylation of functionalized and bare silica materials used in chromatographic columns [10, 12–14, 24, 25, 34, 40, 41]. Moreover, MD simulations have shown that non-functionalized, cylindrical pores carved from β-cristobalite SiO_2 replicate the relevant properties of the bare silica surface in liquid chromatography well [9, 11]. As shown in Section 2.2, carving a cylindrical pore into the crystalline SiO_2 block introduces elements of the amorphous silica surface, such as the presence of different types of silanol groups and a certain surface roughness, to the interior pore surface. In the β-cristobalite structure each Si atom together with its four surrounding O atoms forms a tetrahedron with

$$\alpha_{\mathrm{O-Si-O}} = \frac{2 \cdot 180}{\pi} \tan^{-1} \sqrt{2} = 109.47°, \quad l_{\mathrm{Si-O}} = 0.1550\,\mathrm{nm}. \tag{2.2.1}$$

Si atoms are placed in a diamond structure with O atoms located midway between each pair of nearest-neighbour Si atoms ($\alpha_{\mathrm{Si-O-Si}} = 180°$). This structure forms the space group $Fd\bar{3}m$ and has two formula units per primitive unit cell [60–63]. In the present work, the rectangular β-cristobalite block is generated with edge lengths that are individually adjustable within step widths of 0.506, 0.877 and 1.240 nm in x-, y-, and z-direction, respectively, corresponding to the size of the translationally invariant building block used (see Figure 2.2.1), which consists of 12 Si and 24 O atoms. Note that this minimal building block does not correspond to the cubic unit cell of β-cristobalite containing 8 SiO_2 groups, because for reasons outlined in Section 3 the (111) face was selected as exterior pore surface in the present work.

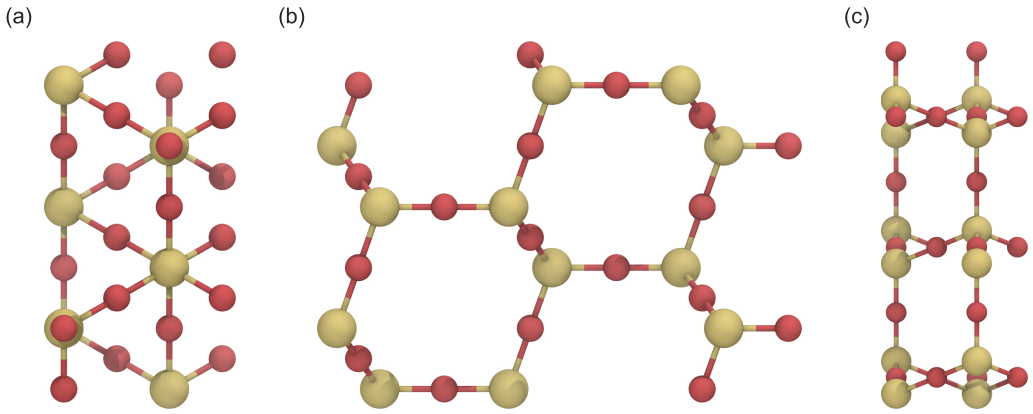

Figure 2.2.1.: Building block of β-cristobalite viewed (a) from the xy-plane, (b) from the zy-plane and (c) from the xz-plane. Si and O atoms are coloured yellow and red, respectively.

Using the main pattern class as a container, child classes can be created to build other crystal lattices. Utilizing the shape class, individual geometrical shapes such as cylinder or sphere can be defined to be carved out from the generated β-cristobalite block. For defining new shape classes, it is required to determine and implement the mathematical function defining the intended geometrical shape. This function will be used to determine the vector perpendicular to any point on the surface by calculating the cross product of the partial derivative of the surface function. For example, the surface function Φ of a cylinder of fixed radius r is given by

$$\Phi\left(\phi, z; r\right) = \begin{bmatrix} r\cos\phi \\ r\sin\phi \\ z \end{bmatrix}. \tag{2.2.2}$$

Thus, the normal vector is obtained from

$$\left[\frac{\partial\Phi}{\partial\phi}\times\frac{\partial\Phi}{\partial z}\right](\phi,z;r)=\begin{bmatrix}r\cos\phi\\ r\sin\phi\\ 0\end{bmatrix}. \tag{2.2.3}$$

These normal vectors will be used for surface functionalization. The position of the centre of geometry as well as the orientation of the geometrical object with respect to the x-, y-, and z-directions can be freely defined, which enables different drill directions. As of this version, only basic geometrical shapes, such as cylinder, sphere, and cuboid are implemented. These predefined shapes can be combined to create an individual shape. Once defined, the shape is carved out of the lattice by removing all atoms within its bounds.

The atom removal generates unsaturated Si and O atoms, resulting in chemically flawed pore surfaces. Reconstruction of the surface chemistry follows the rules of Coasne et al. [46]. First unsaturated Si atoms are removed. Additionally, Si atoms bonded to three dangling O atoms are removed (together with the three O atoms) as they rarely exist on silica surfaces [33, 64, 65]. Depending on the drill direction the surface reconstruction leads to different values of the surface roughness and circularity of the resulting pore. The resulting surface has fully saturated Si atoms with a maximum of two unsaturated O bonds, which will be used as binding sites to attach ligands to the surface. The computational effort related to this process is determined by multiple atom–atom searches for n atoms with an algorithmic expense of $\mathcal{O}\left(n^2\right)$.

The implemented algorithm splits the whole system into smaller, monosized cubes containing intersecting atoms. A scan for the bonds of an atom is then performed solely in the cube containing the atom and its immediate neighbour cubes, that is, in 27 cubes. Due to fixed bond lengths in the lattice, the number of atoms b in a cube is constant. The number of atom–atom searches for each cube is thus a constant with $27\cdot b^2$ iterations. Therefore, the computational effort for an entire search scales linearly with the number of cubes C, $\mathcal{O}(C)$. Doubling the β-cristobalite block size in each direction, for example, only increases the effort eightfold compared to an unoptimized approach that would increase the effort 64 times. Furthermore, the search is easily parallelized, because no communication is needed between the subprocesses that each cover a set of cubes.

Although the search can be parallelized, multiple iterations are still required for the surface preparation. Also, it is impossible to ensure that all bonds are found when iteratively deleting atoms, because all systems are shaped differently. To overcome these issues the number of iterations was reduced to a single search of the expense of $\mathcal{O}(C)$ by creating a connectivity matrix of all lattice atoms prior to pore carving. The result is a dictionary that has atoms $1\dots n$ as keys and their corresponding value is a list of bonded atoms $1\dots m$

$$\boldsymbol{C}=\begin{Bmatrix}a_1: & \begin{bmatrix}a_{1,1} & a_{1,2} & \dots & a_{1,m_1}\end{bmatrix}\\ a_2: & \begin{bmatrix}a_{2,1} & a_{2,2} & \dots & a_{2,m_2}\end{bmatrix}\\ \vdots & & \vdots & \\ a_n: & \begin{bmatrix}a_{n,1} & a_{n,2} & \dots & a_{n,m_n}\end{bmatrix}\end{Bmatrix}. \tag{2.2.4}$$

In this implementation, pore carving is no longer associated with physically deleting atoms but with removing binding partners from the matrix. Surface preparation only considers the number of bonds remaining in each entry to determine whether an atom needs to be removed or not, which results in a computational effort scaling linearly with the number of atoms, $\mathcal{O}(n)$.

Combining all described modules, pore system classes were implemented to allow an easy generation of pore models for molecular simulations. In the package version 0.2.0, ready-to-use functions to generate cylindrical pores as well as slit pores are available.

2.2.2. Surface functionalization

PoreMS generates a list of all Si atoms bonded to unsaturated O atoms with their corresponding binding partners. The reason to enumerate the Si atoms instead of the O atoms is the simplicity in determining whether the location represents a single or a geminal binding site (one or two unsaturated O atoms, respectively, connected to the Si atom) using the connectivity matrix introduced above. The connectivity matrix assumes periodic boundary conditions in each direction. If a solvent reservoir should be attached to the pore, the corresponding periodic boundary conditions are suspended. The binding sites emerging from this process prior to pore carving are designated as exterior binding sites. Binding sites generated as the result of pore carving are designated as interior binding sites.

Ligands for surface functionalization may be constructed using the molecule builder functionality of the PoreMS package. Alternatively, an existing structure file can be used, for example in .gro or .pdb format. The recognition of other formats can be easily implemented by the user.

The ligand attachment is divided into multiple steps. To avoid overlap the radius of a cylinder around the main axis of the ligand (user-defined by specifying two atoms) is determined based on the Van-der-Waals radii of the atom types. Available Si binding sites within this ligand exclusion radius are found and hydroxylated to prevent future functionalizations, unless the ligand-radius is scaled to zero, thus maximising surface coverage but risking ligand–ligand overlap. The program does not check whether the chosen surface coverage is realistic; that responsibility lies with the user.

The second step is randomly choosing a Si atom from the earlier mentioned list of binding sites utilizing a uniformly distributed random number generator. If the chosen binding site is already occupied, the random selection is repeated. To prevent an infinite loop, a maximal number of retries is specified, which may also be adjusted. Alternatively, instead of a random selection, a Cartesian position can be passed on to the method. In this case, the nearest unoccupied binding site will be chosen.

In case the binding site is unoccupied, the ligand is rotated so that its main axis and the normal vector of the surface (determined by the derivative of the surface function at the geometrical position of the Si atom) are aligned. The exterior surface is handled similar to the interior surface. At the planar exterior surface, the normal vector is simply the vector perpendicular to and pointing away from the surface. In case the chosen Si atom represents a geminal binding site no further functional group can be added. This is how the program ensures that double occupancy of the same Si atom by ligands is impossible even with the overlap function turned off. The Si and O atoms of the binding site are replaced by the respective atoms from the ligand. In this way the intramolecular force field terms governing the connection of the ligand to the frozen lattice atoms can be individually customized for each ligand type. Consequently, ligand topologies have to be provided for a single and a geminal binding site. The remaining dangling O atom of an occupied geminal binding site is saturated with an H atom. In case the mentioned overlap functionality is enabled, binding sites within the proximity of the now occupied one are recursively saturated with H atoms. Because the OH group is not treated as frozen in the simulations, the same procedure as for ligands is carried out, that is, lattice Si-O or O-Si-O units

are replaced with single (Si-O-H) or geminal (H-O-Si-O-H) silanol groups, respectively, and assigned a specific residue name, such that they can be distinguished from the fixed lattice atoms in the generated coordinate file. At the end of the user-specified surface functionalization process, the remaining single and geminal unoccupied binding sites are replaced with single and geminal silanol groups, respectively, to neutralize the total pore charge and ensure chemical integrity of the surface.

Optionally, the surface hydroxylation can be reduced prior to surface functionalization through siloxane bridge formation. Following a similar approach as Krishna et al. [26], the program identifies Si-O-Si-O-Si arrangements from which the middle Si atom was cut out during pore carving. This arrangement exists in three variations: 1) one dangling O atom at each of the outer Si atoms; 2) two dangling O atoms at each of the outer Si atoms; 3) one and two dangling O atoms at the outer Si atoms. One dangling O atom is removed from each outer Si atom and a central O atom is then placed at the geometric mean location of the two removed O atoms. The resulting siloxane bridge has a Si-O bond length of 2.69 Å and Si-O-Si angle of 140.9°, close to the median of the siloxane bond angle distribution in bulk vitreous silica [66]. The bond length is larger than a typical Si-O bond due to the prescribed lattice positions of Si atoms in the β-cristobalite structure, whose distance is 5.07 Å. The exact representation of siloxane groups is, however, of minor importance for pore models where the silica surface is covered with relatively bulky functional groups. Reduction of surface hydroxylation is controlled by the user, whereby the maximum number of siloxane bridges and thus the minimal surface hydroxylation are limited by the β-cristobalite structure and the drilling direction. The placement of siloxane bridges is handled by randomly selecting two Si atoms in accordance with the distance criterion described above. If the binding sites are geminal, they are converted to single binding sites, if the binding sites are single, they are removed from the binding site list constructed at the beginning. Because the program package is built for maximal individualization, siloxane bridges can be introduced at any step of pore model generation. It is, however, advisable to execute this step prior to ligand attachment, because finding two unoccupied binding sites fulfilling the distance criterion is less probable once ligands are attached to the surface.

If a reservoir is used, the size of the simulation box is adapted accordingly. The size of the reservoir is measured from the outermost atoms of the functional groups attached to the exterior surface. The Cartesian coordinates of the final pore are provided in .gro and .pdb format, respectively. An extension to other formats by the user is easily possible.

2.2.3. Force field parameters

To use the generated pores in actual molecular simulations, force-field parameters have to be provided by the user. If, for example, GROMACS is used as MD engine, itp files have to be defined for every species. The molecules may be parametrised externally (for uncommon ligands such as organometallic catalysts) or with the molecule builder that is part of PoreMS. The latter generates job files for the Antechamber topology builder [67]. Only for Si, O and H atoms belonging to the silica lattice or the surface silanol groups, respectively, the force-field parameters are provided by PoreMS and are taken from the work of Gulmen and Thompson [68]. Alternative force-field parameters [69] may then be assigned on the topology level. The compatibility of force-field parameters for different functional groups has to be ensured by the user.

2.3. Results and Discussion

2.3.1. Pore model for reversed-phase liquid chromatography

A pore model for high-performance liquid chromatography aims to replicate the conditions inside a chromatographic column. The column is a fixed bed containing two types of pores, macropores for advective (flow-driven) transport and mesopores for diffusive transport. This type of architecture is realized by dense packings of µm-sized, mesoporous, spherical silica particles or by macroporous silica monoliths with mesoporous skeletons. Silica particles are functionalized before being packed into a column, whereas silica monoliths are fully formed prior to surface functionalization. In reversed-phase liquid chromatography (RPLC), the most widely used separation mode today, compounds of low-to-moderate polarity are separated between a hydrophobic stationary phase and an aqueous–organic mobile phase. The stationary phase is the silica structure bearing the bonded phase, which consists of the main ligand and eventually endcapping groups. RPLC ligands are typically unbranched alkyl chains of defined length. The ligands are covalently attached to reactive groups at the silica surface, which are present inside the mesopores as well as at the outside of a silica particle or skeleton. Consequently, ligands line the macropores as well as the mesopores. Surface functionalization with the main ligand is usually followed by endcapping, a process in which short, voluminous, hydrophobic groups are attached to previously unreacted surface OH groups to reduce as well as shield the residual hydroxylation of the silica surface. Compounds are separated according to their differential interaction with the chromatographic interface, which forms when the column is equilibrated with the liquid mobile phase prior to sample injection. At the instrumental level, column equilibration refers to pumping the mobile phase through the column until the composition of the effluent liquid matches the composition of the influent liquid. At the molecular level, column equilibration refers to the interaction between the stationary phase and the solvent molecules of the mobile phase. Solvent molecules penetrate the bonded phase, solvating the ligands, and coordinate the residual OH groups of the silica surface. The most important process occurring during column equilibration in RPLC is the formation of an organic-solvent rich layer at the interface between the alkyl chain ends and the bulk mobile phase. This layer forms a transition between the hydrophobic ligands and the aqueous–organic fluid that strives to preserve

Table 2.3.1.: Input parameters used to generate the RPLC mesopore model.

	Interior	Exterior
Target silica block xyz-dimensions (nm)	16.0; 16.0; 10.0	
Pore drilling direction	z	
Target pore diameter (nm)	9.0	
Solvent reservoir z-dimension (nm)		5.5
Target surface hydroxylation[a] (µmol m^{-2})	7.82	7.82
Siloxane bridges	Yes	No
Main ligand	C_{18}	C_{18}
Target ligand density (µmol m^{-2})	2.91	2.91
Endcapping with TMS groups	Yes	Yes
Target TMS density[b] (µmol m^{-2})	0.70	0.71

[a]Instant hydroxylation of interior and exterior surfaces after pore carving is indicated to the user in the program. [b]Chosen such that a target bonded-phase coverage of 46 % after siloxane bridge formation was achieved.

its hydrogen-bonding structure.

In the pore model, the two surfaces of the silica block perpendicular to the pore axis and facing the solvent reservoirs represent the exterior of a mesoporous particle or skeleton. At the nm-scale of the cylindrical pore, the exterior of the µm-sized particle or skeleton is approximately flat. Relevant chemical parameters to replicate an RPLC mesopore are the ligand chemistry, which comprises the chemical structure of the ligand and the type of bonding to the silica surface, the ligand density, presence and extent of endcapping, the chemistry of the underlying silica surface and its degree of residual hydroxylation, and the pore diameter. The generated pore model (Figure 2.3.1) targets an average commercial RPLC column for the separation of low-molecular-weight compounds. Such a column typically features dimethyloctadecylsilyl (C_{18}) chains attached via a single bond to the silica surface at a ligand density of $\sim 3\,\mu mol\,m^{-2}$ plus

Table 2.3.2.: Properties of the generated cylindrical RPLC mesopore model.

	Interior	Exterior
Silica block xyz-dimensions (nm)	16.19; 15.79; 10.08	
Pore drilling direction	z	
Pore diameter (nm)	9.01	
Surface roughness[a] (nm)	0.08	0.00
Solvent reservoir z-dimension (nm)		5.50
Simulation box xyz-dimensions (nm)	16.19; 15.79; 21.08	
Inner pore volume[b] (nm^3)	642.97	
Solvent reservoir volume (nm^3)		2×1406.02
Surface area[b] (nm^2)	285.32	2×191.88
Surface chemistry before functionalization		
Number of single silanol groups	1054	1700
Number of geminal silanol groups	145	53
Number of siloxane bridges[c]	122	0
Total number of OH groups	1344	1806
Overall hydroxylation ($\mu mol\,m^{-2}$)	7.82	7.82
Surface chemistry after functionalization[d]		
Number of C_{18} chains	500	672
C_{18} density ($\mu mol\,m^{-2}$)	2.91	2.91
Number of TMS groups	121	163
TMS density ($\mu mol\,m^{-2}$)	0.70	0.71
Bonded-phase density ($\mu mol\,m^{-2}$)	3.61	3.61
Number of residual OH groups	723	971
Residual hydroxylation ($\mu mol\,m^{-2}$)	4.21	4.20
Generation time[e] (s)	33.5	

[a]Calculated as the standard deviation of the shortest distances between the central pore axis and the surface Si atoms, see Appendix. [b]Calculated using the actual pore size in z-dimension from line 1 and the actual pore diameter from line 3, see Appendix. [c]For the chosen drilling direction, pore diameter, and silica block size the maximum possible number of siloxane bridges on the interior and exterior surface is 584 and 742, respectively. [d]Binding sites in form of single or geminal silanol groups are equally targeted for bonded-phase coverage in the random selection process. [e]On 8 cores.

endcapping with trimethylsilyl (TMS) groups at an overall bonded-phase coverage of ~ 50%. Chromatographic silica is amorphous with an average surface hydroxylation of 7–8 µmol m^{-2} before functionalization and a residual surface hydroxylation of ~ 4 µmol m^{-2} after functionalization and endcapping. The surface chemistry comprises OH groups in form of single (isolated or vicinal) and geminal silanols as well as siloxane bridges. Chromatographic silica is known for its disordered pore structure and wide pore size distribution. Average pore diameters of 9–10 nm are fairly standard for RPLC columns intended for small molecules [22, 23].

Figure 2.3.1 shows the cylindrical RPLC mesopore model generated with PoreMS using parameters to replicate the conditions inside a standard RPLC column as outlined above. The input parameters are given in Table 2.3.1, the properties of the generated pore model are listed in detail in Table 2.3.2. The first set of parameters concerns the dimensions of the silica block, the targeted pore diameter, the drilling direction, and the length of the solvent reservoirs at each side of the silica block. The dimensions of the silica block were chosen to obtain sufficiently large interior and exterior pore surface areas required to produce good statistics for analyzing density, structure, and dynamics of solvent and solute molecules at the liquid–solid interface inside the mesopore (curved) or at the particle outside (planar). The pore diameter was set to 9 nm and the drilling direction was chosen along the z-axis so that the (111) face of β-cristobalite SiO_2, which owing to its surface hydroxylation has become the standard model for chromatographic silica surfaces [10, 33], faces the solvent reservoirs. The choice of drilling direction determines the maximal surface hydroxylation and thus provides options to realize different combinations of ligand density, endcapping, and residual hydroxylation on the pore surfaces. Incidentally, drilling along the z-direction also produces the smoothest interior surface (minimal surface roughness). However, the effects are rather weak. In a 3 nm cylindrical pore, the surface roughness is 0.11, 0.07, and 0.08 nm, when drilling in x-, y-, and z-direction, respectively, and the maximum possible surface hydroxylation is 9.12, 9.35, and 8.83 μmol m^{-2}. In a 9 nm cylindrical pore, the surface roughness is 0.11, 0.09, and 0.08 nm and the maximum possible surface hydroxylation is 9.50, 9.75, and 9.24 μmol m^{-2}. The equations used to calculate

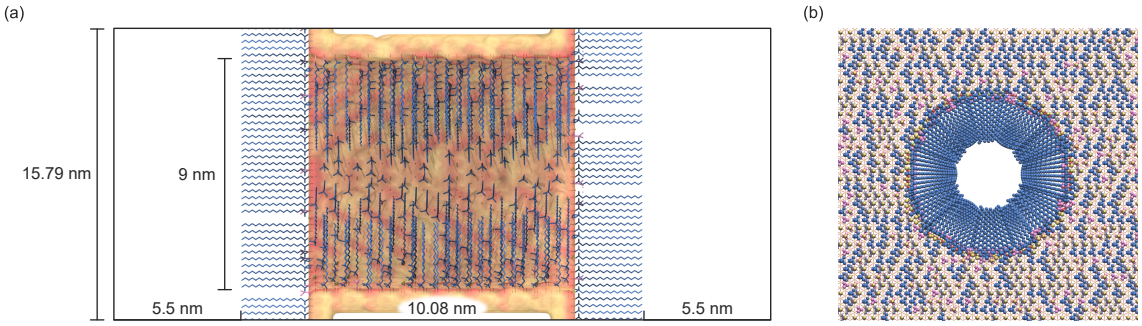

Figure 2.3.1.: Cylindrical RPLC mesopore model generated with PoreMS using the input parameters given in Table 2.3.1. (a) Side view of the simulation box indicating the length of the central silica block and the solvent reservoirs. (b) […] Front view […] of the pierced silica block containing the 9 nm diameter pore. The chemistry of the exterior surface is based on the (111) face of β-cristobalite silica. Exterior planar and interior curved surface are covered with the bonded phase consisting of C_{18} chains as the main ligand and TMS groups for endcapping. Bonded-phase groups are randomly distributed on the silica surface. Ligand and endcapping densities, residual surface hydroxylation, and further details are specified in Table 2.3.2. Colour code: Si, yellow lines; O, red lines; C_{18} chains, blue; TMS groups, magenta; residual surface silanol groups, yellow.

these properties are reported in the Appendix. The solvent reservoirs need to be long enough to observe and sample a statistically relevant stretch of bulk behaviour of the liquid mobile phase, that is, the extension of the organic-solvent rich layer has to be taken into account. The specific length required depends on the system studied (the properties of the functionalized silica as well as of the solvent mixture). The solvent reservoir length chosen for this example was informed by prior MD simulation studies using a slit-pore model of C_{18} functionalized silica equilibrated with water–acetonitrile mixtures [24, 25]. The chosen length should suffice for modelling bonded phases of similar or shorter chain length than C_{18} and common aqueous–organic mobile phases.

The second set of parameters concerns the functionalization and hydroxylation of the silica surface. The chosen drilling direction dictates that the exterior surface bears mostly single silanols; the rare geminal silanols are located at the rim to the pore entrance. Pore carving yields an interior surface with a higher percentage of geminal silanols than found outside. Consequently, the interior surface hydroxylation after carving is higher than at the exterior surface. The user has different options to arrive at a comparable residual hydroxylation of the interior and exterior surface while maintaining an identical main ligand density inside and outside: i) increase the inside endcapping density to reach an identical bonded-phase coverage inside and outside and thus an identical residual surface hydroxylation, ii) reduce the interior surface hydroxylation prior to surface functionalization through siloxane bridge building, and iii) use a combination of siloxane bridge building and endcapping density increase. In the present example, we selected the second option and introduced siloxane bridges on the interior surface to match its hydroxylation to that of the exterior surface after carving ($7.82\,\mu mol\,m^{-2}$). For the bonded phase, we chose C_{18} as the main ligand at a density of $2.91\,\mu mol\,m^{-2}$ and aimed for an overall coverage of 46% with respect to the total number of OH groups. These values translate to an endcapping density of 0.70–$0.71\,\mu mol\,m^{-2}$ and a residual surface hydroxylation of 4.20–$4.21\,\mu mol\,m^{-2}$. Generation of the cylindrical RPLC mesopore model took 33.5 s on eight cores.

2.3.2. Pore model for molecular heterogeneous catalysis

The pore model to study confinement effects in molecular heterogeneous catalysis aims to capture the size, the dominant geometry (cylinder), and the surface chemistry of typical ordered mesoporous silica materials, such as MCM [70] or SBA silica [36, 71]. The pore model targets the experimental concept of pore-size selective immobilization of a well-defined organometallic catalyst present on the interior, but not the exterior surface of a pore, as used recently to study olefin metathesis in confined geometries [17]. Experimentally, this selective immobi-

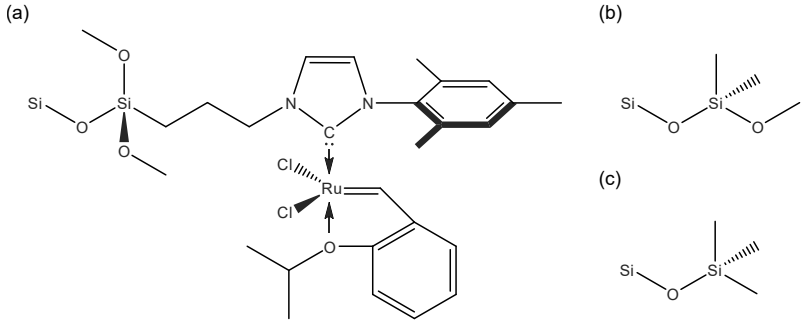

Figure 2.3.2.: Functionalization at the interior (a,b) and exterior surface (c) of the generated cylindrical silica pore model for heterogeneous catalysis. (a) Ruthenium catalyst, (b) dimethoxydimethylsilyl (DMDMS) group, (c) trimethylsilyl (TMS) group.

lization is achieved in a multi-step process, in which the interior pore surface is blocked by filling the mesopores with a polymer, then the exterior particle surface passivated by endcapping with TMS groups, and finally the interior pore surface unblocked again through polymer removal by Soxhlet extraction with ethanol [17, 72]. This procedure forces the catalyst to attach to the interior pore surface, as reactive groups at the particle outside are unavailable or inaccessible. Optionally, the interior pore surface can be further modified with dimethoxydimethylsilyl (DMDMS) groups to decrease the surface polarity and thus the polarity difference at the solid–liquid interface for working with the apolar solvents used in heterogeneous catalysis, such as benzene in the present example. Coverage of the interior pore surface with DMSMS groups also prevents that substrate and product molecules with polar groups can form hydrogen bonds to residual surface OH groups, which would lead to the enrichment of substrate and product molecules at the silica surface. Local enrichment close to the catalytic centre is highly undesirable as it carries the risk of oligomerization (substrate) and ring opening (product). The chemical structures of the three surface functionalizations are shown in Figure 2.3.2.

Figure 2.3.3 shows the cylindrical catalytic pore model of 4.8 nm diameter, generated with PoreMS using the parameters to replicate previous work [17]. The input parameters are given in Table 2.3.3, the properties of the generated pore model are listed in detail in Table 2.3.4. Contrary to the RPLC pore model, siloxane bridges were not introduced to the catalytic pore model. Endcapping with TMS groups was applied to the exterior surface, while the interior surface was functionalized with DMDMS groups. Additionally, two Ru-based catalyst groups were attached to the interior surface in point symmetry with respect to the centre of geometry of the pore. The hydroxylation of the interior surface prior to functionalization (8.84 $\mu mol\,m^{-2}$) recovers typical values assigned to amorphous silica [63–65]. One goal of functionalization was to create a largely apolar surface. The bulky DMDMS groups attached at a density of 5.54 $\mu mol\,m^{-2}$ effectively screen the residual OH groups on the silica surface (3.29 $\mu mol\,m^{-2}$) from access by solvent or solute molecules. The same effect is obtained on the exterior surface covered by TMS groups at a density of 4.47 $\mu mol\,m^{-2}$, resulting in a residual hydroxylation of 3.91 $\mu mol\,m^{-2}$. The catalyst density of 0.02 $\mu mol\,m^{-2}$ was chosen 4 to 5 times higher than in the experiment [17] to

Table 2.3.3.: Input parameters used to generate the catalytic mesopore model.

	Interior	Exterior
Target silica block xyz-dimensions (nm)	8.0; 8.0; 10.0	
Pore drilling direction	z	
Target pore diameter (nm)	4.8	
Solvent reservoir z-dimension (nm)		5.5
Target Surface hydroxylation[a] ($\mu mol\,m^{-2}$)	n/a	n/a
Siloxane bridges	No	No
Symmetry of catalyst molecules[b]	Point	
Number of catalyst groups	2	0
Main ligand	DMDMS	
Target ligand density ($\mu mol\,m^{-2}$)	5.54	
Endcapping with TMS groups	No	Yes
TMS ligand density ($\mu mol\,m^{-2}$)	0.00	4.48

[a]Generates the maximum possible surface hydroxylation. [b]The second possibility currently implemented is mirror symmetry. These two options can be applied to both cylinder and slit pores.

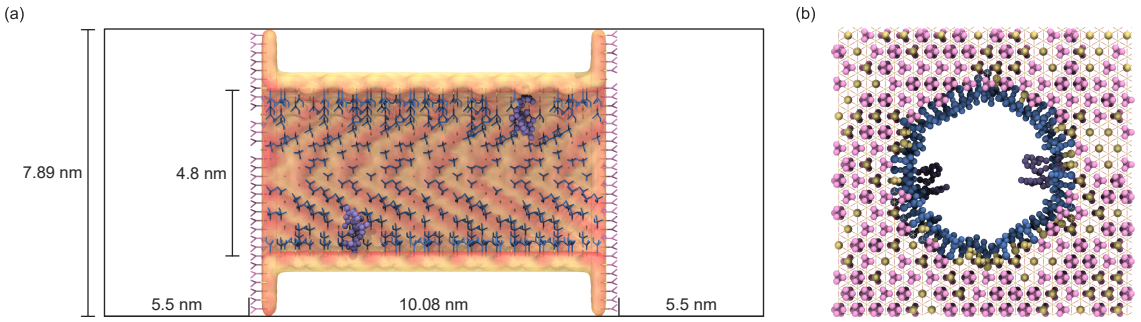

Figure 2.3.3.: Cylindrical catalytic mesopore model generated with PoreMS using the input parameters given in Table 2.3.3. (a) Side view of the simulation box indicating the length of the central silica block and the solvent reservoirs. (b) [...] Front view [...] of the pierced silica block containing the 4.8 nm pore. The chemistry of the exterior surface is based on the (111) face of β-cristobalite silica. The exterior planar and interior curved surfaces are covered with randomly distributed TMS and DMDMS groups, respectively. Two organometallic catalyst groups are attached to the interior surface in point symmetry with respect to the pore centre. The densities of all surface groups and further details are specified in Table 2.3.4. Colour code: Si atoms, yellow line; O atoms, red line; DMDMS groups, blue; TMS groups, magenta; catalyst, purple; residual surface silanol groups, yellow.

improve the statistical sampling in the simulation. In the experiment, a lower catalyst density was used to guard against interaction between reacting substrate molecules close to a catalyst group as well as between the catalyst groups themselves, as contrary to the pore model, a uniform spatial distribution could not be guaranteed. Generation of the cylindrical catalytic mesopore model took 8.2 s on eight cores.

2.4. Conclusion and Outloook

We introduced the open source software tool PoreMS to facilitate rapid model building of functionalized silica pores for Monte Carlo or molecular dynamics simulation studies of confinement effects in applications relying on functionalized mesoporous silica. The capability of PoreMS was demonstrated by the generation of explicit cylindrical pore models for reversed-phase liquid chromatography and molecular heterogeneous catalysis. In experimental practice, the actual surface chemistry of functionalized mesoporous silica depends on various aspects of the sample preparation and its details are not known with high accuracy. Therefore, we designed a modular program structure that allows high flexibility in carrying out different steps of the pore generation as well as individual customization of ligands. Moreover, the short generation time of a few seconds allows for an iterative fine-tuning towards a pore model that is both computationally tractable and representative of a targeted surface chemistry. The introduction of PoreMS should stimulate systematic molecular simulations research on confinement effects in functionalized cylindrical silica pores, as at present experimental advances relying on functionalized mesoporous silica materials are still largely empirically driven due to the lack of molecular-level information. Further development of PoreMS could address the implementation of alternative bulk silica structures.

Table 2.3.4.: Properties of the generated cylindrical catalytic mesopore model.

	Interior	Exterior
Silica block xyz-dimensions (nm)	8.10; 7.89; 10.08	
Pore drilling direction	z	
Pore diameter (nm)	4.80	
Surface roughness[a] (nm)	0.08	0.00
Solvent reservoir z-dimension (nm)		5.50
Simulation box xyz-dimensions (nm)	8.10; 7.89; 21.08	
Pore volume (nm^3)	182.66	
Solvent reservoir volume (nm^3)		2×351.43
Surface area (nm^2)	152.07	2×45.77
Surface chemistry before functionalization		
Number of single silanol groups	690	394
Number of geminal silanol groups	60	34
Number of siloxane bridges	0	0
Total number of OH groups	810	462
Overall hydroxylation ($\mu mol\,m^{-2}$)	8.85	8.38
Surface chemistry after functionalization		
Number of catalyst groups	2	0
Catalyst density ($\mu mol\,m^{-2}$)	0.02	0
Number of DMDMS groups	507	0
DMDMS density ($\mu mol\,m^{-2}$)	5.54	0
Number of TMS groups	0	246
TMS density ($\mu mol\,m^{-2}$)	0	4.47
Bonded-phase density ($\mu mol\,m^{-2}$)	5.56	4.47
Number of residual OH groups	301	216
Residual hydroxylation ($\mu mol\,m^{-2}$)	3.29	3.91
Generation time[b] (s)	8.2	

[a]Calculated as the standard deviation of the shortest distances between the central pore axis and the surface Si atoms. [b]On 8 cores.

References

[1] E. L. Margelefsky, R. K. Zeidan, and M. E. Davis. “Cooperative catalysis by silica-supported organic functional groups”. In: *Chem. Soc. Rev.* 37.6 (2008), pp. 1118–1126. DOI: 10.1039/b710334b.

[2] F. Marras et al. “Ordered mesoporous materials as solid supports for rhodium- diphosphine catalysts with remarkable hydroformylation activity”. In: *Chem. Commun.* 46.35 (2010), pp. 6587–6589. DOI: 10.1039/c0cc00924e.

[3] Z. ALOthman. “A Review: fundamental Aspects of Silicate Mesoporous Materials”. In: *Materials* 5.12 (2012), pp. 2874–2902. DOI: 10.3390/ma5122874.

[4] R. Narayan et al. “Mesoporous Silica Nanoparticles: a Comprehensive Review on Synthesis and Recent Advances”. In: *Pharmaceutics* 10.3 (2018), p. 118. DOI: 10.3390/pharmaceutics10030118.

[5] P. N. Diagboya and E. D. Dikio. “Silica-based mesoporous materials; emerging designer adsorbents for aqueous pollutants removal and water treatment”. In: *Microporous Mesoporous Mater.* 266 (2018), pp. 252–267. DOI: 10.1016/j.micromeso.2018.03.008.

[6] S. Molaei et al. “Highly Efficient Oxidative Coupling of Thiols and Oxidation of Sulfides in the Presence of MCM-41@Tryptophan-Cd and MCM-41@Tryptophan-Hg as Novel and Recoverable Nanocatalysts”. In: *Catal. Lett.* 148.7 (2018), pp. 1834–1847. DOI: 10.1007/s10562-018-2379-3.

[7] J. Siefker et al. “Confinement Facilitated Protein Stabilization As Investigated by Small-Angle Neutron Scattering”. In: *J. Am. Chem. Soc.* 140.40 (2018), pp. 12720–12723. DOI: 10.1021/jacs.8b08454.

[8] B. Dong et al. “Single Molecule Investigation of Nanoconfinement Hydrophobicity in Heterogeneous Catalysis”. In: *J. Am. Chem. Soc.* 142.31 (2020), pp. 13305–13309. DOI: 10.1021/jacs.0c05905.

[9] S. M. Melnikov et al. “Composition, Structure, and Mobility of Water–Acetonitrile Mixtures in a Silica Nanopore Studied by Molecular Dynamics Simulations”. In: *Anal. Chem.* 83.7 (2011), pp. 2569–2575. DOI: 10.1021/ac102847m.

[10] R. K. Lindsey et al. “Molecular simulation studies of reversed-phase liquid chromatography”. In: *J. Chromatogr. A* 1287 (2013), pp. 60–82. DOI: 10.1016/j.chroma.2013.02.040.

[11] S. M. Melnikov et al. “A Molecular Dynamics Study on the Partitioning Mechanism in Hydrophilic Interaction Chromatography”. In: *Angew. Chem. Int. Ed.* 51.25 (2012), pp. 6251–6254. DOI: 10.1002/anie.201201096.

[12] S. M. Melnikov et al. “A Molecular Dynamics View on Hydrophilic Interaction Chromatography with Polar-Bonded Phases: properties of the Water-Rich Layer at a Silica Surface Modified with Diol-Functionalized Alkyl Chains”. In: *J. Phys. Chem. C* 120.24 (2016), pp. 13126–13138. DOI: 10.1021/acs.jpcc.6b03799.

[13] J. Rybka et al. “A new view on surface diffusion from molecular dynamics simulations of solute mobility at chromatographic interfaces”. In: *Fluid Phase Equilib.* 407 (2016), pp. 177–187. DOI: 10.1016/j.fluid.2015.05.040.

[14] J. Rybka, A. Höltzel, and U. Tallarek. “Surface Diffusion of Aromatic Hydrocarbon Analytes in Reversed-Phase Liquid Chromatography”. In: *J. Phys. Chem. C* 121.33 (2017), pp. 17907–17920. DOI: 10.1021/acs.jpcc.7b04746.

[15] K. El Hage et al. “Molecular Mechanisms Underlying Solute Retention at Heterogeneous Interfaces”. In: *J. Phys. Chem. Lett.* 8.18 (2017), pp. 4600–4607. DOI: 10.1021/acs.jpclett.7b01966.

[16] K. El Hage, R. J. Bemish, and M. Meuwly. “From in silica to in silico: retention thermodynamics at solid-liquid interfaces”. In: *Phys. Chem. Chem. Phys.* 20.27 (2018), pp. 18610–18622. DOI: 10.1039/C8CP02899K.

[17] F. Ziegler et al. “Olefin Metathesis in Confined Geometries: a Biomimetic Approach toward Selective Macrocyclization”. In: *J. Am. Chem. Soc.* 141.48 (2019), pp. 19014–19022. DOI: 10.1021/jacs.9b08776.

[18] W. Zheng et al. “Enhanced Menshutkin S_N2 Reactivity in Mesoporous Silica: the Influence of Surface Catalysis and Confinement”. In: *J. Am. Chem. Soc.* 142.12 (2020), pp. 5636–5648. DOI: 10.1021/jacs.9b12666.

[19] T. Kobayashi et al. “Confined Ru-catalysts in a two phase heptane/ionic liquid solution: Modeling aspects”. In: *ChemCatChem* (2020). DOI: 10.1002/cctc.202001596.

[20] M. A. Nejad and H. M. Urbassek. “Diffusion of cisplatin molecules in silica nanopores: molecular dynamics study of a targeted drug delivery system”. In: *J. Mol. Graph. Model.* 86 (2019), pp. 228–234. DOI: 10.1016/j.jmgm.2018.10.021.

[21] A. Bruix et al. “First-principles-based multiscale modelling of heterogeneous catalysis”. In: *Nat. Catal.* 2.8 (2019), pp. 659–670. DOI: 10.1038/s41929-019-0298-3.

[22] P. Žuvela et al. “Column Characterization and Selection Systems in Reversed-Phase High-Performance Liquid Chromatography”. In: *Chem. Rev.* 119.6 (2019), pp. 3674–3729. DOI: 10.1021/acs.chemrev.8b00246.

[23] P. Žuvela et al. “Addition: column Characterization and Selection Systems in Reversed-Phase High-Performance Liquid Chromatography”. In: *Chem. Rev.* 119.7 (2019), pp. 4818–4818. DOI: 10.1021/acs.chemrev.9b00167.

[24] J. Rybka et al. “Molecular Dynamics Study of the Relation between Analyte Retention and Surface Diffusion in Reversed-Phase Liquid Chromatography”. In: *J. Phys. Chem. C* 123.6 (2019), pp. 3672–3681. DOI: 10.1021/acs.jpcc.8b11983.

[25] J. Rybka et al. “Stationary-Phase Contributions to Surface Diffusion in Reversed-Phase Liquid Chromatography: chain Length versus Ligand Density”. In: *J. Phys. Chem. C* 123.35 (2019), pp. 21617–21628. DOI: 10.1021/acs.jpcc.9b06160.

[26] R. Krishna. “Describing the Diffusion of Guest Molecules Inside Porous Structures”. In: *J. Phys. Chem. C* 113.46 (2009), pp. 19756–19781. DOI: 10.1021/jp906879d.

[27] Z. Brkljača et al. “Complementary Molecular Dynamics and X-ray Reflectivity Study of an Imidazolium-Based Ionic Liquid at a Neutral Sapphire Interface”. In: *J. Phys. Chem. Lett.* 6.3 (2015), pp. 549–555. DOI: 10.1021/jz5024493.

[28] R. Stepić et al. “Mechanism of the Water-Gas Shift Reaction Catalyzed by Efficient Ruthenium-Based Catalysts: a Computational and Experimental Study”. In: *Angew. Chem. Int. Ed.* 58.3 (2019), pp. 741–745. DOI: 10.1002/anie.201811627.

[29] N. Vučemilović-Alagić et al. “Insights from molecular dynamics simulations on structural organization and diffusive dynamics of an ionic liquid at solid and vacuum interfaces”. In: *J. Colloid Interface Sci.* 553 (2019), pp. 350–363. DOI: 10.1016/j.jcis.2019.06.017.

[30] A. García, I. I. Slowing, and J. W. Evans. “Pore diameter dependence of catalytic activity: *p*-nitrobenzaldehyde conversion to an aldol product in amine- functionalized mesoporous silica”. In: *J. Chem. Phys.* 149.2 (2018), p. 024101. DOI: 10.1063/1.5037618.

[31] M. Apostolopoulou et al. “Quantifying Pore Width Effects on Diffusivity via a Novel 3D Stochastic Approach with Input from Atomistic Molecular Dynamics Simulations”. In: *J. Chem. Theory Comput.* 15.12 (2019), pp. 6907–6922. DOI: 10.1021/acs.jctc.9b00776.

[32] U. Tallarek et al. “Multiscale Simulation of Diffusion in Porous Media: From Interfacial Dynamics to Hierarchical Porosity”. In: *J. Phys. Chem. C* 123.24 (2019), pp. 15099–15112. DOI: 10.1021/acs.jpcc.9b03250.

[33] L. Zhuravlev. “The surface chemistry of amorphous silica. Zhuravlev model”. In: *Colloids Surf. A* 173.1-3 (2000), pp. 1–38. DOI: 10.1016/S0927-7757(00)00556-2.

[34] S. M. Melnikov et al. “How Ternary Mobile Phases Allow Tuning of Analyte Retention in Hydrophilic Interaction Liquid Chromatography”. In: *Anal. Chem.* 85.18 (2013), pp. 8850–8856. DOI: 10.1021/ac402123a.

[35] J. S. Beck et al. “A new family of mesoporous molecular sieves prepared with liquid crystal templates”. In: *J. Am. Chem. Soc.* 114 (1992), pp. 10834–10843. DOI: 10.1021/ja00053a020.

[36] D. Zhao et al. “Triblock Copolymer Syntheses of Mesoporous Silica with Periodic 50 to 300 Angstrom Pores”. In: *Science* 279.5350 (1998), pp. 548–552. DOI: 10.1126/science.279.5350.548.

[37] F. Kleitz, S. H. Choi, and R. Ryoo. “Cubic *Ia3d* large mesoporous silica: synthesis and replication to platinum nanowires, carbon nanorods and carbon nanotubes”. In: *Chem. Commun.* (2003), pp. 2136–2137. DOI: 10.1039/B306504A.

[38] S.-J. Reich et al. “Hindrance Factor Expression for Diffusion in Random Mesoporous Adsorbents Obtained from Pore-Scale Simulations in Physical Reconstructions”. In: *Ind. Eng. Chem. Res.* 57.8 (2018), pp. 3031–3042. DOI: 10.1021/acs.iecr.7b04840.

[39] S.-J. Reich et al. “Hindered Diffusion in Ordered Mesoporous Silicas: insights from Pore-Scale Simulations in Physical Reconstructions of SBA-15 and KIT-6 Silica”. In: *J. Phys. Chem. C* 122.23 (2018), pp. 12350–12361. DOI: 10.1021/acs.jpcc.8b03630.

[40] J. L. Rafferty, J. Siepmann, and M. Schure. “The effects of chain length, embedded polar groups, pressure, and pore shape on structure and retention in reversed-phase liquid chromatography: molecular-level insights from Monte Carlo simulations”. In: *J. Chromatogr. A* 1216.12 (2009), pp. 2320–2331. DOI: 10.1016/j.chroma.2008.12.088.

[41] S. M. Melnikov et al. “Adsorption of Water-Acetonitrile Mixtures to Model Silica Surfaces”. In: *J. Phys. Chem. C* 117.13 (2013), pp. 6620–6631. DOI: 10.1021/jp312501b.

[42] J. J. Williams et al. “Effect of Surface Group Functionalization on the CO_2/N_2 Separation Properties of MCM-41: a Grand-Canonical Monte Carlo Simulation Study”. In: *J. Phys. Chem. C* 114.43 (2010), pp. 18538–18547. DOI: 10.1021/jp105464u.

[43] J. J. Williams, N. A. Seaton, and T. Düren. “Influence of Surface Groups on the Diffusion of Gases in MCM-41: a Molecular Dynamics Study”. In: *J. Phys. Chem. C* 115.21 (2011), pp. 10651–10660. DOI: 10.1021/jp112073z.

[44] E. Lowry and M. Piri. “Effect of Surface Chemistry on Confined Phase Behavior in Nanoporous Media: an Experimental and Molecular Modeling Study”. In: *Langmuir* 34.32 (2018), pp. 9349–9358. DOI: 10.1021/acs.langmuir.8b00986.

[45] M. D. Elola and J. Rodriguez. “Ionic mobility within functionalized silica nano-pores”. In: *J. Phys. Chem. C* 123.6 (2019), pp. 3622–3633. DOI: 10.1021/acs.jpcc.8b11444.

[46] B. Coasne et al. “Adsorption of Simple Fluid on Silica Surface and Nanopore: effect of Surface Chemistry and Pore Shape”. In: *Langmuir* 24.14 (2008), pp. 7285–7293. DOI: 10.1021/la800567g.

[47] C. D. Williams et al. “A new method for the generation of realistic atomistic models of siliceous MCM-41”. In: *Microporous Mesoporous Mater.* 228 (2016), pp. 215–223. DOI: 10.1016/j.micromeso.2016.03.034.

[48] J. Geske and M. Vogel. “Creating realistic silica nanopores for molecular dynamics simulations”. In: *Mol. Simul.* 43.1 (2017), pp. 13–18. DOI: 10.1080/08927022.2016.1221072.

[49] D. A. Keen and R. L. McGreevy. “Structural Modeling of Glasses using Reverse Monte-Carlo Simulation”. In: *Nature* 344 (1990), pp. 423–425. DOI: 10.1038/344423a0.

[50] F. R. Siperstein and K. E. Gubbins. “Synthesis and Characterization of Templated Mesoporous Materials using Molecular Simulation”. In: *Mol. Simul.* 27 (2001), pp. 339–352. DOI: 10.1080/08927020108031357.

[51] B. Coasne et al. “Adsorption of Simple Gases in MCM-41 Materials: The Role of Surface Roughness”. In: *Langmuir* 22 (2006), pp. 194–202. DOI: 10.1021/la051676g.

[52] S. Bhattacharya et al. “Modeling Micelle-Templated Mesoporous Material SBA-15: Atomistic Model and Gas Adsorption Studies”. In: *Langmuir* 25 (2009), pp. 5802–5813. DOI: 10.1021/la801560e.

[53] C. Schumacher et al. “Generation of Atomistic Models of Periodic Mesoporous Silica by Kinetic Monte Carlo Simulation of the Synthesis of the Material”. In: *J. Phys. Chem. B* 110.1 (2006), pp. 319–333. DOI: 10.1021/jp0551871.

[54] C. A. Ferreiro-Rangel et al. “Kinetic Monte Carlo Simulation of the Synthesis of Periodic Mesoporous Silicas SBA-2 and STAC-1: Generation of Realistic Atomistic Models”. In: *J. Phys. Chem. C* 116 (2012), pp. 20966–20974. DOI: 10.1021/jp307610a.

[55] M. Jorge et al. “Modelling the self-assembly of silica-based mesoporous materials”. In: *Mol. Simul.* 44 (2018), pp. 435–452. DOI: 10.1080/08927022.2018.1427237.

[56] Y. Han, I. I. Slowing, and J. W. Evans. “Surface structure of linear nanopores in amorphous silica: Comparison of properties for different pore generation algorithms”. In: *J. Chem. Phys.* 153 (2020), p. 124708. DOI: 10.1063/5.0021317.

[57] M. W. Thompson et al. “Towards molecular simulations that are transparent, reproducible, usable by others, and extensible (TRUE)”. In: *Mol. Phys.* 118 (2020), e1742938. DOI: 10.1080/00268976.2020.1742938.

[58] M. J. Abraham et al. “GROMACS: high performance molecular simulations through multi-level parallelism from laptops to supercomputers”. In: *SoftwareX* 1-2 (2015), pp. 19–25. DOI: 10.1016/j.softx.2015.06.001.

[59] H. Kraus and N. Hansen. *PoreMS: v0.2.0*. Version v0.2.0. 2020. DOI: 10.5281/zenodo.3984865.

[60] R. W. G. Wyckoff. “Crystal structure of high temperature cristobalite”. In: *Am. J. Sci.* s5-9.54 (1925), pp. 448–459. DOI: 10.2475/ajs.s5-9.54.448.

[61] R. W. G. Wyckoff. “Die Kristallstruktur von β-Cristobalit (bei hohen Temperaturen stabile Form)”. In: *Z. Kristallogr.* 62.1-6 (1925), pp. 189–200. DOI: 10.1524/zkri.1925.62.1.189.

[62] D. R. Peacor. “High-temperature single-crystal study of the cristobalite inversion”. In: *Z. Kristallogr.* 138.1-4 (1973), pp. 274–298. DOI: 10.1524/zkri.1973.138.1-4.274.

[63] P. Villars and L. D. Calvert. *Pearson's handbook of crystallographic data for intermetallic phases*. 2nd ed. Materials Park, OH: ASM International, 1991.

[64] K. K. Unger. *Porous silica, its properties and use as support in column liquid chromatography*. Journal of chromatography library v. 16. Amsterdam: Elsevier, 1979.

[65] E. F. Vansant, P. Van Der Voort, and K. C. Vrancken. *Characterization and Chemical Modification of the Silica Surface*. Studies in surface science and catalysis v. 93. Amsterdam: Elsevier, 1995.

[66] D. A. Litton and S. H. Garofalini. "Modeling of hydrophilic wafer bonding by molecular dynamics simulations". In: *J. Appl. Phys.* 89.11 (2001), pp. 6013–6023. DOI: 10.1063/1.1351538.

[67] J. Wang et al. "Automatic atom type and bond type perception in molecular mechanical calculations". In: *J. Mol. Graph. Model.* 25.2 (2006), pp. 247–260. DOI: 10.1016/j.jmgm.2005.12.005.

[68] T. S. Gulmen and W. H. Thompson. "Testing a Two-State Model of Nanoconfined Liquids: conformational Equilibrium of Ethylene Glycol in Amorphous Silica Pores". In: *Langmuir* 22.26 (2006), pp. 10919–10923. DOI: 10.1021/la062285k.

[69] A. Abramov and S. Iglauer. "Application of the CLAYFF and the DREIDING Force Fields for Modeling of Alkylated Quartz Surfaces". In: *Langmuir* 35.17 (2019), pp. 5746–5752. DOI: 10.1021/acs.langmuir.9b00527.

[70] X. S. Zhao et al. "Comprehensive Study of Surface Chemistry of MCM-41 Using 29Si CP/-MAS NMR, FTIR, Pyridine-TPD, and TGA". In: *J. Phys. Chem. B* 101.33 (1997), pp. 6525–6531. DOI: 10.1021/jp971366+.

[71] G. J. A. Soler-Illia et al. "Block copolymer-templated mesoporous oxides". In: *Curr. Opin. Colloid Interface Sci.* 8.1 (2003), pp. 109–126. DOI: 10.1016/S1359-0294(03)00002-5.

[72] J. D. Webb et al. "Selective functionalization of the mesopores of SBA-15". In: *Microporous Mesoporous Mater.* 203 (2015), pp. 123–131. DOI: 10.1016/j.micromeso.2014.10.032.

3. An atomistic view on the uptake of aromatic compounds by cyclodextrin immobilized on mesoporous silica

The content of this chapter is a literal quote of the publication

H. Kraus and N. Hansen, Adsorption, 28(3-4), 125-136, 2022

The effect of immobilized β-cyclodextrin (bCD) molecules inside a mesoporous silica support on the uptake of benzene and *p*-nitrophenol from aqueous solution was investigated using all-atom molecular dynamics (MD) simulations. The calculated adsorption isotherms are discussed with respect to the free energies of binding for a 1:1 complex of bCD and the aromatic guest molecule. The adsorption capacity of the bCD-containing material significantly exceeds the amount corresponding to a 1:1 binding scenario, in agreement with experimental observations. Beside the formation of 1:2 and, to a lesser extent, 1:3 host:guest complexes, also host-host interactions on the surface as well as more unspecific host-guest interactions govern the adsorption process. The demonstrated feasibility of classical all-atom MD simulations to calculate liquid phase adsorption isotherms paves the way to a molecular interpretation of experimental data that are too complex to be described by empirical models.

3.1. Introduction

Cyclodextrins (CDs) are cyclic oligosaccharides with conical shape built of (1-4)-linked α-D-glucopyranoside units. Their hydrophilic outer surface renders them soluble in water, while the hydrophobic interior can accommodate hydrophobic compounds. Therefore, they are employed in the removal of pollutants from aqueous media [1, 2], as chiral selectors [3] or in (asymmetric) supramolecular catalysis [4–10] among many other fields of applications including the use of cyclodextrins as drug delivery agents or as building blocks in the design of dynamic and adaptive materials [11, 12]. By tuning the size and shape of the hydrophobic cavity through derivatization of the native cyclodextrins the selectivity towards the target compounds can be increased [13]. In addition, the ease of functionalization of their scaffold allows to introduce additional catalytic groups or binding sites in specific positions [14]. Together with the solvent used and a possible immobilization of the cyclodextrins on a solid support, a complex multidimensional design problem emerges. Several approaches can be envisioned to produce CD-functionalized materials. The first involves cross-linking of CDs into polymers using C-OH linkers [15]. A second approach utilizes the coating or grafting of CD moieties onto a stationary phase such as organic polymers or silica gel [16]. A third type of material is based on a mesoporous silica support. Mesoporous silicas with chemically attached macrocyclic moieties were successfully prepared by sol-gel condensation of tetraethyl orthosilicate and β-cyclodextrin-silane in the presence of a structure directing agent [17–20], resulting in silica-based materials that possess a uniform framework mesoporosity with defined nanoscaled cavities. The ability of removing aromatic compounds from an aqueous phase was investigated, and it was concluded that the synthesized materials is promising for this purpose [17, 18, 20].

Molecular modelling approaches are particularly feasible to study the delicate balance between the various intermolecular forces determining macroscopic behavior and allow a fundamental understanding at the molecular level. Gas adsorption in microporous materials such as zeolites [21, 22] or other nanostructured solids [23] has been studied for more than 45 years in particular using classical molecular simulations. The combination of molecular simulation techniques with experimental measurements allows to examine in detail fundamental diffusion processes within nanoporous solids and allows to better understand nano-confinement effects [24]. The investigation of liquid phase systems was largely driven by studies related to liquid chromatography, i.e., partitioning behavior of (multicomponent) mixtures at a solid surface functionalized for example with alkyl chains [25–29]. Other studies used coarse-grained molecular dynamics (MD) simulations to investigate protein adsorption on solid supports [30, 31] including the calculation of adsorption isotherms. An atomistic simulation study of enantiomeric separation of (R)- and (S)-ibuprofen in methanol solvent by means of immobilized cyclodextrins in a slit shaped model pore was reported recently [32]. Therefore, molecular simulation has evolved toward a promising tool to study liquid phase separation processes that are too complex to be described by phenomenological models [33].

The aim of the present work is to investigate the feasibility of all-atom classical MD simulations to reconcile liquid phase adsorption experiments with theoretical predictions. For this purpose adsorption of benzene and *p*-nitrophenol from aqueous solutions onto cyclodextrin-functionalized mesoporous silica support is modelled and analyzed. Binding free enthalpy calculations in bulk solvent are related to the Henry regime of the adsorption isotherm on the functionalized material. The interpretation of experimentally observed adsorption isotherms is discussed in view of the underlying molecular level picture.

3.2. Methodology

3.2.1. Calculation of binding free enthalpies and rate constants in bulk solution

Two approaches were employed to calculate binding free enthalpies, an unbiased (counting) one and a biased (double decoupling) one.
In the unbiased approach, referred to as direct counting (DC), the occurrences of bound, N_b, and unbound, N_u, instances during long ($t \geq 10\,\mu\mathrm{s}$) standard MD simulations of one host-guest pair solvated in a box of water are counted. The binding free enthalpy is then obtained from [34]

$$\Delta G^\mathrm{DC} = -RT \ln \frac{N_\mathrm{b}}{N_\mathrm{u}} - RT \ln \frac{V_\mathrm{box}}{V^0} \tag{3.2.1}$$

with standard state volume $V^0 = 1.661\,\mathrm{nm}^3$ and average volume of the simulation box V_box. In addition, average bound $\langle t_b \rangle$ and unbound $\langle t_u \rangle$ residence times can be calculated, yielding association k_on and dissociation k_off rates [34]

$$k_\mathrm{on} = \frac{1}{\langle t_\mathrm{u} \rangle C_\mathrm{g}}, \quad k_\mathrm{off} = \frac{1}{\langle t_\mathrm{b} \rangle} \tag{3.2.2}$$

with guest molecule concentration C_g. The binding free enthalpy can then be determined using these rate constants (RC)

$$\Delta G^\mathrm{RC} = -RT \ln \frac{k_\mathrm{on} C^0}{k_\mathrm{off}} = -RT \ln \frac{\langle t_\mathrm{b} \rangle}{\langle t_\mathrm{u} \rangle} - RT \ln \frac{V_\mathrm{box}}{V^0} \tag{3.2.3}$$

with standard state concentration $C^0 = 1\,\mathrm{mol\,l}^{-1}$.
In order to identify bound and unbound instances, the host and guest molecule structures need to be geometrically reduced to comparable reference points. Using the different glucopyranose units, the conical shape of cyclodextrin was first reduced to three main circles, one running through the oxygen atoms of the primary hydroxyl groups, one central circle passing through the central carbon atoms, and one circle connecting the oxygen atoms of the secondary hydroxyl groups. This system was then further reduced to a three point system based on the centers of mass of the different circles. Similarly, the two guest molecules were also reduced to a three point system as illustrated in figure 3.2.1.

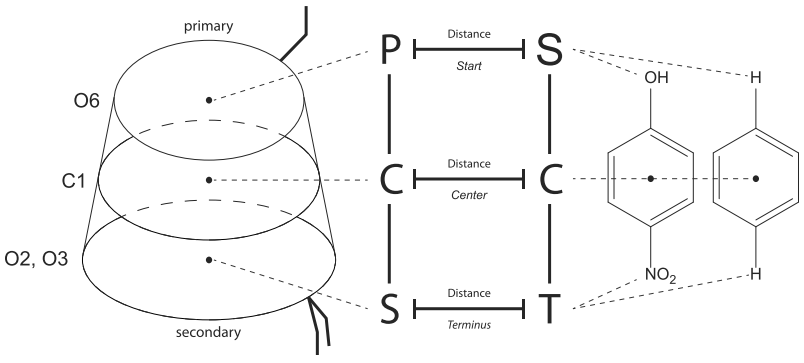

Figure 3.2.1.: Geometrical representation of the cyclodextrin and guest molecule structures by a three point system.

To determine whether a configuration is in a bound state, a spatial cut-off was defined for the central distance within which the guest molecule is assumed to be bound to the host molecule.

Monitoring the angle of the two three point systems provides the orientation in which the guest molecule is bound to the host. Observing the bound and unbound state over time results into bound and unbound instances of different duration. Averaging over these instances yields time averages $\langle t_\mathrm{b} \rangle$ and $\langle t_\mathrm{u} \rangle$. Optionally, a temporal cut-off can be introduced that removes bound and unbound instances with a smaller residence time from the averaging. The impact of the temporal cut-off is shown in the supplementary material in table S1 and discussed below.
The second method used for calculating the binding free enthalpy was double decoupling (DD) [35]. As illustrated in figure 3.2.2 the process is divided into two parts. First, the free enthalpy difference $\Delta G_\mathrm{u}^{\mathrm{M}\rightarrow\mathrm{M}'}$ is calculated, resulting from decoupling the unbound state u, i.e., turning off the intermolecular interactions with the environment ($\mathrm{M}\rightarrow\mathrm{M}'$) of the guest molecule in a box of water while preserving intramolecular interactions. $\Delta G_\mathrm{u}^{\mathrm{M}\rightarrow\mathrm{M}'}$ is equal to the negative hydration free enthalpy $-\Delta G_\mathrm{hyd}^\mathrm{M}$. Second, the free enthalpy difference $\Delta G_\mathrm{b}^{\mathrm{M}\rightarrow\mathrm{M}'}$ is calculated by decoupling the bound state (b), i.e., turning off intermolecular interactions of the guest molecule with the environment in a simulation with a host-guest complex in solvent. The latter is divided into three contributions, the difference $\Delta G_{\mathrm{b}\rightarrow\mathrm{tor}}^\mathrm{M}$ by turning on translational and orientational restraints (tor) between host and guest in order to guarantee that the guest molecule stays within the host when turning off intermolecular interactions $\Delta G_\mathrm{tor}^{\mathrm{M}\rightarrow\mathrm{M}'}$ and lastly turning off the initial restraints $\Delta G_\mathrm{tor}^{\mathrm{M}'}$. The first two free enthalpy differences can be determined through molecular dynamics simulations by gradually turning on restraints and then turning off the interactions. This was done in one continuous simulation resulting into a combined value $\Delta G_{\mathrm{b}\rightarrow\mathrm{tor}}^{\mathrm{M}\rightarrow\mathrm{M}'} = \Delta G_{\mathrm{b}\rightarrow\mathrm{tor}}^\mathrm{M} + \Delta G_\mathrm{tor}^{\mathrm{M}\rightarrow\mathrm{M}'}$. The free enthalpy from turning off the restraints from the non-interacting guest molecule can be calculated analytically. According to the thermodynamic cycle [36, 37] shown in figure 3.2.2, the summation over the whole cycle is equal to zero thus resulting into

$$\begin{aligned}\Delta G^\mathrm{DD} = \Delta G_{\mathrm{u}\rightarrow\mathrm{b}}^\mathrm{M} &= -\Delta G_\mathrm{hyd}^\mathrm{M} - \Delta G_{\mathrm{b}\rightarrow\mathrm{tor}}^\mathrm{M} - \Delta G_\mathrm{tor}^{\mathrm{M}\rightarrow\mathrm{M}'} - \Delta G_\mathrm{tor}^{\mathrm{M}'} \\ &= -\Delta G_\mathrm{hyd}^\mathrm{M} - \Delta G_{\mathrm{b}\rightarrow\mathrm{tor}}^{\mathrm{M}\rightarrow\mathrm{M}'} - \Delta G_\mathrm{tor}^{\mathrm{M}'}.\end{aligned} \tag{3.2.4}$$

The procedure of decoupling the bound ligand was adopted from Boresch and Karplus [38]. Six atoms were chosen, three from the host a, b, c and three from the guest molecule A, B, C, see Fig. S2 in the supplementary material. Using these atoms a total of six harmonic restraints have been applied, a distance $r_{aA,0}$, two angles $\theta_{A,0}$, $\theta_{B,0}$, and three dihedral angles $\phi_{A,0}$, $\phi_{B,0}$, $\phi_{C,0}$. The values for the reference distance and angles have been determined by averaging the distances and angles of host-guest complexes throughout the unbiased simulations. The analytical part for turning off these restraints is then given by

$$\Delta G_\mathrm{tor}^{\mathrm{M}'} = -RT\ln\left[\frac{8\pi V^0 (K_r K_{\theta_A} K_{\theta_B} K_{\phi_A} K_{\phi_B} K_{\phi_C})^{\frac{1}{2}}}{r_{aA,0}^2 \sin\theta_{A,0} \sin\theta_{B,0} (2\pi RT)^3}\right] \tag{3.2.5}$$

with force constants K_i. Depending on the guest molecule, distinct binding configurations may become apparent. In this case the decoupling has to be performed for each of those states k. The total binding free enthalpy is then calculated by a logarithmic mean [39]

$$\Delta \bar{G}_{\mathrm{u}\rightarrow\mathrm{b}}^\mathrm{M} = -RT\ln\left[\sum_k \exp\left(\frac{\Delta G_{\mathrm{u}\rightarrow\mathrm{b},k}^\mathrm{M}}{RT}\right)\right]. \tag{3.2.6}$$

3.2.2. Immobilization of cyclodextrins

For immobilizing cyclodextrin in a silica-pore, two linker concepts used by Huq et al. [17] and Trofymchuk et al. [20] were utilized for generating the molecule structure for simulation. Since

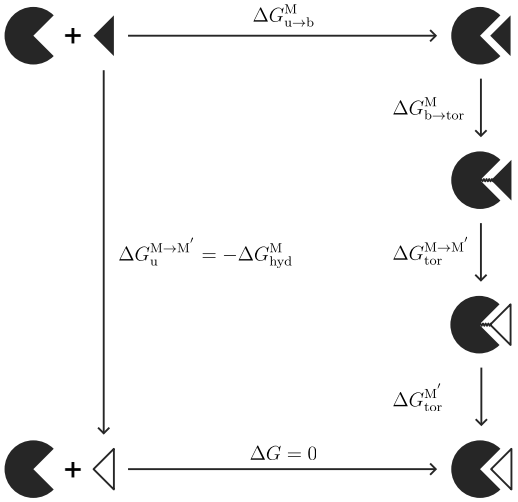

Figure 3.2.2.: Thermodynamic cycle for calculating the binding free enthalpy of a host-guest system. Hereby M indicates that the guest molecule is possessing full intermolecular (environmental) interaction (full triangle), while M' denotes the guest molecule possessing only intramolecular interactions (framed triangle). Index u stands for an unbound state, b for the bound state, and tor for translational and orientational restraints.

the native cyclodextrin molecules were described by the Amber-compatible q4md-CD force field [40], the linker molecules were parametrized via AmberTools20 [41]. The parametrized linker structures were then appended to the cyclodextrin topology while accounting for additional connectivity parameters which are listed in the supplementary material in table S3. The molecular structures of the linkers are illustrated in figure 3.2.3.

3.2.3. Simulated systems

For calculating the binding free enthalpy by direct counting and via rate constants, long unbiased simulations were conducted in the NpT ensemble with one guest molecule, benzene or *p*-nitrophenol, respectively, and one host molecule, β-cyclodextrin, solvated in 1000 water molecules. Simulations for determining the binding free enthalpy by double decoupling were initialized from a configuration of the long unbiased simulations containing a host-guest complex in the bound state. The hydration free enthalpy was calculated from a similar system without a host molecule. The binding free enthalpy was calculated for two temperatures, 298 K and 350 K at a constant pressure of 1 bar.

In order to generate and functionalize silica-pores as shown in figure 3.2.4, the PoreMS Python package [42] version 0.2.2 [43] was utilized. The systems are composed of a cylindrical pore of 4.05 nm diameter carved out of a (6.07, 6.14, 10.08) nm (x, y, z) β-cristobalite block. A bulk reservoir with the length of 5 nm was attached on each side of the pore structure. The internal surface was functionalized with 0.07 and 0.14 µmol m^{-2} β-cyclodextrin, respectively. For the simulations representing the system by Trofymchuk et al. [20], additional 0.11 and 0.22 µmol m^{-2} of the propylamine group was added to the internal surface, which was experimentally used to immobilize cyclodextrin. This resulted into a total hydroxylation density (OH-groups on the surface) of 8.56 µmol m^{-2} on the internal surface and 8.82 µmol m^{-2} on the external surface. Further properties of the pore are listed table 3.2.1.

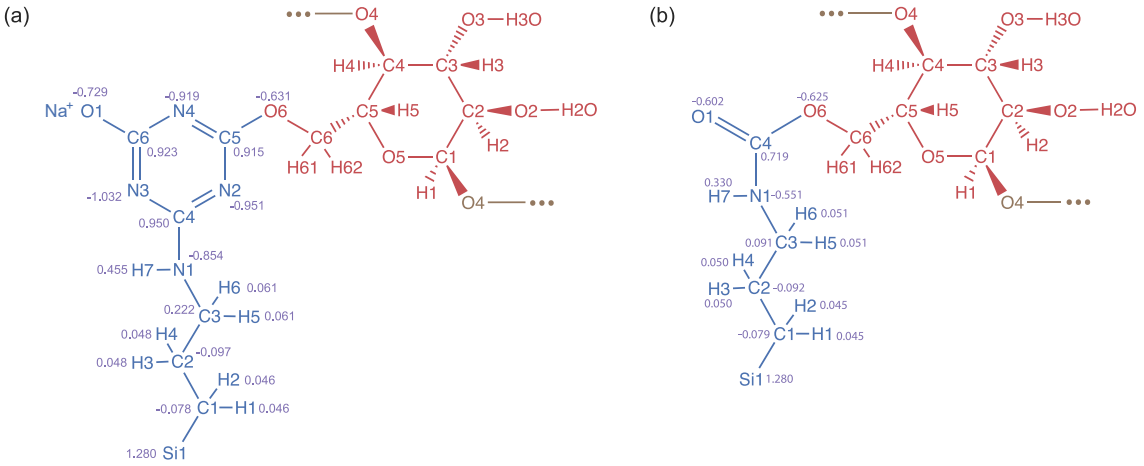

Figure 3.2.3.: Atom names and partial atomic charges (purple) of cyclodextrin (red) with a pore surface linker (blue) used by (a) Huq et al. [17] and referred to as L1 in the present work, with a total charge beyond the `Si1`-atom (not counting the Na^+) of $-1.32\,e$ and by (b) Trofymchuk et al. [20], referred to as L2 in the present work, with a total charge of $-0.32\,e$.

The topology parameters for the lattice silicon and oxygen atoms and silanol groups are taken from Gulmen and Thompson [44] and are shown in the supplementary material in table S4. These systems were simulated in the NVT ensemble by achieving the desired density and pressure in a system with a specific concentration of guest molecules, through iteratively filling the simulation box with solute molecules until the difference between the density within the bulk-reservoir of the pore system and a preliminary NpT simulation at a pressure of 1 bar with the same solvent concentration, is less than one percent. Benzene adsorption isotherms were determined for two temperatures, 298 K and 350 K and two cyclodextrin surface densities. For *p*-nitrophenol an adsorption isotherm was calculated at 350 K using the pore with the higher cyclodextrin surface density.

3.2.4. Simulation parameters

Simulations were prepared using the open source package PoreSim [45] which generates folder structures and other practical scripts for pore simulations. The simulation suite GROMACS 2016.5 [46, 47] was used for all simulations, while PLUMED 2.5 [48, 49] was utilized to extract specific distances and angles. Based on earlier work [50, 51], the general Amber force field (GAFF) [52] was chosen to describe intra- and intermolecular interactions. This is further backed up by the quality of the GAFF-compatible force field q4md-CD for cyclodextrin simulations [40, 53]. In order to verify the quality of the force-fields for the solute molecules *p*-nitrophenol and benzene, which were studied in the work of Huq et al. [17] and Trofymchuk et al. [20], validating simulations were carried out based on topologies provided by Mobley et al. [54]. Water was described by the TIP3P model [55] as the relatively large pore diamter of 4.05 nm is not expected to lead to a strong confinement effect at ambient pressure [56].
All MD simulations were performed under periodic boundary conditions. Temperature was controlled using the Nosé-Hoover thermostat [57, 58] with a coupling constant of 1 ps, while pressure for simulations in the NpT ensemble was controlled by the Parrinello-Rahman barostat [59, 60] with a coupling constant of 5.0 ps and compressibility of $4.5 \times 10^{-5}\,\mathrm{bar}^{-1}$. Bond lenghts between heavy atoms and hydrogens were constrained with the LINCS algorithm [61,

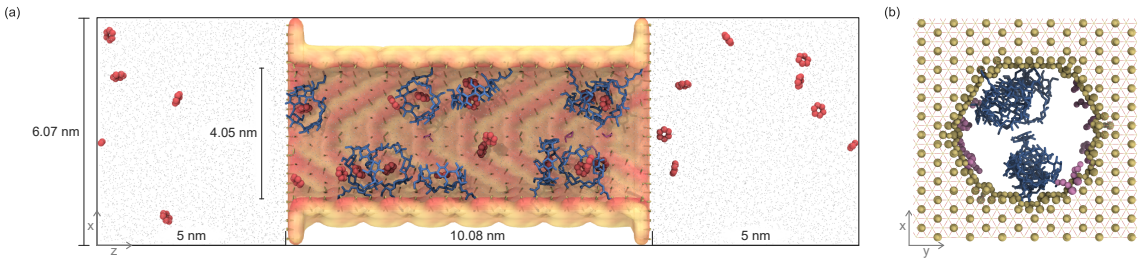

Figure 3.2.4.: Pore system functionalized with β-cyclodextrin using the surface linker used by Trofymchuk et al. [20]. (a) Side view of the simulation box indicating the length of the central silica block and the solvent reservoirs. (b) Front view of the pierced silica block containing the 4 nm diameter pore. The chemistry of the exterior surface is based on the (111) face of β-cristobalite silica. Bonded-phase groups are randomly distributed on the silica surface. Ligand densities, residual surface hydroxylation, and further details are specified in Table 3.2.1. Colour code: Si, yellow lines; O, red lines; β-cyclodextrin, blue; propylamine groups, magenta; surface silanol groups, yellow.

62] with an order of 4. Short-range electrostatic and Lennard-Jones parameters were evaluated up to a cutoff distance of 1.4 nm. Analytical dispersion corrections for energy and pressure were included. Long-range electrostatic interactions were treated with the particle-mesh Ewald algorithm [63, 64].
The long unbiased simulations were run for 10 µs with a time-step of 2 fs after a total equilibration time of 3 ns. Decoupling simulations used a total of 25 intermediate states (λ-points) for a slow equidistant deactivation of the intermolecular interactions of the guest molecule with its environment while preserving intramolecular interactions. Each λ-point was run for 1 ns with a time-step of 2 fs. During the simulation of the pore systems, silicon and oxygen grid atoms were frozen in their position to preserve the original pore shape, this includes the silicon atom of surface groups. For these systems a trajectory length of 1 µs was generated with a time-step of 1 fs and a total equilibration time of 100 ns.

3.2.5. Analysis

Distances and angles between the reference systems during the long unbiased simulations were extracted using PLUMED. The determination of bound and unbound states, and the calculation of the binding free enthalpy using the direct counting and rate constants method was conducted by in-house Python scripts. For determining the free enthalpy differences from decoupling simulations thermodynamic integration [65] was utilized. The density profiles and adsorption isotherms were calculated using the PoreAna package version 0.2.0 [66], developed during this project in object oriented Python 3 to complement the PoreMS package. Radial density and diffusion profiles within the pore were calculated by dividing the cylindrical shape into radial volume slices

$$V_i = \pi z (r_i^2 - r_{i-1}^2) \tag{3.2.7}$$

with pore length z and radius r_i of slice i. The number density ρ_i is then determined by counting the number of molecules N_i within each slice during the simulation, resulting into

$$\rho_i = \frac{N_i}{V_i} = \frac{N_i}{\pi z} \frac{1}{r_i^2 - r_{i-1}^2}. \tag{3.2.8}$$

Table 3.2.1.: Properties of the cylindrical mesopore model before and after functionalization (func), generated as described by Trofymchuk et al. [20], with surface densities ($\mu mol\,m^{-2}$) and pore dimensions (nm).

	Interior	Exterior
Silica block xyz-dim.	6.07; 6.14; 10.08	
Pore drilling direction	z	
Pore diameter	4.05	
Surface roughness[a]	0.08	0.00
Solvent reservoir z-dim.		5.00
Simulation box xyz-dim.	6.07; 6.14; 20.08	
Pore volume	129.74	
Solvent reservoir volume		2×186.36
Surface area	128.16	2×24.39
Surface chemistry before func.		
Num. of single silanol groups	553	205
Num. of geminal silanol groups	68	27
Num. of siloxane bridges	0	0
Total number of OH groups	689	259
Overall hydroxylation	8.93	8.82
Surface chemistry after func.		
Num. of β-cyclodextrin groups[b]	11	0
β-cyclodextrin density	0.14	0
Num. of propylamine groups	17	0
Propylamine density	0.22	0
Bonded-phase density	0.36	0.00
Num. of residual OH groups	661	259
Residual hydroxylation	8.56	8.82

[a]Calculated as the standard deviation of the shortest distances between the central pore axis and the surface Si atoms. [b]Pore variants with 5 and 11 β-cyclodextrin groups were prepared in this work.

Adsorption isotherms describe the amount of solute molecules adsorbed on the surface N^{pore} as a function of the amount of solute in the bulk phase N^{bulk} and are therefore, similarly to the density, determined from counting the number of molecules within the pore and within the bulk reservoirs normalized by the number of frames

$$\langle N\rangle^{\text{pore}} = \frac{1}{N_{\text{F}}}\sum_{j=1}^{N_{\text{F}}} N_j^{\text{pore}},\ \langle N\rangle^{\text{bulk}} = \frac{1}{N_{\text{F}}}\sum_{j=1}^{N_{\text{F}}} N_j^{\text{bulk}}. \tag{3.2.9}$$

with the number of molecules N_j within the pore or bulk phase at frame $j = 1,\ldots,N_{\text{F}}$. These values are then converted to surface and volume concentrations respectively based on the volume of the pore system and inner pore surface.
The diffusion coefficient $D_{\parallel,i}$ parallel to the pore surface was determined from the slope of the mean square displacement $\Delta_i(t)$ over an observation time of 4-20 ps within each bin with a tolerance of ±1 bins

$$D_{\parallel,i} = \frac{1}{2}\frac{d\Delta_i(t)}{dt}. \tag{3.2.10}$$

By weighting the axial diffusion profile $D_{\parallel,i}$ with the density profile ρ_i along the radius r, a mean diffusion coefficient $\langle D_\parallel \rangle$ can be calculated

$$\langle D_\parallel \rangle = \frac{\sum \rho_i D_{\parallel,i} A_i}{\sum \rho_i A_i} = \frac{\sum \rho_i D_{\parallel,i} (r_i^2 - r_{i-1}^2)}{\sum \rho_i (r_i^2 - r_{i-1}^2)} \tag{3.2.11}$$

with the cross-sectional area

$$A_i = \pi (r_i^2 - r_{i-1}^2) \tag{3.2.12}$$

of bin i.

3.2.6. Langmuir model

Considering a simulation set-up as shown in Fig. 4 but with only a single cyclodextrin molecule bound to the inner pore surface and a single guest molecule present in the simulation box, the direct counting method (Eq. (3.2.1)) would result in the same standard binding free enthalpy as in the bulk phase simulation given that the pore walls do not interact substantially with the guest molecule. Therefore, the ratio of bound to unbound samples in the pore system would be

$$\left(\frac{N_\mathrm{b}}{N_\mathrm{u}}\right)_\mathrm{pore} = \left(\frac{N_\mathrm{b}}{N_\mathrm{u}}\right)_\mathrm{bulk} \cdot \frac{V_\mathrm{box}^\mathrm{bulk}}{V_\mathrm{box}^\mathrm{pore}} \tag{3.2.13}$$

where the sub- or superscript 'pore' refers to the entire accessible volume of the simulation box, containing the pore and the solvent reservoirs. Rearranging to

$$N_\mathrm{b}^\mathrm{pore} = \left(\frac{N_\mathrm{u}}{V_\mathrm{box}}\right)_\mathrm{pore} \cdot \left(\frac{N_\mathrm{b}}{N_\mathrm{u}}\right)_\mathrm{bulk} \cdot V_\mathrm{box}^\mathrm{bulk} \tag{3.2.14}$$

and replacing the two rightmost terms by means of Eq. 1 results in

$$N_\mathrm{b}^\mathrm{pore} = \left(\frac{N_\mathrm{u}}{V_\mathrm{box}}\right)_\mathrm{pore} \cdot V^0 \cdot \exp\left(-\frac{\Delta G^\mathrm{DC}}{RT}\right). \tag{3.2.15}$$

The first term on the right-hand side can be identified with the bulk concentration of the guest molecule such that the equation has the form of the Henry isotherm. If we assume that each cyclodextrin can only accommodate one guest molecule and relate the amount adsorbed to the inner pore surface we obtain the Langmuir form [67]

$$q_\mathrm{ads} = q_\mathrm{max} \frac{K \cdot C}{1 + K \cdot C} \tag{3.2.16}$$

where q_max denotes the cyclodextrin density inside the pore and

$$K = \frac{1}{C^0} \exp\left(-\frac{\Delta G}{RT}\right) \tag{3.2.17}$$

with C^0 as the concentration of the standard state, i.e. $1\,\mathrm{mol\,l^{-1}}$ and ΔG as the standard binding free enthalpy obtained via double decoupling, direct counting or any other suitable computational or experimental approach. In that way, a Langmuir isotherm can be computed and compared to isotherms obtained from experiments or molecular simulation to assess whether other processes such as binding of multiple guest molecules to one cyclodextrin or cooperative effects of cyclodextrin molecules in close vicinity on the surface are likely to occur.

3.3. Results and Discussion

3.3.1. Bulk phase simulations

In order to verify the quality of the force field for the solute molecules *p*-nitrophenol and benzene, validating simulations were carried out based on topologies provided by Mobley et al. [54] resulting in liquid density values in good agreement with experiment, see table 3.3.1. Hydration free enthalpies ΔG_{hyd} reported by the Mobley group [68] were reproduced by decoupling simulations of these molecules in water, which in turn are in fair (*p*-nitrophenol) or good (benzene) agreement with the experimental values.

Table 3.3.1.: Liquid densities ρ (kg m^{-3}) for *p*-nitrophenol (*p*-NP) and benzene (BEN) compared with experimental data [69]. Hydration free enthalpy ΔG_{hyd} (kJ mol^{-1}) at 298 K was calculated via simulation (sim) and compared to simulation values reported by the Mobley group [68] (mo) and experimental values (exp) from Cabani et al. [70].

	ρ^{sim}	ρ^{exp}	$\Delta G_{\text{hyd}}^{\text{sim}}$	$\Delta G_{\text{hyd}}^{\text{mo}}$	$\Delta G_{\text{hyd}}^{\text{exp}}$
p-NP	1274.75[a]	1283.15[a]	−35.35	−35.44	−44.08
BEN	861.24[b]	873.49[b]	−3.23	−3.39	−3.62

[a]Determined at 387 K and [b]298 K.

Table 3.3.2 shows the binding free enthalpies and rate constants of CD+*p*-nitrophenol and CD+benzene complexes. For the long unbiased simulations first, a spatial cutoff had to be defined in order to differentiate between bound and unbound states. Since β-Cyclodextrin has a radius of gyration around 0.6 nm [71], the spatial cutoff distance was chosen at 0.7 nm to account for binding on the inner edge of the host molecule. This assumption is further strengthened by figure 3.3.1 where the histogram maximum of the center of mass distances between host and guest molecules diminishes at the chosen cutoff and a smaller cluster emerges that indicates the unbound states. The effect of the temporal cut-off between 0 and 1 ns on the binding free enthalpy is summarized in table S1 in the supplementary material. The consideration behind the temporal cut-off is that the average residence time of the guest molecule inside the host is usually shorter than an average experimentally determined survival time because in an experiment several short-term events are likely to be missed. This effect has to be kept in mind when comparing to experimentally determined rates which may differ depending on the temporal resolution of the measurement device. For benzene the effect on ΔG is minor, while for *p*-nitrophenol an effect is only visible between temporal cut-offs of 0 ps and 100 ps. For both molecules the k_{on}- and k_{off}-rates calculated with 0 ps cut-off are an order of magnitude larger compared to the values calculated with a larger cut-off. In the present work only bound/unbound periods that lasted longer than 1 ns were counted as one bound/unbound event, in agreement with previous works [34, 72].
For CD+benzene all three approaches used to calculate the binding free enthalpy yield a consistent value at both temperatures. For CD+*p*-nitrophenol the counting approaches did not provide reliable values at 298 K due to the rather strong binding and thus low occurrences of unbound instances. The time evolution of bound and unbound instances are provided in the supplementary material in figure S1. Therefore only the double decoupling results are reported at this temperature. At 350 K unbound occurrences are more likely due to the higher temperature, allowing an improved sampling which leads to results for the direct counting approach that is in good agreement with the double decoupling method. Nevertheless, the drop of the

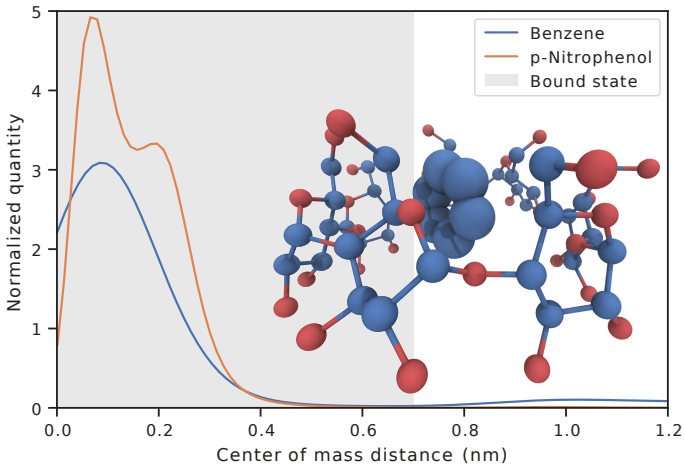

Figure 3.3.1.: Histogram of the central distances **C-C** with a marked area of the bound states (grey) of the reference systems for host and guest molecules as illustrated in figure 3.2.1 for benzene (blue) and *p*-nitrophenol (orange) at $T = 350\,\mathrm{K}$ with the corresponding image showing benzene in the bound state.

binding free enthalpy in the rate constants approach indicates that longer unbound instances are still infrequent. The reason for the larger binding free enthalpy at a higher temperature for benzene in the unbiased approaches is due to a larger volumetric correction in equation (3.2.1) at $RT_{298} \ln \frac{V_{\mathrm{box}}}{V^0} = 7.28\,\mathrm{kJ\,mol^{-1}}$ and, $RT_{350} \ln \frac{V_{\mathrm{box}}}{V^0} = 8.69\,\mathrm{kJ\,mol^{-1}}$, which is not entirely compensated by the decrease of the ratio of bound and unbound instances $RT_{298} \ln \frac{N_{\mathrm{b}}}{N_{\mathrm{u}}} = 5.98\,\mathrm{kJ\,mol^{-1}}$ and, $RT_{350} \ln \frac{N_{\mathrm{b}}}{N_{\mathrm{u}}} = 5.41\,\mathrm{kJ\,mol^{-1}}$, as they stay almost similar.

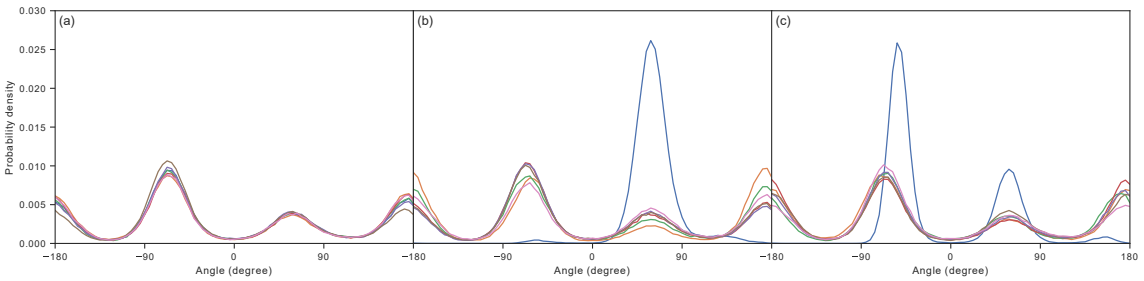

Figure 3.3.2.: (a) Distributions of the seven individual dihedral angles H6O-O6-C6-H61 for the native β-cyclodextrin resulting from an NpT simulation in TIP3P water. The different colours denote the different glucopyranose units. (b) Distribution of six dihedral angles H6O-O6-C6-H61 for β-cyclodextrin connected with the L1 linker [17]. The blue line represents the distribution of the C5(tail)-O6-C6-H61 dihedral angle. (c) Analogous to (b) but for the L2 linker [20] with the blue line representing the distribution of the C4(tail)-O6-C6-H61 dihedral angle.

For assessing the properties of the parametrized CD molecule with an attached linker for connecting to the pore surface, NpT simulations in TIP3P water were carried out and the resulting dihedral-angle distributions were analyzed. Figure 3.3.2(a) shows that for the native cyclodextrin the distributions are in good agreement with those reported by Gebhardt et al. [53] using the same force field. Additional dihedral-angle distributions for α- and γ-cyclodextrin are

Table 3.3.2.: Comparison of direct counting (DC), rate constants (RC) and double decoupling (DD) methods for determining the binding free enthalpy ΔG (kJ mol^{-1}) with experimental (Exp) data of β-cyclodextrin-ligand complexes, with association k_{on} (10^8 dm^3 mol^{-1} s^{-1}) and dissociation k_{off} (10^6 s^{-1}) rates at a temporal cut-off of 1 ns calculated at temperature T (K). The chosen spatial cut-off for differentiating between bound and unbound states is 0.7 nm for both guest molecules *p*-nitrophenol (*p*-NP) and benzene (BEN).

T	298			350		
	$-\Delta G$	k_{on}	k_{off}	$-\Delta G$	k_{on}	k_{off}
p-NP						
DC				24.22		
RC				17.01	11.6	3.34
DD	25.79			24.07		
Mean[a]				24.15		
Exp[73, 74]	10–17					
BEN						
DC	13.25			14.11		
RC	13.27	5.41	2.55	13.46	8.58	8.41
DD	13.12			12.15		
Mean[b]	13.21			13.24		
Exp[75]	12–13					

[a]Mean value from DC, DD, and [b]DC, RC, DD.

shown in the supplementary material in figure S3. Attaching the linker affects the corresponding dihedral angle describing rotation around the C6-O6 bond, see figure 3. With the L1-variant essentially one rotamer around 60° is populated (figure 3.3.2(b)) while the L2-variant has two rotamers populated (figure 3.3.2(c)).

3.3.2. Unfunctionalized silica pores

Figure 3.3.3 shows density profiles of water, benzene, and *p*-nitrophenol as well as axial diffusion coefficient profiles in a system containing 60 solute molecules which corresponds to a concentration of 200 mmol l^{-1}. Hardly any adsorption for benzene or *p*-nitrophenol is visible, in agreement with experiments [17, 20]. The number densities converges rapidly towards the density value at the pore center. The slowdown of water diffusion in confinement relative to the bulk phase can be compared with recent experimental data reported by Jani et al. [76]. At a temperature of 300 K the experimental self-diffusion coefficient of water in the bulk phase, 2.3×10^{-9} m^2 s^{-1}, is reduced to 2.0×10^{-9} m^2 s^{-1} in SBA-15 with a pore mean pore diameter of 6.6 nm and to 1.7×10^{-9} m^2 s^{-1} in MCM-41 with a pore diameter of 3.8 nm, close to the simulated pore diameter of 4 nm. This accounts to change of factor 1.15 for the SBA-15 system and 1.35 in the MCM-41 pore. The mean diffusion $\langle D_{\parallel} \rangle$ of water in the simulated unfunctionalized pore is 3.07×10^{-9} m^2 s^{-1} at a temperature of 298 K and 5.63×10^{-9} m^2 s^{-1} at a higher temperature of 350 K. This yields a factor 1.70 at 298 K and 1.74 at 350 K by comparing the pore diffusion to the bulk diffusion of the same system.

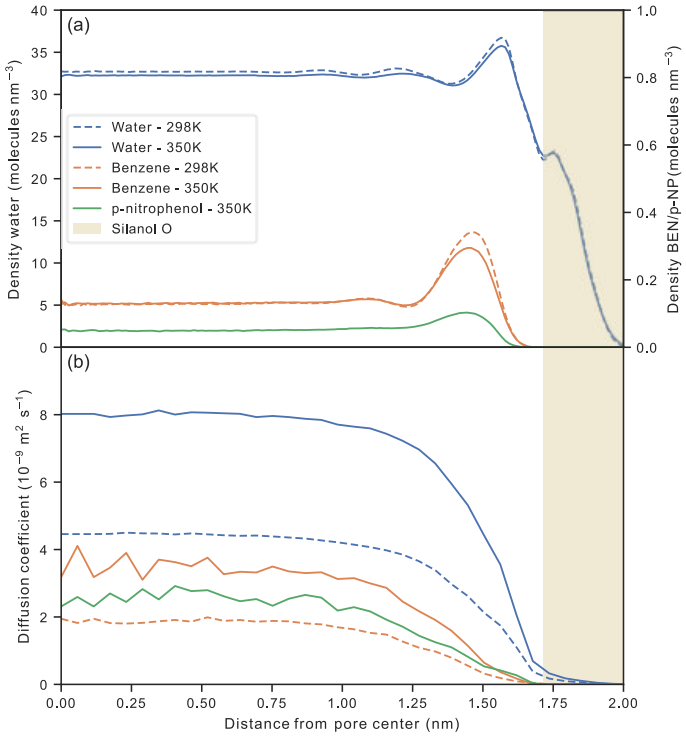

Figure 3.3.3.: (a) Density and (b) axial diffusion profiles of water (blue), benzene (BEN) (orange), and *p*-nitrophenol (p-NP) (green) in a non-functionalized pore at temperatures 298 K (dashed lines) and 350 K (solid lines). The shaded area denotes the configurational space of the silanol group oxygen atoms (yellow).

3.3.3. Cyclodextrin-functionalized silica pores

By functionalizing the surface, benzene molecules have a significantly higher concentration at the configurational space of the cyclodextrin center of mass, indicating host-guest interaction, see figure 3.3.4.

Benzene adsorption isotherms were calculated for a low cyclodextrin surface concentration at 298 K and a high cyclodextrin concentration at 298 K and 350 K. For *p*-nitrophenol only the larger surface concentration at 350 K was considered due to the strong binding affinity that leads to unreliable statistics at the lower temperature. The volumetric and the surface concentration of the guest molecules were assessed. The volumetric concentration in the reservoir was converted from the average number of molecules, which was determined by counting the solute molecule occurrences inside the reservoir normalized by the number of frames. Similarly, a surface specific concentration was determined by counting the appearances of the solute molecules inside the pore. In order to obtain excess adsorption, the adsorption value of the solute molecules within a non-functionalized pore has been subtracted. Repeating the pore simulation for different solute concentrations in the system, results into adsorption isotherms shown in figure 3.3.5. Further isotherms are provided in figure S4 of the supplementary material.

Similar to experimental observation a simple relation between the amount adsorbed and the number of cyclodextrin molecules attached to the surface could only be observed at small concentration, following Langmuir behavior. For benzene, Trofymchuk et al. [20] reported adsorption isotherms for materials with different amounts of cyclodextrin molecules up to benzene

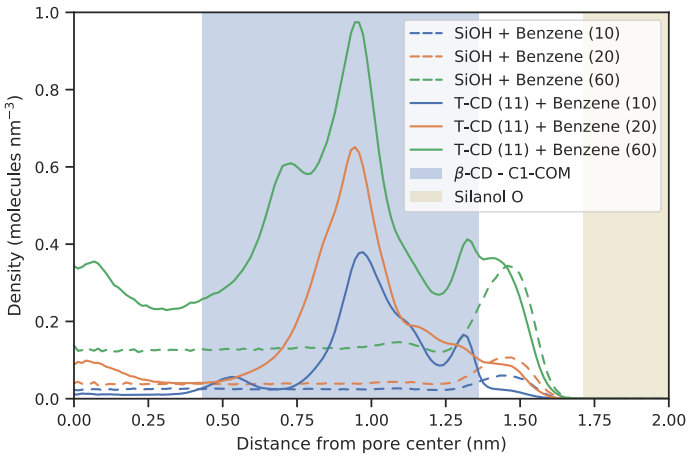

Figure 3.3.4.: Radial density profile of the benzene centre of mass in a non-functionalized pore (dashed lines) and in a functionalized pore using the L2-variant cyclodextrin (L2-CD) [20] (solid lines) simulated for 1 µs. Shaded areas denote the configurational space of the cyclodextrin centre of mass (blue) and the silanol groups oxygen atoms (yellow).

concentrations of 7 mmoll^{-1}, i.e., roughly one third of the solubility limit of 23.8 mmoll^{-1} at 25°C [77]. The corresponding amount adsorbed exceeded the capacity of a 1:1 binding by more than a factor of 10 and the isotherms showed dual-site Langmuir type behavior. In the present work higher benzene concentrations of up to 60 mmoll^{-1} were used to improve the statistical sampling. However, the amount adsorbed did not exceed the 1:1 binding capacity by more than a factor of two. The visual inspection of the trajectories shows that for the lower cyclodextrin density (i.e. five molecules attached to the pore surface) up to three benzene molecules may be associated to one cyclodextrin molecule. For the higher cyclodextrin density some cyclodextrin molecules may also be trapped in the space between the pore surface and the outer surface of the cyclodextrin, thus enhancing the adsorption capacity. Moreover, cyclodextrin molecules in close vicinity may associate and form rather long-living complexes that encapsulate the solute molecules. In addition, a benzene molecule dissociating from one cyclodextrin is very likely associating with the next one close by instead of leaving the pore.

For *p*-nitrophenol experimental adsorption isotherms were reported by Achad et al. for very low bulk concentrations below 0.15 mM, compared to the aqueous solubility of 115 mM at 25°C [78]. In this regime Langmuir behavior was observed with the Langmuir constant resembling the 1:1 association free enthalpy, as expected [18]. Shen et al. performed adsorption measurements at higher initial concentration of up to 28 mM *p*-nitrophenol and found adsorption capacities significantly larger than those corresponding to a 1:1 binding scenario and explained this finding with hydrogen bonds that are formed between the polar groups of *p*-nitrophenol and the hydroxyl groups of cyclodextrin and the amine groups of the functionalized silica, respectively [79]. In the simulations, a large range of bulk-phase concentration has been studied. The binding free enthalpy for the 1:1 complex is overestimated by the force field, leading to rather strong increase in the amount adsorbed at low bulk phase concentration that first follows the Langmuir isotherm but exceeds the 1:1 binding capacity by more than a factor of three due to the association of up to three nitrophenol molecules with one cyclodextrin molecule, the trapping between cyclodextrin and the pore surface and the formation of hydrogen bonds between the hydroxyl groups at the rims of cyclodextrin and *p*-nitrophenol in the solvent phase.

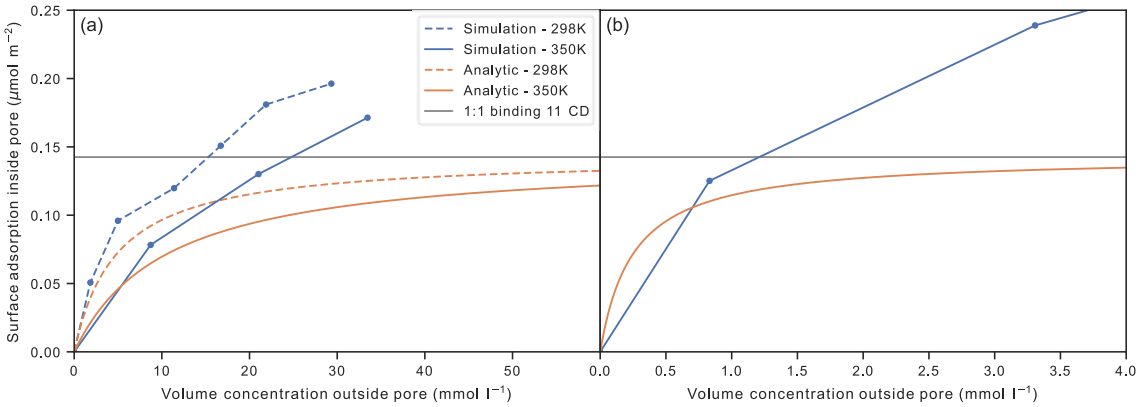

Figure 3.3.5.: (a) Excess adsorption isotherms of pore simulations utilizing an L2-variant [20] cyclodextrin functionalized surface (blue) compared to the analytical solution shown in equation (3.2.16) (orange) at varying amounts of benzene. The binding free enthalpy used to evaluate equation (3.2.16) was calculated as the mean value of all utilized methods (DC, RC, DD) at the respective temperature. (b) Like (a) but with an L1-variant cyclodextrin [17] with p-nitrophenol and the mean free enthalpy value only from the DD and DC approach. Simulation were run for 1 µs at 298 K (dashed lines) and 350 K (solid lines). The grey line represents a hypothetical maximum of 1:1 binding with 11 cyclodextrin molecules.

3.4. Conclusion and Outlook

An efficient model building is a prerequisite for computational studies of functionalized mesoporous silica materials. The Python package PoreMS introduced previously [42, 43] was complemented by two additional program packages for preparing MD simulations of porous materials with GROMACS, PoreSim [45], and for analyzing the simulation trajectories, PoreAna [66], the latter providing results such as density and diffusion profiles, thereby reducing the overhead for system preparation to analysis. The selected case study of adsorption of aromatic molecules in cyclodextrin-functionalized silica mesopores shows that current moderate computational resources allow an atomistically resolved model (~ 65 000 atoms) to be propagated to the µs time scale. The calculated adsorption isotherms show a more complex behavior than predicted by a simple Langmuir model corresponding to a 1:1 host:guest binding complex. Beside the formation of 1:2 and even 1:3 host:guest complexes also host-host interactions on the surface as well as more unspecific host-guest interactions have an influence on the shape of the isotherm. The information is relevant, for example, for the prediction of band broadening in liquid chromatography [80]. While the aim of the present work was to investigate the feasibility of calculating liquid phase adsorption isotherms by all-atom MD, future work may address the study of multicomponent mixtures, the influence of the solvent or the investigation of chiral stationary phases, e.g by attaching cyclodextrin derivatives.

References

[1] R. Sawicki and L. Mercier. “Evaluation of Mesoporous Cyclodextrin-Silica Nanocomposites for the Removal of Pesticides from Aqueous Media”. In: *Environ. Sci. Technol.* 40.6 (2006), pp. 1978–1983. DOI: 10.1021/es051441r.

[2] B. Tian et al. “Cyclodextrin-based adsorbents for the removal of pollutants from wastewater: a review”. In: *Environ. Sci. Pollut. R.* 28.2 (2021), pp. 1317–1340. DOI: 10.1007/s11356-020-11168-2.

[3] H. Lorenz and A. Seidel-Morgenstern. “Processes To Separate Enantiomers”. In: *Angew. Chem. Int. Ed.* 53.5 (2014), pp. 1218–1250. DOI: 10.1002/anie.201302823.

[4] R. Breslow and S. D. Dong. “Biomimetic Reactions Catalyzed by Cyclodextrins and Their Derivatives”. In: *Chem. Rev.* 98.5 (1998), pp. 1997–2012. DOI: 10.1021/cr970011j.

[5] S. Hu et al. “Asymmetric Supramolecular Primary Amine Catalysis in Aqueous Buffer: connections of Selective Recognition and Asymmetric Catalysis”. In: *J. Am. Chem. Soc.* 132.20 (2010), pp. 7216–7228. DOI: 10.1021/ja102819g.

[6] M. P. van der Helm, B. Klemm, and R. Eelkema. “Organocatalysis in aqueous media”. In: *Nat. Rev. Chem.* 3.8 (2019), pp. 491–508. DOI: 10.1038/s41570-019-0116-0.

[7] M. De Rosa et al. “Supramolecular Organocatalysis in Water Mediated by Macrocyclic Compounds”. In: *Front. Chem.* 6 (2018), p. 84. DOI: 10.3389/fchem.2018.00084.

[8] P. Rai et al. “β-Cyclodextrin: a Biomimetic Catalyst used for the Synthesis of 4H-chromene-3-carbonitrile and Tetrahydro-1H-xanthen-1-one Derivatives”. In: *Catal. Lett.* 145.12 (2015), pp. 2020–2028. DOI: 10.1007/s10562-015-1588-2.

[9] Á. Molnár. “Synthetic Application of Cyclodextrins in Combination with Metal Ions, Complexes, and Metal Particles”. In: *ChemCatChem* 13.6 (2021), pp. 1424–1474. DOI: 10.1002/cctc.202001610.

[10] C. Gaeta et al. “Supramolecular Catalysis with Self-Assembled Capsules and Cages: what Happens in Confined Spaces”. In: *ChemCatChem* 13.7 (2021), pp. 1638–1658. DOI: 10.1002/cctc.202001570.

[11] E. Del Valle. “Cyclodextrins and their uses: a review”. In: *Process Biochem.* 39.9 (2004), pp. 1033–1046. DOI: 10.1016/S0032-9592(03)00258-9.

[12] B. V. K. J. Schmidt and C. Barner-Kowollik. “Dynamic Macromolecular Material Design-The Versatility of Cyclodextrin-Based Host-Guest Chemistry”. In: *Angew. Chem. Int. Ed.* 56.29 (2017), pp. 8350–8369. DOI: 10.1002/anie.201612150.

[13] G. Gattuso, S. A. Nepogodiev, and J. F. Stoddart. “Synthetic Cyclic Oligosaccharides”. In: *Chem. Rev.* 98.5 (1998), pp. 1919–1958. DOI: 10.1021/cr960133w.

[14] A. R. Khan et al. “Methods for Selective Modifications of Cyclodextrins”. In: *Chem. Rev.* 98.5 (1998), pp. 1977–1996. DOI: 10.1021/cr970012b.

[15] A. Harada, J. Li, and M. Kamachi. “Synthesis of a tubular polymer from threaded cyclodextrins”. In: *Nature* 364.6437 (1993), pp. 516–518. DOI: 10.1038/364516a0.

[16] I. Ciucanu and W. A. König. “Immobilization of peralkylated β-cyclodextrin on silica gel for high-performance liquid chromatography”. In: *J. Chromatogr. A* 685.1 (1994), pp. 166–171. DOI: 10.1016/0021-9673(94)00564-8.

[17] R. Huq, L. Mercier, and P. J. Kooyman. “Incorporation of Cyclodextrin into Mesostructured Silica”. In: *Chem. Mater.* 13.12 (2001), pp. 4512–4519. DOI: 10.1021/cm010171i.

[18] A. Bibby and L. Mercier. “Adsorption and separation of water-soluble aromatic molecules by cyclodextrin-functionalized mesoporous silica”. In: *Green Chem.* 5 (2003), pp. 15–19. DOI: 10.1039/B209251B.

[19] N. V. Roik et al. “Mesoporous silicas with covalently immobilized β-cyclodextrin moieties: synthesis, structure, and sorption properties”. In: *J. Nanopart. Res.* 19.9 (2017), p. 317. DOI: 10.1007/s11051-017-3999-z.

[20] I. Trofymchuk, N. Roik, and L. Belyakova. “Structural Variety and Adsorptive Properties of Mesoporous Silicas with Immobilized Oligosaccharide Groups”. In: *Nanoscale Res. Lett.* 12.1 (2017), p. 307. DOI: 10.1186/s11671-017-2072-2.

[21] R. I. Derrah and D. M. Ruthven. “Sorption of the Inert Gases (Ar, Kr, and Xe) in Type A Zeolites”. In: *Can. J. Chem.* 53.7 (1975), pp. 996–1006. DOI: 10.1139/v75-142.

[22] B. Smit and T. L. M. Maesen. “Molecular Simulations of Zeolites: adsorption, Diffusion, and Shape Selectivity”. In: *Chem. Rev.* 108.10 (2008), pp. 4125–4184. DOI: 10.1021/cr8002642.

[23] A. Dabrowski. “Adsorption - from theory to practice”. In: *Adv. Colloid. Interface Sci.* 93.1-3 (2001), pp. 135–224. DOI: 10.1016/S0001-8686(00)00082-8.

[24] B. C. Bukowski et al. “Connecting theory and simulation with experiment for the study of diffusion in nanoporous solids”. In: *Adsorption* 27 (2021), pp. 683–760. DOI: 10.1007/s10450-021-00314-y.

[25] R. K. Lindsey et al. “Molecular simulation studies of reversed-phase liquid chromatography”. In: *J. Chromatogr. A* 1287 (2013), pp. 60–82. DOI: 10.1016/j.chroma.2013.02.040.

[26] S. M. Melnikov et al. “A Molecular Dynamics Study on the Partitioning Mechanism in Hydrophilic Interaction Chromatography”. In: *Angew. Chem. Int. Ed.* 51.25 (2012), pp. 6251–6254. DOI: 10.1002/anie.201201096.

[27] J. Rybka, A. Höltzel, and U. Tallarek. “Surface Diffusion of Aromatic Hydrocarbon Analytes in Reversed-Phase Liquid Chromatography”. In: *J. Phys. Chem. C* 121.33 (2017), pp. 17907–17920. DOI: 10.1021/acs.jpcc.7b04746.

[28] K. El Hage, R. J. Bemish, and M. Meuwly. “From in silica to in silico: retention thermodynamics at solid-liquid interfaces”. In: *Phys. Chem. Chem. Phys.* 20.27 (2018), pp. 18610–18622. DOI: 10.1039/C8CP02899K.

[29] N. Trebel et al. “Consequences of Cylindrical Pore Geometry for Interfacial Phenomena in Reversed-Phase Liquid Chromatography”. In: *J. Phys. Chem. B* 125.40 (2021), pp. 11320–11336. DOI: 10.1021/acs.jpcb.1c06732.

[30] J. E. Basconi, G. Carta, and M. R. Shirts. “Effects of protein properties on adsorption and transport in polymer-grafted ion exchangers: A multiscale modeling study”. In: *AIChE J.* 63 (2017), pp. 4564–4575. DOI: 10.1002/aic.15798.

[31] S. Jakobtorweihen, J. Heuer, and T. Waluga. “A novel approach to calculate adsorption isotherms by molecular dynamics simulations”. In: *J. Chromatogr. A* 1620 (2020), p. 460940. DOI: 10.1016/j.chroma.2020.460940.

[32] I. Nezbeda and J. Škvára. “On industrial applications of molecular simulations”. In: *Mol. Simul.* 47 (2020), pp. 846–856. DOI: 10.1080/08927022.2020.1828584.

[33] F. Gritti. “Perspective on the Future Approaches to Predict Retention in Liquid Chromatography”. In: *Anal. Chem.* 93 (2021), pp. 5653–5664. DOI: 10.1021/acs.analchem.0c05078.

[34] J. Baz et al. “Insights into Noncovalent Binding Obtained from Molecular Dynamics Simulations”. In: *Chem. Ing. Tech.* 90.11 (2018), pp. 1864–1875. DOI: 10.1002/cite.201800050.

[35] M. Gilson et al. “The statistical-thermodynamic basis for computation of binding affinities: a critical review”. In: *Biophys. J.* 72.3 (1997), pp. 1047–1069. DOI: 10.1016/S0006-3495(97)78756-3.

[36] W. F. van Gunsteren and H. J. C. Berendsen. “Thermodynamic cycle integration by computer simulation as a tool for obtaining free energy differences in molecular chemistry”. In: *J. Comput. Aid. Mol. Des.* 1.2 (1987), pp. 171–176. DOI: 10.1007/BF01676960.

[37] M. L. Mugnai and R. Elber. “Thermodynamic Cycle without Turning Off Self-Interactions: formal Discussion and a Numerical Example”. In: *J. Chem. Theory Comput.* 8.9 (2012), pp. 3022–3033. DOI: 10.1021/ct3003817.

[38] S. Boresch et al. “Absolute Binding Free Energies: a Quantitative Approach for Their Calculation”. In: *J. Phys. Chem. B* 107.35 (2003), pp. 9535–9551. DOI: 10.1021/jp0217839.

[39] D. L. Mobley, J. D. Chodera, and K. A. Dill. “On the use of orientational restraints and symmetry corrections in alchemical free energy calculations”. In: *J. Chem. Phys.* 125.8 (2006), p. 084902. DOI: 10.1063/1.2221683.

[40] C. Cézard et al. “Molecular dynamics studies of native and substituted cyclodextrins in different media: 1. charge derivation and force field performances”. In: *Phys. Chem. Chem. Phys.* 13.33 (2011), p. 15103. DOI: 10.1039/c1cp20854c.

[41] D. A. Case et al. *AMBER 2020*. 2020.

[42] H. Kraus et al. “PoreMS: a software tool for generating silica pore models with user-defined surface functionalisation and pore dimensions”. In: *Mol. Simul.* 47.4 (2021), pp. 306–316. DOI: 10.1080/08927022.2020.1871478.

[43] H. Kraus and N. Hansen. *PoreMS: 0.2.2*. Version v0.2.2. 2021. DOI: 10.5281/zenodo.4738036.

[44] T. S. Gulmen and W. H. Thompson. “Testing a Two-State Model of Nanoconfined Liquids: conformational Equilibrium of Ethylene Glycol in Amorphous Silica Pores”. In: *Langmuir* 22.26 (2006), pp. 10919–10923. DOI: 10.1021/la062285k.

[45] H. Kraus. *PoreSim: 0.1.0*. Version v0.1.0. 2021. DOI: 10.5281/zenodo.4588861.

[46] M. J. Abraham et al. “GROMACS: high performance molecular simulations through multi-level parallelism from laptops to supercomputers”. In: *SoftwareX* 1-2 (2015), pp. 19–25. DOI: 10.1016/j.softx.2015.06.001.

[47] B. Hess et al. “GROMACS 4: algorithms for Highly Efficient, Load-Balanced, and Scalable Molecular Simulation”. In: *J. Chem. Theory. Comput.* 4.3 (2008), pp. 435–447. DOI: 10.1021/ct700301q.

[48] M. Bonomi et al. “PLUMED: a portable plugin for free-energy calculations with molecular dynamics”. In: *Comput. Phys. Commun.* 180.10 (2009), pp. 1961–1972. DOI: 10.1016/j.cpc.2009.05.011.

[49] G. A. Tribello et al. “PLUMED 2: new feathers for an old bird”. In: *Comput. Phys. Commun.* 185.2 (2014), pp. 604–613. DOI: 10.1016/j.cpc.2013.09.018.

[50] F. Ziegler et al. “Olefin Metathesis in Confined Geometries: a Biomimetic Approach toward Selective Macrocyclization”. In: *J. Am. Chem. Soc.* 141.48 (2019), pp. 19014–19022. DOI: 10.1021/jacs.9b08776.

[51] F. Ziegler et al. “Confinement Effects for Efficient Macrocyclization Reactions with Supported Cationic Molybdenum Imido Alkylidene N-Heterocyclic Carbene Complexes”. In: *ACS Catal.* 11 (2021), pp. 11570–11578. DOI: 10.1021/acscatal.1c03057.

[52] J. Wang et al. “Development and testing of a general amber force field”. In: *J. Comput. Chem.* 25.9 (2004), pp. 1157–1174. DOI: 10.1002/jcc.20035.

[53] J. Gebhardt et al. “Validation and Comparison of Force Fields for Native Cyclodextrins in Aqueous Solution”. In: *J. Phys. Chem. B* 122.5 (2018), pp. 1608–1626. DOI: 10.1021/acs.jpcb.7b11808.

[54] D. L. Mobley et al. *MobleyLab/FreeSolv: Version 0.52*. Version v0.52. 2018. DOI: 10.5281/zenodo.1161245.

[55] W. L. Jorgensen et al. “Comparison of simple potential functions for simulating liquid water”. In: *J. Chem. Phys.* 79.2 (1983), pp. 926–935. DOI: 10.1063/1.445869.

[56] J. Dix, L. Lue, and P. Carbone. “Why different water models predict different structures under 2D confinement”. In: *J. Comput. Chem.* 39.25 (2018), pp. 2051–2059. DOI: 10.1002/jcc.25369.

[57] S. Nosé. “A molecular dynamics method for simulations in the canonical ensemble”. In: *Mol. Phys.* 52.2 (1984), pp. 255–268. DOI: 10.1080/00268978400101201.

[58] W. G. Hoover. “Canonical dynamics: equilibrium phase-space distributions”. In: *Phys. Rev. A* 31.3 (1985), pp. 1695–1697. DOI: 10.1103/physreva.31.1695.

[59] M. Parrinello and A. Rahman. “Crystal Structure and Pair Potentials: a Molecular-Dynamics Study”. In: *Phys. Rev. Lett.* 45.14 (1980), pp. 1196–1199. DOI: 10.1103/physrevlett.45.1196.

[60] M. Parrinello and A. Rahman. “Polymorphic transitions in single crystals: a new molecular dynamics method”. In: *J. Appl. Phys.* 52.12 (1981), pp. 7182–7190. DOI: 10.1063/1.328693.

[61] B. Hess et al. “LINCS: a linear constraint solver for molecular simulations”. In: *J. Comp. Chem.* 18.12 (1997), pp. 1463–1472. DOI: 10.1002/(sici)1096-987x(199709)18:12<1463::aid-jcc4>3.0.co;2-h.

[62] B. Hess. “P-LINCS: a Parallel Linear Constraint Solver for Molecular Simulation”. In: *J. Chem. Theory Comput.* 4.1 (2008), pp. 116–122. DOI: 10.1021/ct700200b.

[63] T. Darden, D. York, and L. Pedersen. “Particle mesh Ewald: An N log(N) method for Ewald sums in large systems”. In: *J. Chem. Phys.* 98.12 (1993), pp. 10089–10092. DOI: 10.1063/1.464397.

[64] U. Essmann et al. “A smooth particle mesh Ewald method”. In: *J. Chem. Phys.* 103.19 (1995), pp. 8577–8593. DOI: 10.1063/1.470117.

[65] J. G. Kirkwood. “Statistical Mechanics of Fluid Mixtures”. In: *J. Chem. Phys.* 3.5 (1935), pp. 300–313. DOI: 10.1063/1.1749657.

[66] H. Kraus and N. Hansen. *PoreAna: 0.2.0*. Version v0.2.0. 2021. DOI: 10.5281/zenodo.4738182.

[67] I. Langmuir. “The Adsorption of Gases on Plane Surfaces of Glass, Mica and Platinum”. In: *J. Am. Chem. Soc.* 40.9 (1918), pp. 1361–1403. DOI: 10.1021/ja02242a004.

[68] G. Duarte Ramos Matos et al. “Approaches for Calculating Solvation Free Energies and Enthalpies Demonstrated with an Update of the FreeSolv Database”. In: *J. Chem. Eng. Data* 62.5 (2017), pp. 1559–1569. DOI: 10.1021/acs.jced.7b00104.

[69] *Dortmund Data Bank*. www.ddbst.com. 2014.

[70] S. Cabani et al. “Group contributions to the thermodynamic properties of non-ionic organic solutes in dilute aqueous solution”. In: *J. Solution Chem.* 10.8 (1981), pp. 563–595. DOI: 10.1007/BF00646936.

[71] S. K. S. Al-Burtomani and F. O. Suliman. “Inclusion complexes of norepinephrine with β-cyclodextrin, 18-crown-6 and cucurbit[7]uril: experimental and molecular dynamics study”. In: *RSC Adv.* 7.16 (2017), pp. 9888–9901. DOI: 10.1039/C6RA28638K.

[72] Z. Tang and C. A. Chang. “Binding Thermodynamics and Kinetics Calculations Using Chemical Host and Guest: A Comprehensive Picture of Molecular Recognition”. In: *J. Chem. Theory Comput.* 14.1 (2018), pp. 303–318. DOI: 10.1021/acs.jctc.7b00899.

[73] M. V. Rekharsky and Y. Inoue. “Complexation Thermodynamics of Cyclodextrins”. In: *Chem. Rev.* 98.5 (1998), pp. 1875–1918. DOI: 10.1021/cr970015o.

[74] F. Cramer, W. Saenger, and H. C. Spatz. “Inclusion Compounds. XIX.[1a] The Formation of Inclusion Compounds of α-Cyclodextrin in Aqueous Solutions. Thermodynamics and Kinetics”. In: *J. Am. Chem. Soc.* 89.1 (1967), pp. 14–20. DOI: 10.1021/ja00977a003.

[75] W. Chen, C.-E. Chang, and M. K. Gilson. “Calculation of Cyclodextrin Binding Affinities: energy, Entropy, and Implications for Drug Design”. In: *Biophys. J.* 87.5 (2004), pp. 3035–3049. DOI: 10.1529/biophysj.104.049494.

[76] A. Jani et al. “Dynamics of water confined in mesopores with variable surface interaction”. In: *J. Chem. Phys.* 154.9 (2021), p. 094505. DOI: 10.1063/5.0040705.

[77] F. P. Schwarz. “Measurement of the solubilities of slightly soluble organic liquids in water by elution chromatography”. In: *Anal. Chem.* 52.1 (1980), pp. 10–15. DOI: 10.1021/ac50051a004.

[78] C. Achard et al. “Aqueous Solubilities of Phenol Derivatives by Conductivity Measurements”. In: *J. Chem. Eng. Data* 41.3 (1996), pp. 504–507. DOI: 10.1021/je950202o.

[79] H.-M. Shen et al. “Surface immobilization of β-cyclodextrin on hybrid silica and its fast adsorption performance of p-nitrophenol from the aqueous phase”. In: *RSC Adv.* 5 (103 2015), pp. 84410–84422. DOI: 10.1039/C5RA15592D.

[80] B. L. Karger, L. R. Snyder, and C. Horvath. *An introduction to separation science*. New York: John Wiley & Sons, 1973.

4. Fluid structure and dynamics in mesoporous confinement

4.1. Introduction

In a porous catalyst particle, hindered diffusion to and from the active surface sites often becomes a limiting factor to the process performance [1]. With the advent in sophisticated synthesis methods, porous materials with controlled pore size distributions can be generated and used for catalyst immobilization [2, 3]. This raises the question which materials are the best ones to optimize catalyst performance by taking advantage of the confinement effect and its impact on catalyst selectivity [4–7]. Computational modeling is crucial to address this question and requires usually a multiscale modeling framework [8]. An important part of such a framework are molecular dynamics (MD) simulations at atomistic resolution, which provide important insight on the single pore level and can be used to inform more coarse-grained approaches on the mesoscale level [9]. In the present work the results from MD simulations of various confined systems are presented and their impact on macroscopically observed behavior is discussed.

4.2. Methodology

4.2.1. Generating functionalized silica pores

For the present study a variety of functionalized pore models were generated with the software tool PoreMS designed to facilitate rapid model building of functionalised silica pores for Monte Carlo or molecular dynamics simulation studies of confinement effects in applications relying on functionalised mesoporous silica [10, 11].
The aim of the first set of pore systems was analyzing the effect of surface composition on surface-substrate interactions. While experimentally the amount of silanol groups on the inner pore surface can be determined, the exact structure of the surface is not known in detail. For the computational model however, the positions of all atoms have to be specified as well as their interactions with the surrounding molecules. In order to resemble experimental conditions of a rather low surface hydroxylation degree of just $0.7\,\mu mol\,m^{-2}$ [12] and study the impact of the modeling approach on the resulting density profiles inside the pore, six cases were investigated: (i) Add a maximal possible number of siloxane bridges reaching a surface hydroxylation of $3\,\mu mol\,m^{-2}$ then deactivate silanol molecules by removing the hydrogen atomic partial charge until reaching the experimental surface hydroxylation as shown in figure 4.2.1 and table 4.2.1, (ii) like (i) but use the larger Lennard-Jones parameters from Coasne and Fourkas [13] compared to the ones proposed by Gulmen and Thompson [14] which were used in an earlier study [15], (iii) add siloxane bridges until reaching a surface hydroxylation of $5.3\,\mu mol\,m^{-2}$ which is the experimental value determined by Ide et al. [16], (iv) like (iii) but further deactivate silanol surface groups until reaching the surface hydroxylation from the accompanying experimental study [12], (v) only deactivate silanol molecules to achieve the desired final surface hydroxylation, and (vi) like (v) but with larger Lennard-Jones parameters from Coasne and

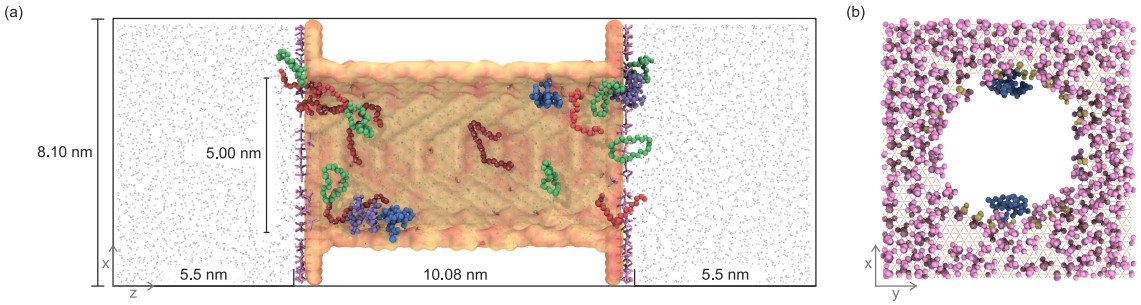

Figure 4.2.1.: Pore system functionalized with supported cationic molybdenum imido alkylidene N-heterocyclic carbene complexes (Mo1). (a) Side view of the simulation box filled with benzene (grey dots) indicating the length of the central silica block and the solvent reservoirs. (b) Front view of the pierced silica block containing the 5 nm diameter pore. The chemistry of the exterior surface is based on the (111) face of β-cristobalite silica. The hydroxylation degree was reduced by adding a maximal amount of siloxane bridges then further reduced by deactivating silanol groups to the experimental value determined by Ziegler et al. [12]. Further details are specified in Table 4.2.1. Colour code: Si, yellow surface O, red surface; substrate, red; product, green; benzene, grey dots; Mo1-cation, blue; $B(Ar^F)_4$-anion, purple; TMS surface groups, pink; surface silanol groups, yellow.

Fourkas [13]. All these systems were generated for a 5 nm and a 6.2 nm pore with 2 / 3 supported cationic molybdenum imido alkylidene N-heterocyclic carbene complexes (Mo1). The exterior surface was functionalized with a maximal possible amount of trimethylsilyl (TMS) groups after reducing the hydroxylation degree to 5.3 µmol m^{-2}. These pore structure were flanked with bulk reservoirs containing 12.5 mM of both substrate (dodecane-1,12-diyl bis(undec-10-enoate)) and product (Z-1,7-dioxacycloheptacos-17-ene-8,27-dione) from Ziegler et al. [15] and filled with benzene as solvent.

The second set of pores were utilized for analyzing the effect of geometrical confinement on mobility. Bare silica pores were utilized without further functionalization which is shown in table 4.2.2. The bulk reservoirs on both sides of the pore structure were filled with (i) different concentrations of benzene in water as shown in figure 4.2.2, and (ii) different concentrations of *p*-nitrophenol in water.

4.2.2. Molecular dynamics simulations

All simulations were run using GROMACS 2019.6 [17, 18] on the ForHLR II cluster. Similar to previous studies [12, 15], the general Amber force field (GAFF) was utilized [19] as the underlying force field. Because the NVT ensemble was used, the system was iteratively filled with molecules until reaching densities calculated from a prior NpT simulation.

The simulations were performed under periodic boundary conditions while using the Nosé-Hoover thermostat [20, 21] for temperature control with a coupling constant of 1 ps. Bond lengths between heavy atoms and hydrogens were constrained by the LINCS algorithm [22, 23] with an order of 4. Short-range electrostatic and Lennard-Jones parameters were evaluated up to a cutoff distance of 1.4 nm while including analytical dispersion corrections for energy and pressure. Long-range electrostatic interactions were treated with the particle-mesh Ewald algorithm [24, 25].

Table 4.2.1.: Properties of the generated cylindrical pores with Mo1-Catalysts, with surface densities (µmol m^{-2}) and pore dimensions (nm).

	5 nm		6 nm	
	Interior	Exterior	Interior	Exterior
Silica block xyz-dimensions	8.10; 7.89; 10.08		8.10; 7.89; 10.08	
Pore drilling direction	z		z	
Pore diameter	5.00		6.20	
Surface roughness[a]	0.09	0.00	0.09	0.00
Solvent reservoir z-dimension		5.50		5.00
Simulation box xyz-dimensions	8.10; 7.89; 20.08		8.10; 7.89; 20.08	
Pore volume	197.46		303.75	
Solvent reservoir volume		2×351.43		2×319.49
Surface area	158.11	2×44.30	196.11	2×33.75
Surface chemistry before func.				
Number of single silanol groups	258	242	294	176
Number of geminal silanol groups	15	21	31	20
Number of siloxane bridges	294	78	371	65
Total number of OH groups	288	284	356	216
Overall hydroxylation	3.02	5.32	3.01	5.31
Surface chemistry after func.				
Number of Mo1 groups	2	0	3	0
Mo1 density	0.02	0.00	0.03	0.00
Number of SLO (deactivated silanol)	220	0	203	0
SLO (deactivated silanol) density	2.31	0	1.71	0
Number of TMS groups	0	263	0	196
TMS density	0	4.93	0	4.82
Bonded-phase density	2.33	4.93	1.74	4.82
Number of residual OH groups	66	21	150	20
Residual hydroxylation	0.69	0.39	1.27	0.49

[a]Calculated as the standard deviation of the shortest distances between the central pore axis and the surface Si atoms.

4.2.3. Analysis

The density and diffusion within the pore systems were analyzed using the developed PoreAna [26] analysis suite. Radial density and diffusion profiles within the pore were determined by slicing the cylindrical volume into radial volume bins

$$V_i = \pi z (r_i^2 - r_{i-1}^2) \tag{4.2.1}$$

with pore length z and radius r_i of slice i. The number density ρ_i is determined by counting the number of molecules N_i within each bin during the whole trajectory

$$\rho_i = \frac{N_i}{V_i} = \frac{N_i}{\pi z} \frac{1}{r_i^2 - r_{i-1}^2}. \tag{4.2.2}$$

The axial diffusion coefficient $D_{\parallel,i}$ parallel to the pore surface was determined from the slope of the mean square displacement $\Delta_i(t)$ over an observation time of 4-20 ps within each bin with

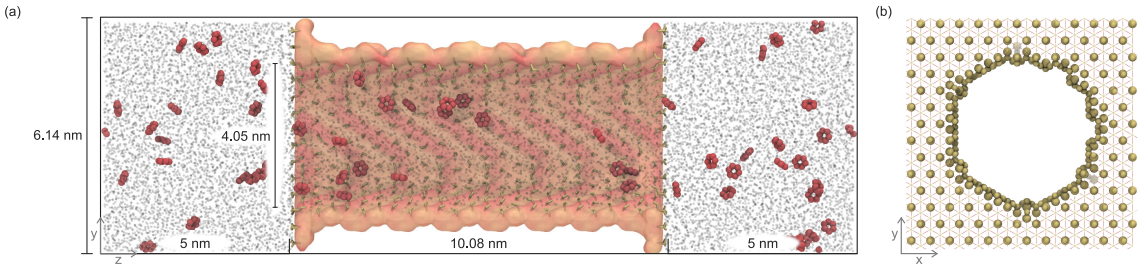

Figure 4.2.2.: Pore system without surface functionalization. (a) Side view of the simulation box filled with water (gray) and benzene (red) indicating the length of the central silica block and the solvent reservoirs. (b) Front view of the pierced silica block containing the 4 nm diameter pore. The chemistry of the exterior surface is based on the (111) face of β-cristobalite silica. Further details are specified in Table 4.2.2. Colour code: Si, yellow surface; O, red surface; water, gray; benzene, red; surface silanol groups, yellow.

a tolerance of ±1 bins

$$D_{\parallel,i} = \frac{1}{2}\frac{\mathrm{d}\Delta_i(t)}{\mathrm{d}t}. \tag{4.2.3}$$

By integrating the diffusion profile $D_{\parallel,i}$ with the density profile ρ_i along the radius r, a mean diffusion coefficient $\langle D_\parallel \rangle$ can be determined

$$\langle D_\parallel \rangle = \frac{\sum \rho_i D_{\parallel,i} A_i}{\sum \rho_i A_i} = \frac{\sum \rho_i D_{\parallel,i}(r_i^2 - r_{i-1}^2)}{\sum \rho_i (r_i^2 - r_{i-1}^2)} \tag{4.2.4}$$

with the surface of bin i

$$A_i = \pi(r_i^2 - r_{i-1}^2). \tag{4.2.5}$$

Alternatively, spatially resolved diffusion coefficients along the pore axis were calculated from a Bayesian analysis of the molecular dynamics trajectories as described by Hummer and coworkers [27, 28]. For this purpose the Smoluchowski diffusion equation [29, 30], describing the time evolution of the probability density $p(z,t)$ along the coordinate z

$$\frac{\partial p(z,t)}{\partial t} = \frac{\partial}{\partial z}\left\{ D(z) e^{-\beta F(z)} \frac{\partial}{\partial z}\left[e^{\beta F(z)} p(z,t) \right] \right\} \tag{4.2.6}$$

with $\beta^{-1} = k_\mathrm{B} T$, where k_B is Boltzmann's constant and T the absolute temperature is discretized, giving a system of rate equations. Analytical models of diffusion, $D(z)$, and free-energy, $F(z)$, profiles were then optimized using Monte Carlo sampling by comparing the observed motion along z with the motion expected from diffusive dynamics, resulting in a posterior density of unknown parameters of the diffusive model given the simulated trajectory.

4.3. Results

After an initial benchmark to determine the scaling of the simulation systems on the ForHLR II cluster as shown in figure 4.3.1, it was concluded that a core number of 400 (20 nodes, 20 cores each) is the most efficient with respect to efficiency and total simulation time, as it is the point at which speedup is significantly reduced due to increasing communication time between processors.

Table 4.2.2.: Properties of the non-functionalized cylindrical mesopore, with surface densities ($\mu mol\,m^{-2}$) and pore dimensions (nm).

	Interior	Exterior
Silica block xyz-dimensions	6.07; 6.14; 10.08	
Pore drilling direction	z	
Pore diameter	4.05	
Surface roughness[a]	0.08	0.00
Solvent reservoir z-dimension		5.00
Simulation box xyz-dimensions	6.07; 6.14; 20.08	
Pore volume	129.74	
Solvent reservoir volume		2×186.36
Surface area	128.16	2×24.39
Surface chemistry before func.		
Number of single silanol groups	553	205
Number of geminal silanol groups	68	27
Number of siloxane bridges	0	0
Total number of OH groups	689	259
Overall hydroxylation	8.93	8.82
Surface chemistry after func.		
Bonded-phase density	0.00	0.00
Number of residual OH groups	689	259
Residual hydroxylation	8.93	8.82

[a]Calculated as the standard deviation of the shortest distances between the central pore axis and the surface Si atoms.

All simulations were carried out for a total of 1 µs which resulted into around 150 000 core–h per simulation and thus a total of 3 000 000 core–h pure simulation time for the results presented here, omitting the time used for analysis. During the project, several studies were undertaken which in total consumed all the provided simulation time of 16 000 000 core–h. All simulation files for running the discussed systems are provided via DaRUS [31].

4.3.1. Influence of surface chemistry on density profiles

With the first set of simulations an understanding of the effect of surface composition on the solvent behavior was aimed for. The results of the previously discussed surface functionalisations are shown in figure 4.3.2.
Reducing the hydroxylation degree of the pore mainly by adding siloxane bridges, leads to some lattice atoms being strongly solvent exposed, because the underlying β-cristobalite silica only allows for siloxane bridges with rather unphysical bond lengths. As a consequence, the substrate and product molecules are penetrating into the lattice in an unphysical manner. Using the larger Lennard-Jones parameters suggested by Coasne and Fourkas [13] for the lattice atoms, does not remove this effect. Reducing the amount of siloxane bridges to the hydroxylation degree reported by Ide et al. [16] shows similar behavior. This concludes that the main issue is the exposure of the surface. In the final attempts, only deactivated silanol groups were used to reach the desired hydroxylation degree, i.e. no unphysical siloxane bridges were introduced. Here, it can be seen that the peak of oxygen density profile has a well-defined behavior.

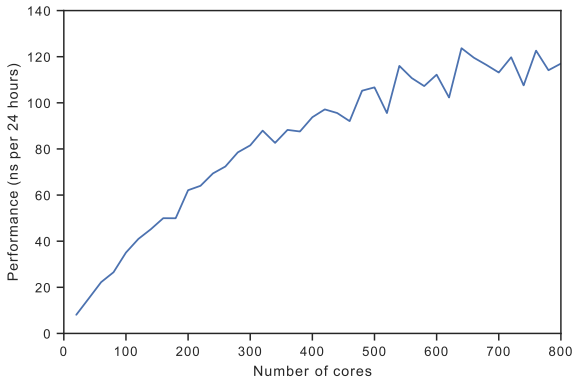

Figure 4.3.1.: Benchmark of the simulation time achieved per hour depending on the number of cores using GROMACS.

However, the mobility is still hindered as concluded from unrealistic residence times of surface-attached substrate and product molecules. Therefore, the larger Lennard-Jones parameters for the lattice atoms suggested by Coasne and Fourkas [13] were utilized. More detailed figures with substrate and product density profiles in the 5 nm and 6 nm pores are deposited on DaRUS [31].

4.3.2. Structure and mobility of aqueous mixtures in mesoporous confinement

For analyzing the quality of different methods for calculating diffusion in mesopores, simple unfunctionalized pores were simulated with water and different concentrations of benzene and *p*-nitrophenol. The first methodology calculates the diffusion coefficient as a function of the radius using a binning approach. This means that the volume is divided into sub-volumes in the shape of cylinder rings. The mean square displacement of the molecules center of mass is then calculated within each of these bins. If the center of mass leaves the bin, the trajectory is discarded within the observed time window. This creates the issue that a lot of data is discarded which can be counteracted by increasing the bin size and decreasing the observation time to the reduce the probability of the molecule leaving the bin. Another method of calculating the diffusion coefficient in pores uses a Monte Carlo (MC) algorithm developed by Hummer et al. [27]. The main difference is that instead of determining the mean square displacement within separate bins during short time intervals, the transition probability along the pore system is sampled. This so called transition matrix can then be used to calculate diffusion and free energy profiles as seen in figure 4.3.3 using the Smoluchowski equation (4.2.6).
Results from calculating the mean diffusion coefficients within the different sections of the pore system are shown in table 4.3.1. Here it can be seen that the diffusion coefficients within the reservoirs region calculated using the MC algorithm are in good agreement with the values calculated from a simple bulk-phase NpT simulation. However comparing the coefficients within the pore determined from the binning and MC approaches, show a larger discrepancy with the MC coefficients being larger. This can be attributed to the methodology of the binning approach. Since molecule trajectories leaving a bin are discarded, faster moving molecules have a much higher probability of being omitted resulting into an overall smaller diffusion coefficient.

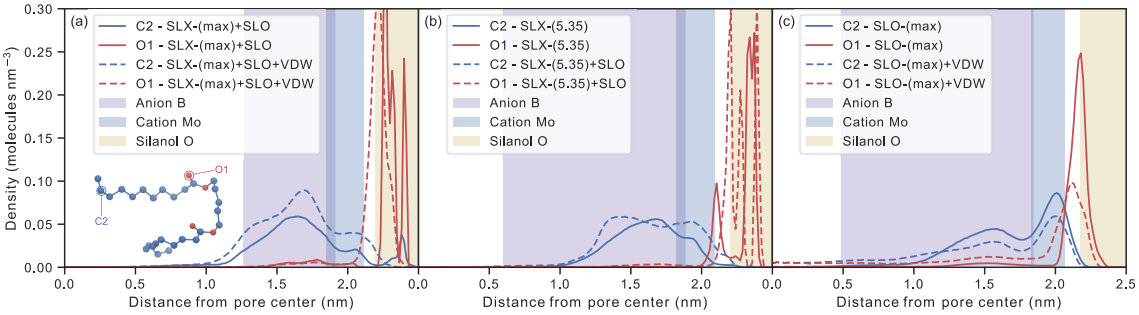

Figure 4.3.2.: Radial density profiles of the carbonyl oxygen O1 (red lines) and vinylic carbon C2 of the substrate (blue lines) in a 5 nm pore with two catalytic centers. The shaded areas indicate the configurational space accessible by the boron atom (purple) of the anion, the molybdenum atom (blue) of the cation and the silanol oxygen (yellow). (a) The surface was functionalized with the maximum amount of siloxane bridges (SLX) and the hydroxylation degree of 0.7 µmol m^{-2} was achieved by deactivating silanol surface groups (SLO) (solid lines). An additional surface was similarly prepared but with the addition of larger Van-der-Waals parameters (VDW) from Coasne and Fourkas [13] (dashed lines). (b) Siloxane bridges were only added until reaching the hydroxylation degree of 5.3 µmol m^{-2} reported by Ide et al. [16] (solid lines). In another pore the hydroxylation degree was reduced to 0.7 µmol m^{-2} by deactivating silanol groups (dashed lines). (c) Only silanol groups were deactivated in order to reach the hydroxylation degree of 0.7 µmol m^{-2} (solid lines) and the same functionalization was simulated with lager Van-der-Waals parameters (dashed lines).

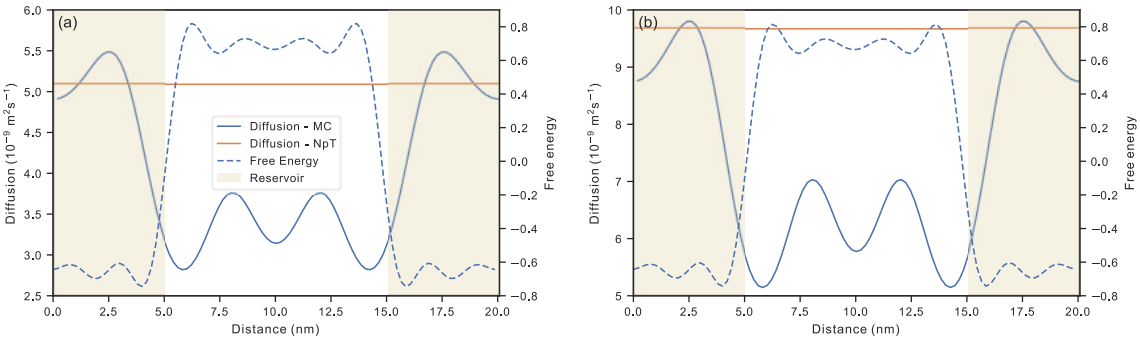

Figure 4.3.3.: Diffusion (solid lines) and free energy profiles (dashed lines) of water in the pore system calculated using the MC-Diffusion algorithm compared to the bulk diffusion (orange) from an NpT simulation at (a) T = 298 K and (b) T = 350 K. The yellow areas denote the region of the bulk reservoirs of the pore system.

Table 4.3.1.: Diffusion coefficient ($10^{-9}\,m^2\,s^{-1}$) of water from an NpT simulation D_{NpT}, in the bulk phase of the pore system D_{Bulk} and within the pore D_{Pore} calculated using the binning method (Bin) and the MC-method (MC) for benzene (BEN) and *p*-nitrophenol (*p*-NP) as solutes. The pore system contains a cylindrical pore of 4 nm with no surface functionalization. Properties are shown in table 4.2.2.

		298 K				350 K			
Solute	N_{Solute}	D_{NpT}	D_{Bulk}^{MC}	$\langle D\rangle_{Pore}^{Bin}$	D_{Pore}^{MC}	D_{NpT}	D_{Bulk}^{MC}	$\langle D\rangle_{Pore}^{Bin}$	D_{Pore}^{MC}
BEN	10	5.23	5.24	3.07	3.58	9.78	9.36	5.63	6.42
	60	5.09	5.08	2.93	3.38	9.21	9.05	5.47	6.27
p-Np	10	5.32	5.35	3.07	3.50	10.30	9.64	5.60	6.38
	60	5.11	5.20	3.05	3.47	9.56	9.10	5.54	6.33

4.4. Discussion

The strength of localized adsorption of substrate and product molecules onto the silanol groups of the silica surface via hydrogen bonding depends on the details of the computational model used to represent the surface. Since the exact density distribution is an experimentally elusive quantity a comparison between simulation and experiment has to be based on indirect indicators such as diffusion coefficients or residence times in a continuous flow setting [32]. Moreover, in future work parent materials other than β-cristobalite silica will be tested [33, 34] including representations of the usually amorphous silica surface as generated based on large-scale density functional theory calculations.

4.5. Conclusion

Recent developments in the synthesis of mesoporous solid materials have triggered an increased attention towards understanding their adsorption and diffusion properties for molecular heterogeneous catalysis in confined geometries. Molecular simulations based on atomistic force fields are an important component within an integrated multiscale simulation approach. While the development of more powerful computer resources increases the complexity of materials that can be simulated the development of experimental characterization and synthesis techniques are expected to provide templates for more realistic models in the future. Large scale density functional theory calculations are expected to help closing the gap between experimental resolution and atomistic force field models.

References

[1] B. C. Bukowski et al. “Connecting theory and simulation with experiment for the study of diffusion in nanoporous solids”. In: *Adsorption* 27.5 (2021), pp. 683–760. DOI: 10.1007/s10450-021-00314-y.

[2] T. Banerjee et al. “Polymer photocatalysts for solar-to-chemical energy conversion”. In: *Nat. Chem. Rev.* 6 (2021), pp. 168–190. DOI: 10.1038/s41578-020-00254-z.

[3] F. Markus et al. “Ordered Mesoporous Carbons via Self-Assembly of Tailored Block Copolyethers for Pore Size-Dependent Applications”. In: *ACS Appl. Nano Mater.* 4.4 (2021), pp. 3486–3492. DOI: https://doi.org/10.1021/acsanm.0c03467.

[4] F. Goettmann and C. Sanchez. “How does confinement affect the catalytic activity of mesoporous materials?” In: *J. Mater. Chem.* 17.1 (2007), pp. 24–30. DOI: 10.1039/B608748P.

[5] C. Yu and J. He. “Synergic catalytic effects in confined spaces”. In: *Chem. Commun.* 48.41 (2012), p. 4933. DOI: 10.1039/c2cc31585h.

[6] V. Mouarrawis et al. “Confinement Effects in Catalysis Using Well-Defined Materials and Cages”. In: *Front. Chem.* 6 (2018), p. 623. DOI: 10.3389/fchem.2018.00623.

[7] E. Derouane. “Shape selectivity in catalysis by zeolites: the nest effect”. In: *J. Catal.* 100.2 (1986), pp. 541–544. DOI: 10.1016/0021-9517(86)90127-2.

[8] M.-O. Coppens et al. “Nature-inspired, computer-assisted optimization of hierarchically structured zeolites”. In: *Adv. Mater. Interfaces* 8.4 (2021), p. 2001409. DOI: 10.1002/admi.202001409.

[9] U. Tallarek et al. “Olefin ring-closing metathesis under spatial confinement: Morphology-transport relationships”. In: *ChemCatChem* 13.1 (2021), pp. 281–292. DOI: 10.1002/cctc.202001495.

[10] H. Kraus and N. Hansen. *PoreMS: v0.2.0*. Version v0.2.0. 2020. DOI: 10.5281/zenodo.3984865.

[11] H. Kraus et al. “PoreMS: a software tool for generating silica pore models with user-defined surface functionalisation and pore dimensions”. In: *Mol. Simul.* 47.4 (2021), pp. 306–316. DOI: 10.1080/08927022.2020.1871478.

[12] F. Ziegler et al. “Confinement Effects for Efficient Macrocyclization Reactions with Supported Cationic Molybdenum Imido Alkylidene N-Heterocyclic Carbene Complexes”. In: *ACS Catal.* 11 (2021), pp. 11570–11578. DOI: 10.1021/acscatal.1c03057.

[13] B. Coasne and J. T. Fourkas. “Structure and Dynamics of Benzene Confined in Silica Nanopores”. In: *J. Phys. Chem. C* 115.31 (2011), pp. 15471–15479. DOI: 10.1021/jp203831q. (Visited on 06/14/2021).

[14] T. S. Gulmen and W. H. Thompson. “Testing a Two-State Model of Nanoconfined Liquids: conformational Equilibrium of Ethylene Glycol in Amorphous Silica Pores”. In: *Langmuir* 22.26 (2006), pp. 10919–10923. DOI: 10.1021/la062285k.

[15] F. Ziegler et al. “Olefin Metathesis in Confined Geometries: a Biomimetic Approach toward Selective Macrocyclization”. In: *J. Am. Chem. Soc.* 141.48 (2019), pp. 19014–19022. DOI: 10.1021/jacs.9b08776.

[16] M. Ide et al. “Quantification of silanol sites for the most common mesoporous ordered silicas and organosilicas: Total versus accessible silanols”. In: *Phys. Chem. Chem. Phys.* 15.2 (2013), pp. 642–650. DOI: 10.1039/C2CP42811C.

[17] M. J. Abraham et al. “GROMACS: high performance molecular simulations through multi-level parallelism from laptops to supercomputers”. In: *SoftwareX* 1-2 (2015), pp. 19–25. DOI: 10.1016/j.softx.2015.06.001.

[18] B. Hess et al. “GROMACS 4: algorithms for Highly Efficient, Load-Balanced, and Scalable Molecular Simulation”. In: *J. Chem. Theory. Comput.* 4.3 (2008), pp. 435–447. DOI: 10.1021/ct700301q.

[19] J. Wang et al. “Development and testing of a general amber force field”. In: *J. Comput. Chem.* 25.9 (2004), pp. 1157–1174. DOI: 10.1002/jcc.20035.

[20] S. Nosé. “A molecular dynamics method for simulations in the canonical ensemble”. In: *Mol. Phys.* 52.2 (1984), pp. 255–268. DOI: 10.1080/00268978400101201.

[21] W. G. Hoover. “Canonical dynamics: equilibrium phase-space distributions”. In: *Phys. Rev. A* 31.3 (1985), pp. 1695–1697. DOI: 10.1103/physreva.31.1695.

[22] B. Hess et al. “LINCS: a linear constraint solver for molecular simulations”. In: *J. Comp. Chem.* 18.12 (1997), pp. 1463–1472. DOI: 10.1002/(sici)1096-987x(199709)18:12<1463::aid-jcc4>3.0.co;2-h.

[23] B. Hess. “P-LINCS: a Parallel Linear Constraint Solver for Molecular Simulation”. In: *J. Chem. Theory Comput.* 4.1 (2008), pp. 116–122. DOI: 10.1021/ct700200b.

[24] T. Darden, D. York, and L. Pedersen. “Particle mesh Ewald: An N log(N) method for Ewald sums in large systems”. In: *J. Chem. Phys.* 98.12 (1993), pp. 10089–10092. DOI: 10.1063/1.464397.

[25] U. Essmann et al. “A smooth particle mesh Ewald method”. In: *J. Chem. Phys.* 103.19 (1995), pp. 8577–8593. DOI: 10.1063/1.470117.

[26] H. Kraus, M. Högler, and N. Hansen. *PoreAna: 0.2.1*. Version v0.2.1. 2021. DOI: 10.5281/zenodo.5039999.

[27] G. Hummer. “Position-dependent diffusion coefficients and free energies from Bayesian analysis of equilibrium and replica molecular dynamics simulations”. In: *New J. Phys.* 7 (2005), p. 34. DOI: 10.1088/1367-2630/7/1/034.

[28] A. Ghysels et al. “Position-dependent diffusion tensors in anisotropic media from simulation: Oxygen transport in and through membranes”. In: *J. Chem. Theory Comput.* 13.6 (2017), pp. 2962–2976. DOI: 10.1021/acs.jctc.7b00039.

[29] M. von Smoluchowski. “Über Brownsche Molekularbewegung unter Einwirkung äußerer Kräfte und deren Zusammenhang mit der verallgemeinerten Diffusionsgleichung”. In: *Ann. Phys.* 353 (1916), pp. 1103–1112. DOI: 10.1002/andp.19163532408.

[30] P. Hänggi, P. Talkner, and M. Borkovec. “Reaction-rate theory: fifty years after Kramers”. In: *Rev. Mod. Phys.* 62.2 (1990), pp. 251–341. DOI: 10.1103/RevModPhys.62.251.

[31] H. Kraus and N. Hansen. *Supplementary material for ’Fluid structure and dynamics in mesoporous confinement’*. Version V1. 2021. DOI: 10.18419/darus-2039.

[32] F. Ziegler et al. “Olefin ring-closing metathesis under spatial confinement and continuous flow”. In: *ChemCatChem* 13.9 (2021), pp. 2234–2241. DOI: 10.1002/cctc.202001993.

[33] F. S. Emami et al. “Force field and a surface model database for silica to simulate interfacial properties in atomic resolution”. In: *Chem. Mater.* 26.8 (2014), pp. 2647–2658. DOI: 10.1021/cm500365c.

[34] F. S. Emami et al. “Correction to force field and a surface model database for silica to simulate interfacial properties in atomic resolution”. In: *Chem. Mater.* 28.1 (2016), pp. 406–407. DOI: 10.1021/acs.chemmater.5b04760.

5. Axial Diffusion in Liquid Saturated Cylindrical Silica Model Pores

Molecular dynamics simulations of solvent-filled cylindrical silica mesopores of 5 nm diameter are carried out to obtain a detailed molecular-level picture of the fluid structure and the self-diffusion coefficient in confinement. The focus of the study is to obtain the ratio between the bulk and the pore diffusion coefficient, a quantity often used in experimental work to draw conclusion on the tortuosity of a given material. For the straight pores studied in the present work this ratio is between two and three for all 14 solvent molecules studied independent of the computational approach used to obtain the average diffusion coefficient in the pore or whether the pore was carved out from crystalline or amorphous bulk silica. Therefore, it merely reflects the influence of the confinement perturbing the fluid relative to the bulk phase.

5.1. Introduction

Quantifying diffusion effects in mesoporous materials is of relevance for the characterization of the pore topology,[1] for design of chromatographic processes [2] and to assess possible diffusion limitations of chemical reactions catalyzed by active sites located on or close to the inner pore surface [3, 4]. Effective transport in the bulk material depends on geometric details of the pore topology and the chemical nature of the inner pore surface. Within a hierarchical modelling approach, it is therefore highly important to be predictive on all relevant length scales [5, 6]. However, the validation of computational results on diffusional transport in porous materials requires well-characterized experimental data [7]. For microporous materials such as zeolites large deviations between diffusion coefficients measured with different techniques were reported [8–10]. Parts of these differences are related to the different physical phenomena that are captured in uptake measurements and PFG NMR measurements, respectively [11]. By accounting for the loading dependence of the diffusion coefficient the agreement between different data sets could be improved [12]. In mesoporous materials such as silica, completely saturated with fluids, the static and dynamic fluid properties may differ from their corresponding bulk values and are affected by the pore diameter and the chemical nature of the inner surface of the pore [13, 14].

A structural parameter characterizing the pore topology is the tortuosity, often defined by the ratio of the actual path and the shortest path from A to B [15] or by the ratio of the two paths squared [16]. The latter definition can be approximated by the ratio of the bulk diffusion coefficient of a chemically inactive species and its diffusion coefficient measured under confinement [17, 18]. The notion of chemical inactivity is important to avoid any superimposed effect resulting from interactions with the pore walls that may lead to rather complex diffusion behavior such as a strong reduction or even an enhanced self-diffusivity [18, 19].

However, also structural properties such as constrictions, reduced connectivity or roughness affect the diffusion coefficient ratio [20]. Note that the ratio of bulk diffusion and diffusion inside the porous material is also interpreted as the ratio of the tortuosity and the porosity of the material [21–23]. However, in this definition pore diffusion refers to the effective mobility within the porous matrix and not within a single pore. Alkanes such as *n*-heptane or cyclohexane are often used as probe molecules to measure the tortuosity by pulsed field gradient NMR [24]. However, for pore sizes below 6 nm the tortuosity values start to depend on the pore size and, thus deviate from a purely structural definition [24–26]. For molecular heterogeneous catalysis in confined geometries this is the pore size where confinement effects are to be expected. Separating tortuosity from surface interaction effects is therefore an important step when developing predictive (multiscale) models. While various theoretical or empirical tortuosity-porosity relations have been proposed [27] random walk particle tracking simulations of inert tracer molecules inside physical reconstructions of real porous materials give a more direct access to these relations [5].

For a straight cylindrical mesopore of constant diameter the tortuosity is by (the structural) definition equal to one. Deviation from bulk diffusion can therefore only be due to confinement and can be conveniently probed by molecular dynamics simulations at atomistic resolution. Due to the controlled and well-defined environment such simulations help in dissecting the complex interplay of various physical effects interfering each other and leading to the observed behavior. In the present work 14 different solvent molecules are simulated in cylindrical silica pores of 5 nm diameter. The main focus was to obtain reliable ratios for the densities and self-diffusion coefficients between bulk and pore phase.

5.2. Methodology

5.2.1. Generation of Model Pores

The PoreMS python package [28] version 0.2.5 [29] was utilized to generate the pore systems composed of a cylindrical pore of 5 nm diameter carved out of a (7.08, 7.02, 10.08) nm (x, y, z) β-cristobalite block. On each side of the pore structure, a bulk reservoir with the length of 10 nm was attached, see Fig. 5.2.1. Using siloxane bridges, the hydroxylation degree of the internal and external surface was set to 6.06 µmol m^{-2}, corresponding to a partially hydroxylated surface.[30–32] Additionally, the exterior surface was configured with an end-capping of trimethylsilyl (TMS) in order to avoid excessive clustering of hydrophilic solvent molecules at the outer surface, resulting into a total bonded-phase coverage of around 90 %. Additionally, an amorphous silica block of (x, y, z) 9.84, 9.87, 10.7 from the study of Vink and Barkema [33] was used as starting material, targeting the same surface functionalization. The properties within the pore are mostly similar, except for a slightly smaller achieved pore size since the more randomized structure allows finer adjustments. The properties on the outer surface show some

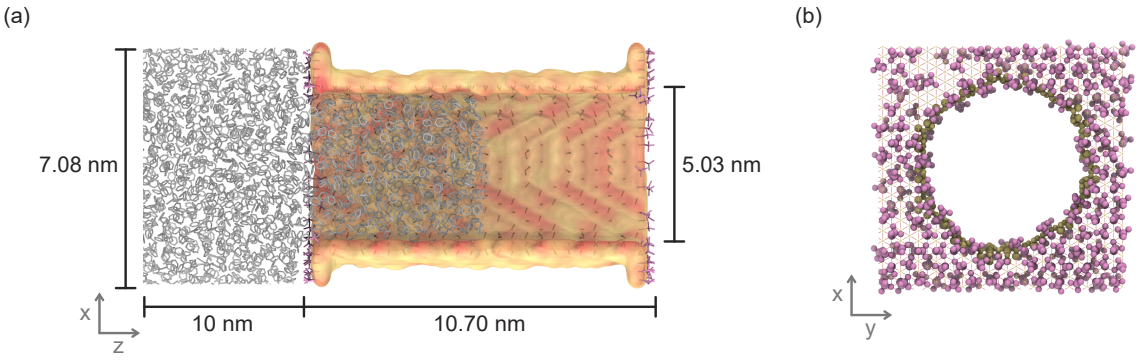

Figure 5.2.1.: (a) Side view of the simulation box filled with benzene indicating the length of the central silica block and the solvent reservoirs. (b) Front view of the pierced silica block containing the 5 nm diameter pore. The chemistry of the exterior surface is based on the (111) face of β-cristobalite silica. Bonded-phase groups are randomly distributed on the silica surface. Ligand densities, residual surface hydroxylation, and further details are specified in Table 5.2.1. Colour code: Si, yellow lines/surface; O, red lines/surface; trimethylsilyl, pink; surface silanol groups, yellow; benzene, gray.

differences to the crystalline material. First, the surface roughness is larger than zero due to the uneven surface which is completely smooth in the ideal case, and second, the hydroxylation degree reduction is more limited, because the positions of the silanol groups are more randomly distributed which leads to difficulties when searching for two close silanol groups for siloxane bridge conversion. Since the difference in the hydroxylation degree is small, and it can be assumed that its effect will no be detrimental to the analysis within the pore, this dissimilarity is of minor importance when comparing diffusion coefficients in the two materials. Further properties of the pores are listed Table 5.2.1 while Fig. 5.2.2 shows the radial distribution functions (rdf) of the two bulk materials.

Table 5.2.1.: Properties of the cylindrical mesopore model before and after functionalization (func).[a]

	Crystalline		Amorph	
	Interior	Exterior	Interior	Exterior
Silica block xyz-dim.	7.08; 7.02; 10.70		9.84; 9.87; 10.70	
Pore drilling direction	z		z	
Pore diameter	5.03		5.01	
Surface roughness[b]	0.08	0.00	0.08	0.15
Solvent reservoir z-dim.		10.00		10.00
Simulation box xyz-dim.	7.08; 7.02; 30.70		9.84; 9.87; 30.70	
Pore volume	196.84		189.37	
Solvent reservoir volume		2×496.97		2×970.69
Surface area	156.65	2×29.86	151.18	2×72.54
Surface chemistry before func.				
Num. of single silanol groups	472	174	370	402
Num. of geminal silanol groups	48	22	90	86
Num. of siloxane bridges	145	49	190	217
Total number of OH groups	570	218	550	574
Overall hydroxylation	6.04	6.06	6.04	6.57
Surface chemistry after func.				
Num. of TMS groups	0	196	0	358
TMS density	0	5.45	0	4.10
Bonded-phase density	0	5.45	0	4.10
Num. of residual OH groups	570	22	550	216
Residual hydroxylation	6.04	0.61	6.04	2.47

[a]Pore diameter (in nm) and surface densities (in $\mu mol\,m^{-2}$) are reported for a cylindrical pore carved through a β-cristobalite structure generated by PoreMS [28, 29] and an amorphous structure reported by Vink and Barkema [33]. [b]Calculated as the standard deviation of the shortest distances between the central pore axis and the surface Si atoms within the pore and between the xy-plane and the surface Si atoms on the outer surface.

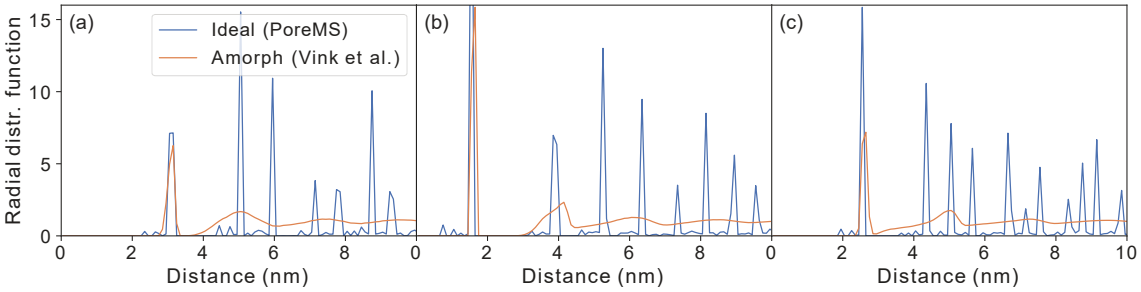

Figure 5.2.2.: Radial distribution functions for (a) Si-Si, (b) Si-O, and (c) O-O pairs, of an ideal β-cristobalite structure generated by PoreMS [28, 29] and an amorphous structure reported by Vink and Barkema [33].

5.2.2. Calculation of Density and Self-Diffusion

The radial number density and diffusion coefficient profiles were calculated using the PoreAna package version 0.2.3 [34]. For the radial number density profile the cross-sectional area of the pore was discretized into annuli of equal area. In each bin the number density was then calculated according to

$$\rho_r = \frac{N_r}{V_r} = \frac{N_r}{\pi l} \frac{1}{\delta_r^2 - \delta_{r-1}^2}. \tag{5.2.1}$$

where N_r represents the number of molecules in the volume element $V_r = \pi l(\delta_r^2 - \delta_{r-1}^2)$, with l being the length of the pore and δ the two radii defining the annulus. For annuli of constant area the calculation of the mean density simplifies to a normal average

$$\langle \rho \rangle = \frac{\sum \rho_r V_r}{\sum V_r} = \frac{1}{M} \sum \rho_r. \tag{5.2.2}$$

where M is the number of bins. Note that the value of the mean density depends on the choice of the largest δ_r-value due to the strong depletion of the density close to the pore surface. As a result the mean density is an ambiguous quantity which hampers comparison between experiment and simulation.

Diffusion coefficients were determined using two distinct methods. The first approach is the Einstein relation[35]

$$\lim_{t\to\infty} \left\langle (\boldsymbol{r}_i(t+\tau) - \boldsymbol{r}_i(\tau))^2 \right\rangle_{i,\tau} = 2nD_{\mathrm{E}}t + \mathrm{const} \tag{5.2.3}$$

where $\boldsymbol{r}_i$ is the instantaneous molecular position (following molecules across periodic boundaries), $\langle ... \rangle_{i,\tau}$ stands for averaging over all molecules i and time origins τ and n is the dimensionality of the system in which diffusion occurs. According to Yeh and Hummer [36], the diffusion coefficient is dependent on the simulation box size due to finite size effects, and therefore needs to be corrected by extrapolating the coefficient towards an infinite box length.

For pore systems, similar to the density calculation, a radial binning approach was utilized. Hereby a diffusion coefficient $D_{\mathrm{E},r} := D_{\parallel,\mathrm{E},r}$ parallel to the pore surface is calculated within each radial bin r from the slope of the mean square displacement $\Delta_r(t)$ over an observation time of 4-20 ps with a tolerance of ± 1 bins

$$D_{\mathrm{E},r} = \frac{1}{2} \frac{\mathrm{d}\Delta_r(t)}{\mathrm{d}t}. \tag{5.2.4}$$

By weighting the axial diffusion profile D_{E} with the density profile ρ along the radius δ, a mean diffusion coefficient $\langle D_{\mathrm{E}} \rangle$ was calculated according to

$$\langle D_{\mathrm{E}} \rangle = \frac{\sum \rho_r D_{\mathrm{E},r} A_r}{\sum \rho_r A_r} = \frac{\sum \rho_r D_{\mathrm{E},r} (\delta_r^2 - \delta_{r-1}^2)}{\sum \rho_r (\delta_r^2 - \delta_{r-1}^2)} = \frac{\sum \rho_r D_{\mathrm{E},r}}{\sum \rho_r}. \tag{5.2.5}$$

where the equisized annular areas are cancelling out.

The second method proposed by Hummer[37] and further developed by Ghysels et al. [38], determines a spatially resolved diffusion profile using Bayesian analysis. The Smoluchowski equation [39] in z-direction describes the time evolution of the probability density $p(z,t)$ along the coordinate z

$$\frac{\partial p(z,t)}{\partial t} = \frac{\partial}{\partial z} \left\{ D_{\mathrm{S}}(z) e^{-\beta F_{\mathrm{S}}(z)} \frac{\partial}{\partial z} \left[e^{\beta F_{\mathrm{S}}(z)} p(z,t) \right] \right\}, \quad \beta^{-1} = k_{\mathrm{B}} T \tag{5.2.6}$$

with Boltzmann constant k_{B}, absolute temperature T, and diffusion $D_{\mathrm{S}} =: D$ and free energy profiles $F_{\mathrm{S}} =: F$ along the z-axis. Spatial discretization of the first factor [40]

$$D(z) e^{-\beta F(z)} \Big|_{z_i + \frac{\Delta z}{2}} \approx D_{i+\frac{1}{2}} e^{-\beta \frac{F_i + F_{i+1}}{2}} \tag{5.2.7}$$

with bin $i = 1, \ldots, n$, the approximation of the second term by the difference quotient

$$\frac{\partial}{\partial z}\left[e^{\beta F(z)}\, p(z,t)\right]\Big|_{z_i+\frac{\Delta z}{2}} \approx \frac{1}{\Delta z}\left(e^{\beta F_{i+1}}\, p_{i+1} - e^{\beta F_i}\, p_i\right) \tag{5.2.8}$$

and applying the divergence theorem, results in

$$\begin{aligned}\frac{\partial p_i}{\partial t} \approx & \frac{D_{i+\frac{1}{2}}}{\Delta z^2}\left[e^{\frac{-\beta(F_i - F_{i+1})}{2}}\, p_{i+1} - e^{\frac{-\beta(F_{i+1} - F_i)}{2}}\, p_i\right] \\ & + \frac{D_{i-\frac{1}{2}}}{\Delta z^2}\left[e^{\frac{-\beta(F_i - F_{i-1})}{2}}\, p_{i-1} - e^{\frac{-\beta(F_{i-1} - F_i)}{2}}\, p_i\right]\end{aligned} \tag{5.2.9}$$

with notation $D_i := D(z_i)$, and thus

$$\frac{d\boldsymbol{p}}{dt} = \boldsymbol{R}\boldsymbol{p}. \tag{5.2.10}$$

Hereby the rate-matrix $\boldsymbol{R} \in \mathbb{R}^{n\times n}$ contains the prefactors of the probability density and thereby describing the diffusion and free energy values. The secondary diagonal elements are given by

$$\begin{aligned}R_{i,i+1} &= \frac{D_{i+\frac{1}{2}}}{\Delta z^2} e^{\frac{\beta(F_{i+1} - F_i)}{2}};\; R_{i+1,i} = \frac{D_{i+\frac{1}{2}}}{\Delta z^2} e^{\frac{\beta(F_i - F_{i+1})}{2}} \\ R_{i,i-1} &= \frac{D_{i-\frac{1}{2}}}{\Delta z^2} e^{\frac{\beta(F_{i-1} - F_i)}{2}};\; R_{i-1,i} = \frac{D_{i-\frac{1}{2}}}{\Delta z^2} e^{\frac{\beta(F_i - F_{i-1})}{2}}\end{aligned} \tag{5.2.11}$$

and the diagonal elements result from combining the neighbouring entries

$$R_{i,i} = -R_{i-1,i} - R_{i+1,i}. \tag{5.2.12}$$

Due to periodic boundary conditions, the corners of the matrix are treated differently

$$\begin{aligned}R_{n,1} &= \frac{D_{n+\frac{1}{2}}}{\Delta z^2} e^{\frac{\beta(F_1 - F_n)}{2}};\; R_{1,1} = -R_{2,1} - R_{n,1}, \\ R_{1,n} &= \frac{D_{n+\frac{1}{2}}}{\Delta z^2} e^{\frac{\beta(F_n - F_1)}{2}};\; R_{n,n} = -R_{n-1,n} - R_{1,n}.\end{aligned} \tag{5.2.13}$$

A time discretization of the solution of the matrix equation

$$\boldsymbol{p}(t) = e^{\boldsymbol{R}t}\boldsymbol{p}(0) \tag{5.2.14}$$

allows the definition of the propagator

$$p(i, t_i | j, t_j) = \left[e^{\boldsymbol{R}\Delta_{ij} t_\alpha}\right]_{ij}, \tag{5.2.15}$$

which describes the probability for a molecule to move from bin j at time t_j to bin i at time t_i. The time elapsing between these two time instances is referred to as lag time $\Delta t_\alpha = \Delta_{ij} t_\alpha = t_j - t_i$. Utilizing Bayesian analysis

$$p(M|T) \propto p(T|M)p(M), \tag{5.2.16}$$

with prior probability $p(M)$ expressing the probability of the model parameter M and posterior probability $p(M|T)$ describing the probability of the model parameter M for given data T, the propagator is used to determine the likelihood term $L(M) := p(T|M)$, which in turn represents the probability of data T for a given model M. This is done by weighting the propagator with the frequency of bin transition N_{ij}

$$\ln L(M) = \sum_{j\to i} \ln\left\{\left[\left(e^{\boldsymbol{R}\Delta t_\alpha}\right)_{ij}\right]^{N_{ij}(\Delta t_\alpha)}\right\}. \tag{5.2.17}$$

The transition matrix $\boldsymbol{N}(\Delta t_\alpha) \in \mathbb{R}^{n\times n}$ contains the number of all observed transitions $j \to i$ at a given lag time Δt_α and is sampled during the simulation. Finally, the model M is represented by a Fourier series for the diffusion

$$\ln\left(D_{i+\frac{1}{2}}\right) = a_0 + \sum_{k=1}^{n_k} a_k \cdot \cos\left(\frac{2\pi k i}{n}\right) \tag{5.2.18}$$

and for the free energy profile

$$F_i = a_0 + \sum_{k=1}^{n_k} a_k \cdot \cos\left[\frac{2\pi k(i+0.5)}{n}\right]. \tag{5.2.19}$$

During the Bayesian analysis, the likelihood is sampled by performing a Monte Carlo (MC) random walk with the coefficients a_k from the Fourier series as the model parameters. The likelihood is then used in the acceptance criterion

$$\xi < \exp\left(\frac{\ln L_{\text{new}} - \ln L_{\text{old}}}{T}\right) \tag{5.2.20}$$

with random number $\xi \in [0,1]$ to optimize the model coefficients a_k during multiple MC cycles. This Bayesian approach however, does not discriminate between long and short time periods which leads to inaccurate diffusion values [38]. Therefore the diffusion profiles are extrapolated linearly towards an infinite lag time $(\Delta t_\alpha)^{-1} \to 0$. The self-diffusion coefficient is then determined as a mean value over the extrapolated profile. Alternatively specific profile sections (e.g. pore area) can be chosen for averaging.

5.2.3. Molecular Models and Simulation Setup

The solvent molecules were described with AMBER-compatible force fields. For alcohols the GAFF-DC parameters proposed by Fennel et al. [41] were used. Linear and cyclic alkanes were described with parameters derived by Nikitin et al. [42] Aromatic molecules were described by the general AMBER force field (GAFF) [43] topologies provided via the FreeSolv database [44]. For water the TIP4P/2005 model was employed [45]. Finally tetrahydrofuran was simulated using the second generation GAFF2 due to the better agreement of both density and self-diffusion coefficient with experiment. The still significant underestimation of the experimental self-diffusion coefficient (see table 5.3.1) could be remedied by a reparametrization of the model [46] which was, however, beyond the scope of the present work. Figure 5.2.3 shows relative deviations between densities obtained from molecular dynamics (MD) simulations and experimental data for all 14 solvent molecules at 295 K.
The Lennard-Jones parameters for the silica lattice, including the silanol groups were taken from Coasne et al. [49], and the partial charges atoms from Gulmen and Thompson [50] as in previous work [51]. These parameters are listed in the supporting information in table S1. The possible occurrence of deprotonated silanol groups on the surface [52] was not considered. For the TMS surface group GAFF was used, following earlier work [51, 53, 54].
The pore simulations were prepared using the open source PoreSim [55] python package, which generates a simulation directory structure as well as scripts that automatize the insertion of molecules into the simulation box containing the pore. The simulation suite GROMACS 2019.6 [56, 57] was used for all simulations.

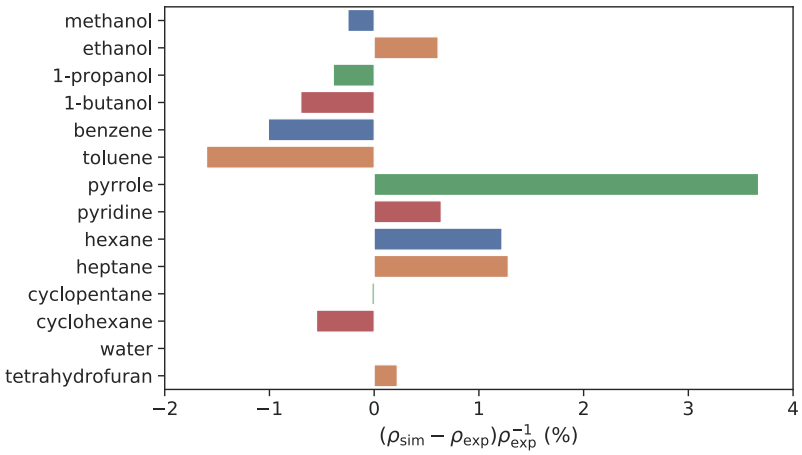

Figure 5.2.3.: Relative deviation of simulated densities from experimental data.[47, 48]

All MD simulations were performed under periodic boundary conditions. Temperature was controlled using the Nosé-Hoover thermostat [58, 59] with a coupling constant of 1 ps, while pressure for simulations in the NpT ensemble was controlled by the Parrinello-Rahman barostat [60, 61] with a coupling constant of 5.0 ps and compressibility of 4.5×10^{-5} bar^{-1}. Bond lengths between heavy atoms and hydrogens were constrained with the LINCS algorithm [62, 63] with an order of 4. Short-range electrostatic and Lennard-Jones parameters were evaluated up to a cutoff distance of 1.4 nm. Analytical dispersion corrections for energy and pressure were included. Long-range electrostatic interactions were treated with the particle-mesh Ewald algorithm [64, 65].
The NpT simulation for the bulk phase systems were run for 50 ns with a time-step of 2 fs after a total equilibration time of 10 ns. The pore systems simulated in the NVT ensemble were iteratively filled with solvent molecules until the density in the reservoir region corresponds to the density of prior pure solvent NpT simulation at the desired thermodynamic state (T = 295 K, p = 1 bar). Table 5.3.1 shows that the largest deviation between the two density values occurs for cyclohexane with a relative deviation of only 0.13%.
During the simulation of the pore systems, silicon and oxygen grid atoms were frozen in their position to preserve the original pore shape, this includes the silicon atom of surface groups. For these systems a trajectory length of 200 ns was generated with a time-step of 1 fs and a total equilibration time of 50 ns.

5.3. Results and Discussion

5.3.1. Bulk phase simulations

The purpose of the bulk phase simulations is threefold. First, the equilibrium density at $T = 295\,\mathrm{K}$ and $p = 1\,\mathrm{bar}$ was determined for all solvent models in NpT simulations. Second, subsequent NVT simulations at this density were then employed to determine the self-diffusion coefficients with the Einstein and Smoluchowski approach, respectively, in order to evaluate the equivalency of the two approaches. Third, a comparison between simulated and experimental density and self-diffusion coefficient values was used to evaluate whether the force fields are able to reproduce both static and dynamic properties. Figure 5.3.1 illustrates the calculation of the self-diffusion coefficient for methanol with the Smoluchwski approach for three different system sizes. The diffusion coefficients were determined with 10^7 equilibration and production steps respectively for the Monte Carlo sampling for multiple lag times (20 ps, 40 ps, 60 ps, 80 ps, 100 ps, 120 ps) and then extrapolated towards an infinite lag time.

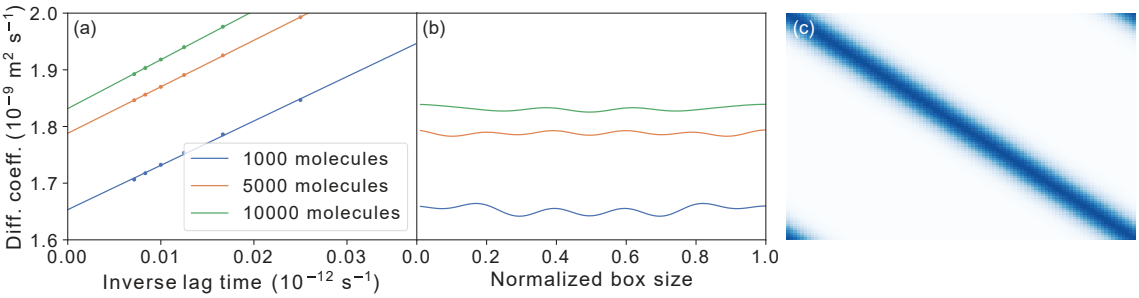

Figure 5.3.1.: Illustration of the calculation of bulk diffusion coefficients for methanol using the Smoluchowski approach. (a) Fitting of the diffusivity as function of the inverse lag time for three different system sizes. (b) Diffusion profiles along the normalized simulation box length. (c) Visualization of the transition matrix for a lag time of 20 ps.

Since the diffusion coefficients depend on the system-size [36] they were extrapolated towards an infinite box size. This was done over three simulations in cubic boxes with increasing number of molecules (1000, 5000, 10 000) as shown in figure 5.3.2. The values at infinite box-size are compared to experimental data in table 5.3.1. The analysis of the experimental data is discussed in the appendix in section A.3.2, individual data points from the different bulk-simulation are available in the appendix in section A.3.3, and additional figures for the Smoluchowski approach (transition matrices, diffusion profiles, and extrapolation curves) are provided in the appendix in section A.3.4 in the supporting information.

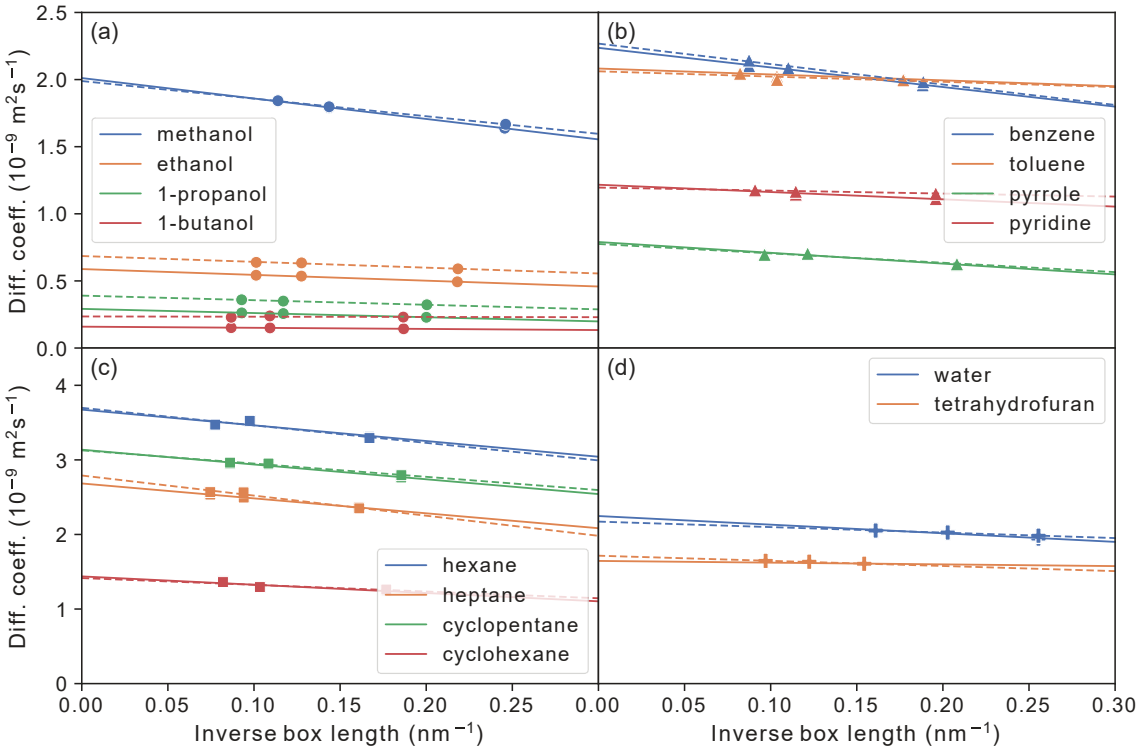

Figure 5.3.2.: Extrapolation of self-diffusion coefficients towards an infinite box size for (a) alcohols, (b) aromatics, (c) alkanes, and (d) water and tetrahydrofuran, using the Einstein method (eq. (5.2.3), solid lines) and the Smoluchowski equation (eq. (5.2.6), dashed lines).

Table 5.3.1 shows that the Einstein and Smoluchowski approaches are in good agreement, with the highest deviation seen for the alcohol molecules. The reason is the lag time extrapolation in the Smoluchowski approach where the single diffusion coefficients from the different lag times do not align on a linear curve but show a slight curvature instead (see figure S9). However, it can be concluded that the Smoluchowski approach is a reliable alternative to the Einstein method and can thus be used to determine diffusion coefficients in the pore simulations, representing an inhomogeneous system, which is more difficult to treat with the Einstein method. Comparison between simulation and experiment shows a particular good agreement for alkanes. Aromatic molecules show a good agreement for benzene and toluene while simulations for pyridine and pyrrole underestimate the experimental values. However, since the focus of the present work is the ratio between bulk and pore diffusion the selected molecular models show sufficient accuracy.

5.3.2. Pore simulations

For assessing the impact of confinement on the self-diffusion, pore simulations in the NVT ensemble were conducted with the pure solvent for 200 ns. Figure 5.3.3 shows radial density profiles of all solvent molecules. Except for water, all solvents display a significant fluid structure. The oscillation of the density is particularly strong for the cyclic alkanes and tetrahydrofuran. For the other molecules the bulk density is approached in the pore center. Figure 5.3.4 illustrates the molecular layers of cyclopentane.

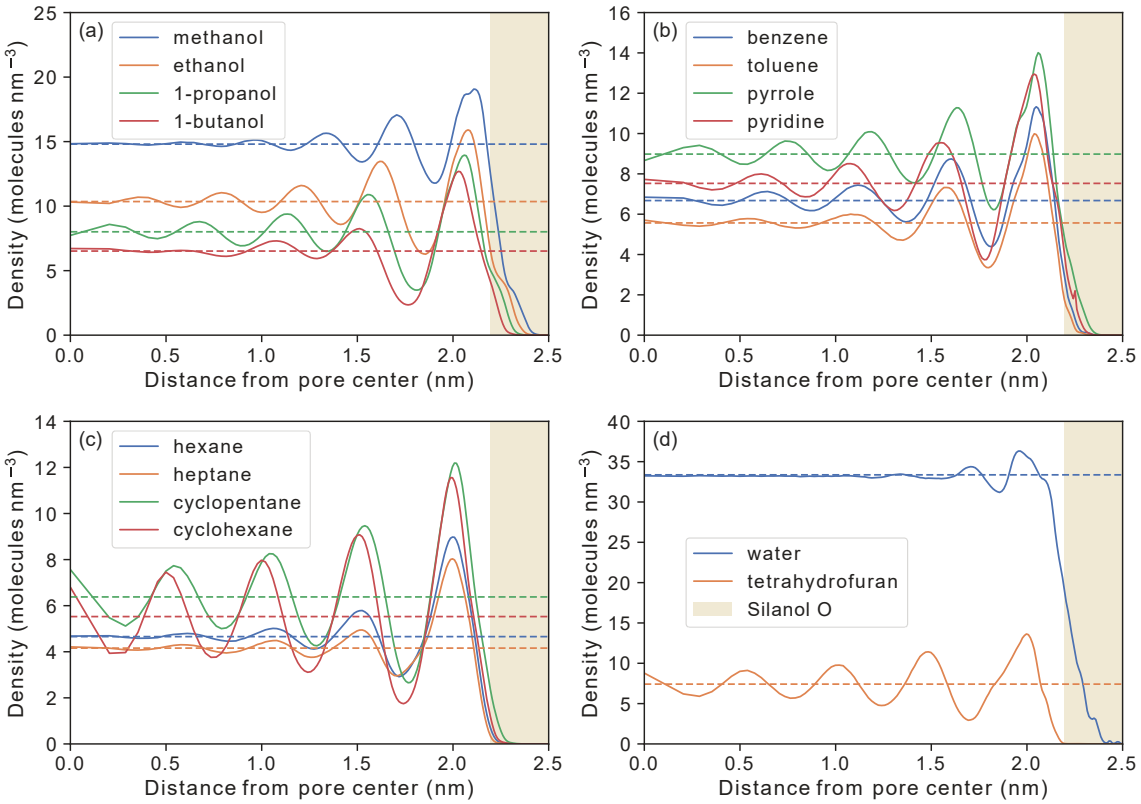

Figure 5.3.3.: Radial density profiles of the molecules' center of mass for (a) alcohols, (b) aromatics, (c) alkanes, and (d) water and tetrahydrofuran. The dashed lines indicate the bulk densities. The shaded area denotes the configurational space of the silanol oxygen atoms.

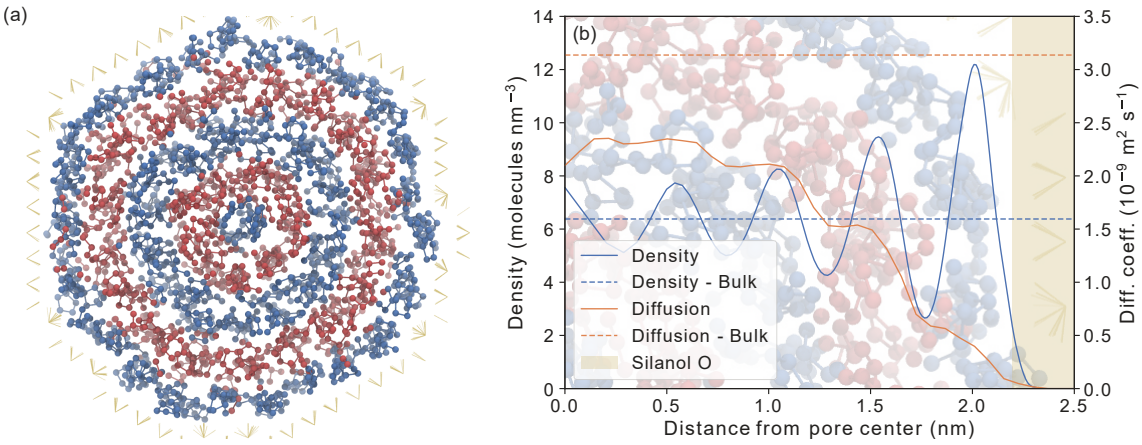

Figure 5.3.4.: (a) Frontal view of the pore with marked cyclopentane layers (alternating blue and red). The pores surface is indicated by the yellow silanol groups. (b) Radial density (blue) and diffusion (orange) profiles within the pore filled with cyclopentane.

Table 5.3.1.: Self-diffusion coefficients in the bulk phase at 295 K from simulation at constant volume and from experiment.[a]

Molecule	D_E	D_S	D_{Exp}	References
methanol	2.01	1.99	2.20(9)	[66–71]
ethanol	0.59	0.69	0.97(4)	[66, 68–73]
1-propanol[b]	0.29	0.39	0.58(2)	[66, 69, 73]
1-butanol[b]	0.16	0.24	0.43(4)	[66, 73]
benzene	2.24	2.27	2.10(4)	[68, 71, 72, 74–77]
toluene[b]	2.08	2.06	2.07(2)	[78]
pyrrole	0.79	0.78	1.53	[66]
pyridine[b]	1.22	1.20	1.83(28)	[68, 79]
hexane[b]	3.67	3.70	4.01(16)	[80]
heptane[b]	2.68	2.79	3.11(9)	[81]
cyclopentane[b]	3.14	3.13	3.32(20)	[66, 79]
cyclohexane[b]	1.44	1.42	1.40(3)	[73]
water	2.25	2.17	2.03(5)	[82–84]
tetrahydrofuran[b]	1.65	1.72	2.72(40)	[68]

[a]Diffusion coefficients (in $10^{-9}\,m^2\,s^{-1}$) D_E and D_S refer to the Einstein and Smoluchowski approach, respectively, and are extrapolated to infinite box size. D_{Exp} refers to experimental data.
[b]For these compounds error bars for the experimental values were calculated from reported values at 295 K due to the better data availability at this temperature compared to 295 K.

In table 5.3.2 density ratios between pore and reservoir region are compared to experimental density ratios reported by Agrawal et al. [66]. As noted previously the calculated value of the mean density in the pore depends significantly on the choice of the cutoff radius. This is illustrated in figure S13, showing the running average of the density as function of the cutoff radius. Therefore, two quantities are reported in table 5.3.2. First, the radius r_1 at which the running average of the density approaches the bulk density [85] and second the maximum value of the running average which is in all cases obtained just outside the surface region covered by silanol groups. Except for water and THF, r_1 has an almost constant value of 2.26 nm. Since water does only show moderate fluctuations of the radial density (see also Refs [86–88]) the running average starts to decrease below the bulk value already at 2.1 nm. For THF a value of 2.18 nm is obtained. Due to the ambiguity in the mean density values a direct comparison to experimental data is difficult since the latter also depend on the definition of the accessible pore volume [13]. However, for the alkanes the experimental values reported by Agrawal et al. [66] are significantly larger than those found in the simulation.

Table 5.3.2.: Bulk density (in $kg\,m^{-3}$) and ratio of pore and bulk density from simulation and experiment at 295 K.[a]

Molecule	ρ_{Exp}	ρ_{Bulk}	ρ_{Res}	r_1	$\left(\frac{\rho_{Pore}}{\rho_{Res}}\right)^{max}_{Sim}$	$\left(\frac{\rho_{Pore}}{\rho_{Bulk}}\right)_{Exp}$
methanol	789.86(67)	787.90	787.82	2.255	1.02	1.12
ethanol	787.78(12)	792.55	792.54	2.250	1.03	1.11
1-propanol	802.47(70)	799.33	799.26	2.255	1.04	1.01
1-butanol	808.98(106)	803.30	802.85	2.265	1.05	0.98
benzene	876.42(74)	867.58	867.21	2.265	1.07	0.99
toluene	865.42(93)	851.57	850.97	2.265	1.08	0.96
pyrrole	964.97	1000.37	999.69	2.255	1.05	1.14
pyridine	982.00	988.26	988.35	2.265	1.06	1.10
hexane	657.97(23)	665.99	665.94	2.265	1.10	1.25
heptane	682.81(96)	691.56	691.32	2.265	1.11	1.25
cyclopentane	743.33	743.21	743.26	2.265	1.19	1.62
cyclohexane	776.60(14)	772.35	771.35	2.250	1.23	1.31
water	997.83(8)	997.84	997.91	2.100	1.00	
THF	885.14	887.09	888.04	2.180	1.18	

[a] The experimental density values, ρ_{Exp}, were obtained from the DDB database [47], except for THF, for which the data from Chen et al. was used [48]. Simulated bulk densities are presented from constant pressure simulations of bulk fluid (ρ_{Bulk}) and from constant volume simulations of the pore system, restricting the analysis to the fluid reservoirs (ρ_{Res}). The ratios of experimental pore and bulk density values were reported by Agrawal et al. [66]. Due to the ambiguity in the definition of average fluid densities within mesopores only the maximum possible density obtained by integration over the simulated density profiles is reported (see eq. (5.2.2)). With r_1 we refer to the integration radius at which the averaged pore density according to eq. (5.2.2) equals the bulk density.

Figure 5.3.5 shows radial diffusion profiles determined by the Einstein equation (eq. (5.2.3)). Surface interactions of the molecules result in a decrease of mobility close to the surface. Similar to the density profiles, with increasing distance from the surface, the surface effect is reduced and the diffusion coefficients approach the bulk values in the case of the alcohols while they stay below the bulk values for the other species. The layering effect seen in the density profiles for the cyclic alkanes (figures 5.3.3 and 5.3.4) also appears in the diffusion profiles.
Figure 5.3.6 shows the profiles of the average self-diffusion coefficient along the z-axis from one reservoir through the pore into the other reservoir.

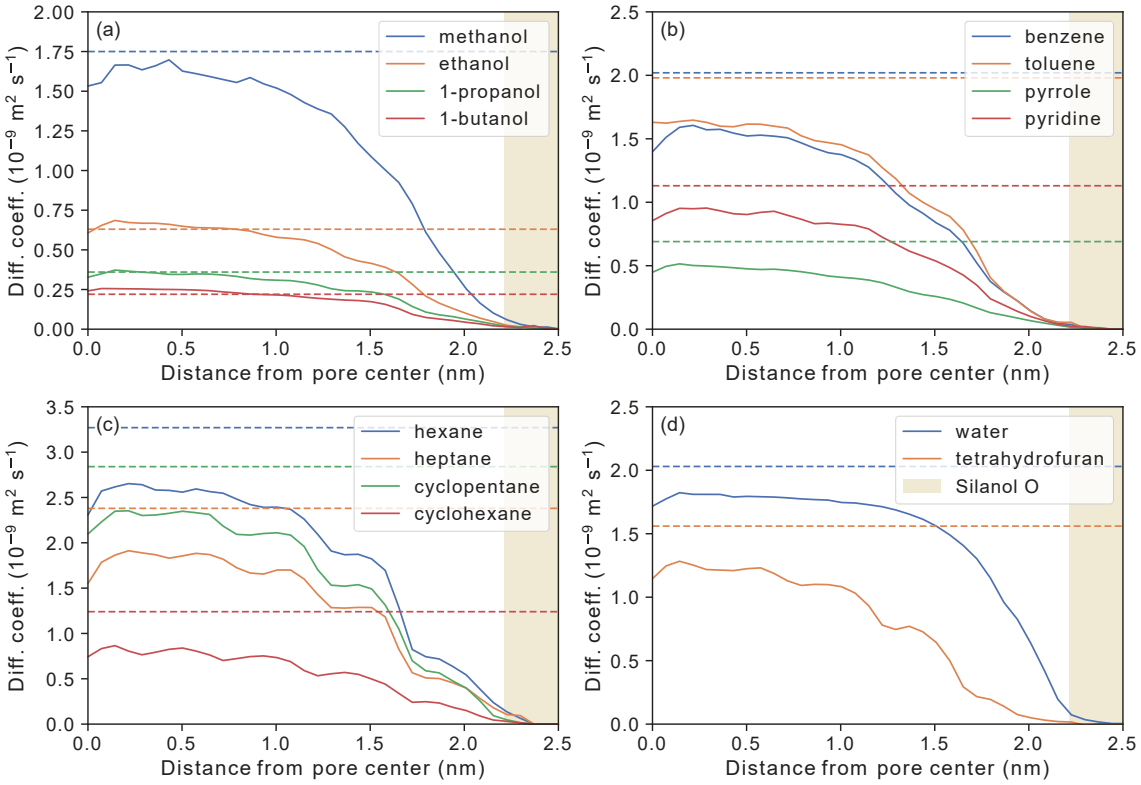

Figure 5.3.5.: Radial diffusion profiles of the molecules' center of mass calculated using the Einstein equation (eq. (5.2.3)) for (a) alcohols, (b) aromatics, (c) alkanes, and (d) water and tetrahydrofuran. The dashed lines indicate the bulk diffusion coefficient. The shaded area denotes the configurational space of the silanol oxygen atoms.

These profiles were calculated with the Smoluchowski approach from equation (5.2.6) using the same lag times as in the prior bulk simulations (20 ps, 40 ps, 60 ps, 80 ps, 100 ps, 120 ps) before extrapolating to infinity. The oscillations seen in the profiles are a consequence of the periodic model functions (see eq. (5.2.18)) and have no physical relevance. In all cases the self-diffusion is reduced inside the confinement while in the reservoir region the reference values from independent bulk phase simulations (dashed lines) are approached. This allows to extract a reasonable value for the ratio of bulk and pore diffusion coefficients from a single simulation, given that the reservoir was chosen large enough to reduce the influence of the outer pore surface. However, it should be emphasized that additional bulk simulations in elongated boxes having the same dimension as the pore system including the pore and the two reservoirs were conducted to obtain these reference values. Such simulations are required because in rectangular boxes diffusion becomes anisotropic [89] such that it cannot be expected that the diffusion coefficient calculated in the z-direction of the reservoir region approaches the value obtained in a cubic box of similar size. As shown in table S3 the diffusion coefficient in z-direction of the elongated bulk box is significantly smaller than the one obtained in cubix boxes and extrapolated to infinite system size. Transition matrices, lag time extrapolation, and diffusion and free energy profiles along the z-coordinate, are supplied in the appendix in section A.3.7.

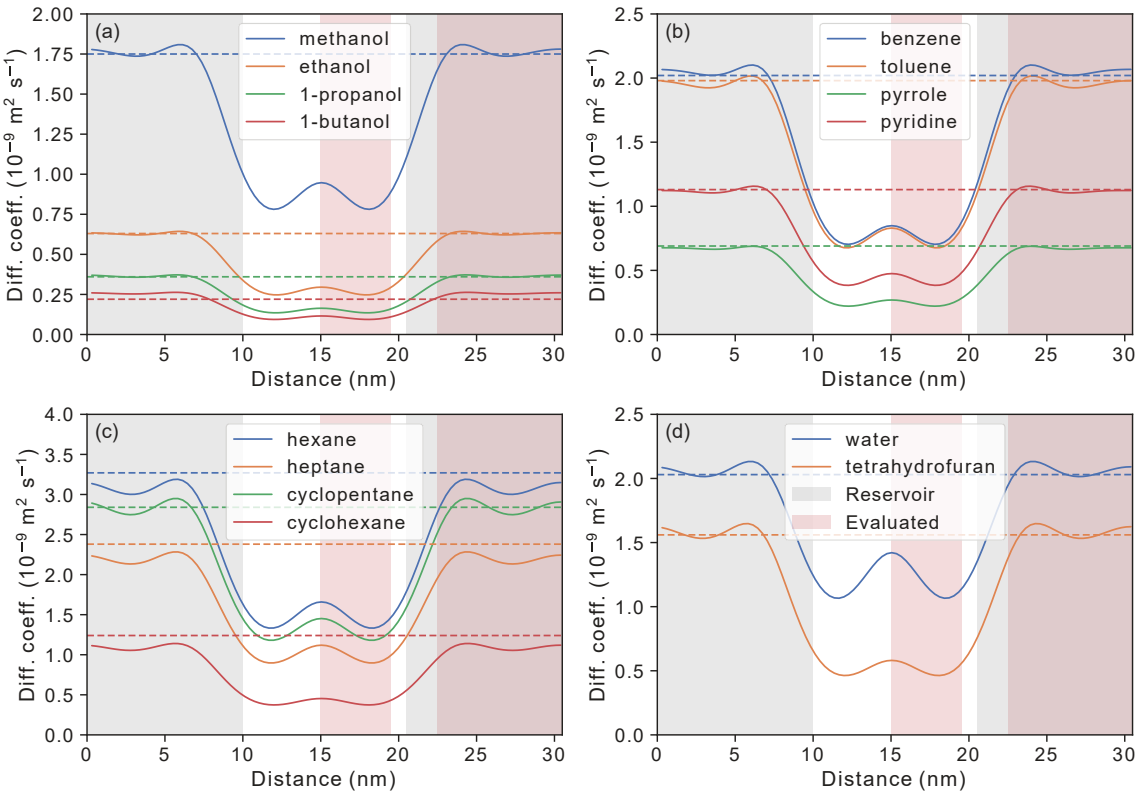

Figure 5.3.6.: Diffusion profiles along the z-direction of an elongated simulation box including a pore flanked by two solvent reservoirs, calculated using the Smoluchowski equation (eq. (5.2.6)) for (a) alcohols, (b) aromatics, (c) alkanes, and (d) water and tetrahydrofuran. The dashed lines represent diffusion coefficients in the z-direction determined from bulk simulations in elongated systems of the same size. The gray shaded areas denote the reservoir space and the red shade refers to the section used to average the area specific (pore, reservoir) diffusion coefficients.

The final results of both methods, Einstein and Smoluchowski are compared to each other and to the experimental data from Agrawal et al. [66] in table 5.3.3. The first two numerical columns show that for the majority of solvents the diffusion coefficient obtained in the reservoir region is in very good agreement with the reference values obtained in the z-direction of an elongated bulk box. Moreover, the average diffusion coefficient in the pore calculated with the Einstein equation is in very good agreement with the one from the Smoluchowski approach. However, the latter approach is preferred because it allows to obtain entire diffusion profiles along the box. The ratio of reservoir and bulk diffusion has values between two and three which is significantly smaller than the experimental ratios reported by Agrawal et al. [66]. However, for some of the solvents (benzene, heptane and cyclohexane) other authors reported significantly smaller ratios measured in pores of comparable diameters. While the reason for this discrepancy is difficult to specify we hope that molecular simulations may help to establish reference values for well-defined mesoporous materials. For water the simulation results are in good agreement with the experimental source [91] while for THF no experimental data was found.

Table 5.3.3.: Simulated Self-Diffusion coefficients ($10^{-9}\,m^2\,s^{-1}$) in Bulk and Pore Environments at 295 K and Their Ratio Compared to Reported Experimental Ratios.[a]

Molecule	$D^z_{\mathrm{rect,S}}$	$D_{\mathrm{Res,S}}$	$\langle D\rangle_{\mathrm{Pore,E}}$	$D_{\mathrm{Pore,S}}$	$\left(\frac{D_{\mathrm{Res}}}{D_{\mathrm{Pore}}}\right)_{\mathrm{S}}$	$\left(\frac{D_{\mathrm{Bulk}}}{D_{\mathrm{Pore}}}\right)_{\mathrm{Exp}}$
methanol	1.75	1.76	0.89	0.85	2.07	5.65[b]
ethanol	0.63	0.63	0.34	0.27	2.33	5.10[b]
1-propanol	0.36	0.36	0.19	0.15	2.40	4.26[b]
1-butanol	0.22	0.26	0.13	0.10	2.60	2.60[b]
benzene	2.02	2.05	0.75	0.77	2.66	12.71[b],1.96[c]
toluene	1.98	1.96	0.80	0.74	2.65	12.15[b]
pyrrole	0.69	0.67	0.24	0.24	2.79	12.28[b]
pyridine	1.13	1.12	0.46	0.43	2.60	7.35[b]
hexane	3.28	3.08	1.44	1.47	2.10	9.29[b]
heptane	2.38	2.19	1.01	0.99	2.21	10.15[b],1.2[d],1.48[e],3[f]
cyclopentane	2.84	2.83	1.20	1.29	2.19	11.52[b]
cyclohexane	1.24	1.09	0.42	0.41	2.66	9.32[b],1.23[d],1.5[e],3[f]
water	2.03	2.06	1.26	1.21	1.70	1.35[g]
THF	1.56	1.58	0.57	0.51	3.10	

[a]The subscript S refers to the Smoluchowski method, the subscript E to the Einstein method. $D^z_{\mathrm{rect,S}}$ represents the diffusion coefficient in the z-direction of an elongated bulk system (without a pore) of the same dimensions as the pore system shown in Fig. 5.2.1. $D_{\mathrm{Res,S}}$ represents the diffusion coefficient measured in the reservoir region of the simulation box including a pore. $\langle D\rangle_{\mathrm{Pore,E}}$ represents the average diffusion coefficient inside the pore calculated according to Eq. (5.2.5). $D_{\mathrm{Pore,S}}$ represents the diffusion coefficient inside the pore calculated according to Eq. (5.2.6). The experimental data are collected from various sources representing different materials with pore diameters mostly around 5 nm and are based on NMR measurements. For benzene and water also QENS measurements carried out in materials with smaller diameters are considered. [b]SBA-15, 5 nm pore diameter, $T = 295\,\mathrm{K}$ [66]. [c]MCM-41, 3 nm pore diameter, QENS, $T = 300\,\mathrm{K}$ [90]. [d]SBA-15, 4.9 nm pore diameter, $T = 298\,\mathrm{K}$ [24]. [e]KIT-6, 5.2 nm pore diameter, $T = 298\,\mathrm{K}$ [24]. [f]Commercial sample, 5-6 nm pore diameter, $T = 298\,\mathrm{K}$ [26]. [g]MCM-41, 3.8 nm pore diameter, QENS, 300 K [91].

5.3.3. Amorphous Pore Structure

To study the influence of an amorphous parent structure relative to a crystalline three alkanes were simulated in the pore carved out from the amorphous silica sample provided by Vink and Barkema [33]. Figure 5.3.7 shows that the density profiles in the crystalline pore have slightly higher peaks. From the radial and axial diffusion profiles in Figure 5.3.8 it appears that in the amorphous pore the self-diffusion is slightly smaller than in the crystalline pore. In Table 5.3.4 the average diffusion coefficients in z-direction are compared. The slightly smaller values in the amorphous pore lead to slightly higher diffusion coefficient ratios around 2.5. However, it can be concluded that the nature of the parent material is of less importance for these probe molecules.

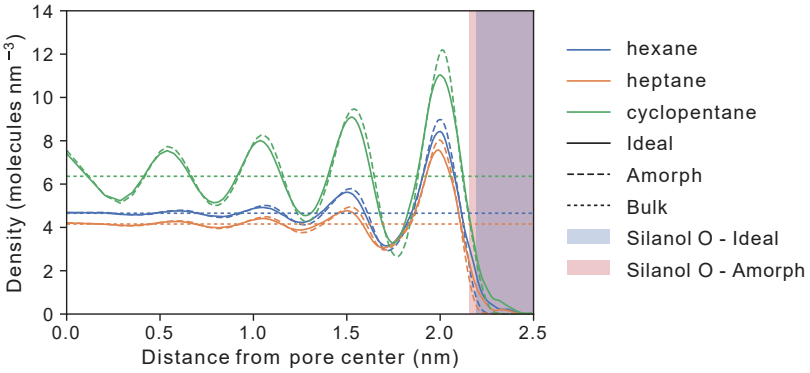

Figure 5.3.7.: Comparison of radial density profiles of selected alkanes confined in pores carved out from amorphous (solid lines) and crystalline (dashed lines) silica. The dotted lines refer to the respective bulk values. The shaded areas denote the configurational space of the silanol oxygen atoms.

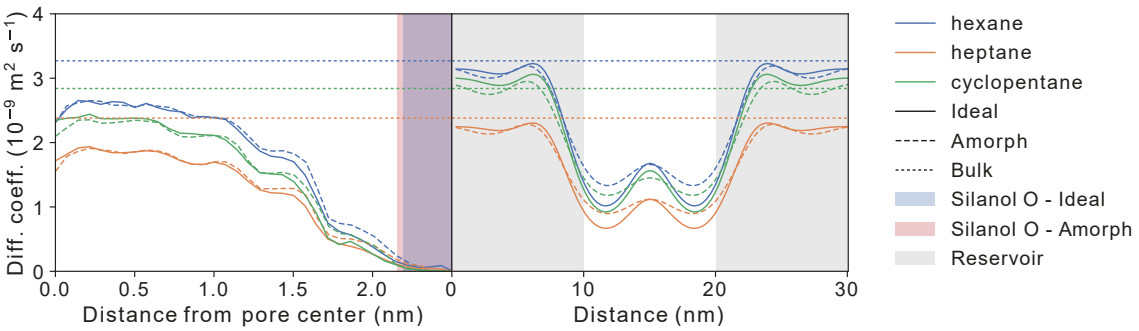

Figure 5.3.8.: Comparison of diffusion profile of selected alkanes confined in pores carved out from amorphous (solid lines) and crystalline (dashed lines) silica: (a) radial diffusion profiles calculated using the Einstein method and (b) diffusion profiles along the simulation box determined by the Smoluchowski method. The dotted lines refer to the respective bulk values. In the first panel, the shaded areas denote the configurational space of the silanol oxygen atoms. In the second panel the shaded areas denote the reservoir regions.

Table 5.3.4.: Simulated Self-Diffusion coefficients ($10^{-9}\,m^2\,s^{-1}$) in two Pore Environments at 295 K.[a]

	Hexane		Heptane		Cyclopentane	
Property	Ideal	Amorph	Ideal	Amorph	Ideal	Amorph
$D_{\mathrm{Res,S}}$	3.08	3.13	2.19	2.23	2.83	2.96
$\langle D\rangle_{\mathrm{Pore,E}}$	1.45	1.31	1.01	0.92	1.20	1.12
$D_{\mathrm{Pore,S}}$	1.47	1.28	0.99	0.85	1.29	1.18
$\left(\frac{D_{\mathrm{Res}}}{D_{\mathrm{Pore}}}\right)_{\mathrm{S}}$	2.10	2.45	2.21	2.62	2.19	2.51

[a]See caption of table 5.3.3 for the definition of the different diffusion coefficients.

5.4. Conclusion and Outlook

The main purpose of the present study was to establish a robust computational protocol that allows the calculation of the ratio between a self-diffusion coefficient in the bulk phase and its counterpart in porous confinement, often used as proxy for the tortuosity of porous materials. The first approach was based on a local evaluation of the mean squared displacement to obtain a radially resolved axial diffusion coefficient in the pore. The second approach was based on Bayesian analysis of the molecular dynamics trajectory [37, 38]. In this approach the observed motion along the pore axis is compared to the motion expected from diffusive dynamics modelled by the Smoluchowski equation. The discretization of the latter then leads to a system of rate equations which enter into a likelihood expression optimized by a Monte Carlo algorithm in the space of model parameters for describing diffusion and free-energy profiles. While both methods were in good agreement with each other, advantages of the latter approach are the use of all data generated within the MD simulation and the seamless evaluation of the diffusion profile also in inhomogeneous regions of the simulation system. For the solvents studied, the diffusion coefficient ratios are between two and three and do not include any geometrical component because straight cylindrical pores were employed. Instead, only the interactions of the molecules with the pore surface are included as well as the influence of the perturbed fluid structure in the confined environment. Unfortunately, a large variation of this diffusion coefficient ratio is present in the experimental literature. Given the importance of understanding confinement effects to aid the rational design of heterogeneously catalyzed reacting systems molecular dynamics simulations in conjunction with experimental techniques such as neutron scattering of nuclear magnetic resonance are expected to become a useful tool to shed further light on the structure and dynamics of confined fluids.

References

[1] L. J. Zielinski et al. “Characterization of coupled pore systems from the diffusion eigenspectrum”. In: J. Chem. Phys. 117.11 (2002), pp. 5361–5365. DOI: 10.1063/1.1499956.

[2] N. Trebel, A. Höltzel, and U. Tallarek. “Confinement Effects on Distribution and Transport of Neutral Solutes in a Small Hydrophobic Nanopore”. In: J. Phys. Chem. B 126.39 (2022), pp. 7781–7795. DOI: 10.1021/acs.jpcb.2c04924.

[3] C. B. Contreras, O. Azzaroni, and G. J. Soler-Illia. “1.16 - Use of Confinement Effects in Mesoporous Materials to Build Tailored Nanoarchitectures”. In: Comprehensive Nanoscience and Nanotechnology. Ed. by D. L. Andrews, R. H. Lipson, and T. Nann. 2nd. Oxford: Academic Press, 2019, pp. 331–348. ISBN: 978-0-12-812296-9. DOI: 10.1016/B978-0-12-803581-8.10420-5.

[4] F. Zaera. “Designing Sites in Heterogeneous Catalysis: Are We Reaching Selectivities Competitive With Those of Homogeneous Catalysts?” In: Chem. Rev. 122.9 (2022), pp. 8594–8757. DOI: 10.1021/acs.chemrev.1c00905.

[5] U. Tallarek, D. Hlushkou, and A. Höltzel. “Solute Sorption, Diffusion, and Advection in Macro-Mesoporous Materials: toward a Realistic Bottom-Up Simulation Strategy”. In: J. Phys. Chem. C 126.5 (2022), pp. 2336–2348. DOI: 10.1021/acs.jpcc.1c10137.

[6] C. Li et al. “Trans-level multi-scale simulation of porous catalytic systems: Bridging reaction kinetics and reactor performance”. In: Chem. Eng. J. 455 (2023), p. 140745. ISSN: 1385-8947. DOI: 10.1016/j.cej.2022.140745.

[7] J. Kärger, D. M. Ruthven, and R. Valiullin. “Diffusion Research with Nanoporous Material - More Than Just a Random Walk?” In: Chem. Int. 43.3 (2021), pp. 25–29. DOI: 10.1515/ci-2021-0307.

[8] J. Kärger and D. M. Ruthven. “Diffusion in zeolites. Comparison of sorption and nuclear magnetic resonance diffusivities”. In: J. Chem. Soc. Farad. T. 1 77.7 (1981), p. 1485. DOI: 10.1039/f19817701485.

[9] J. Kärger. “Measurement of diffusion in zeolites — A never ending challenge?” In: Adsorption 9.1 (2003), pp. 29–35. DOI: 10.1023/A:1023811229823.

[10] O. Talu, M. S. Sun, and D. B. Shah. “Diffusivities ofn-alkanes in silicalite by steady-state single-crystal membrane technique”. In: AIChE J. 44.3 (1998), pp. 681–694. DOI: 10.1002/aic.690440316.

[11] J. Kärger and R. Valiullin. “Mass transfer in mesoporous materials: the benefit of microscopic diffusion measurement”. In: Chem. Soc. Rev. 42 (2013), pp. 4172–4197. DOI: 10.1039/C3CS35326E.

[12] E. Beerdsen and B. Smit. “Diffusion in confinement: Agreement between experiments better than expected”. In: J. Phys. Chem. B 110.30 (2006), pp. 14529–14530. DOI: 10.1021/jp062867a. (Visited on 08/18/2022).

[13] M. S. Gruszkiewicz et al. “Direct Measurements of Pore Fluid Density by Vibrating Tube Densimetry”. In: Langmuir 28.11 (2012), pp. 5070–5078. DOI: 10.1021/la204517v.

[14] S. Luo, J. L. Lutkenhaus, and H. Nasrabadi. “Confinement-Induced Supercriticality and Phase Equilibria of Hydrocarbons in Nanopores”. In: Langmuir 32.44 (2016), pp. 11506–11513. DOI: 10.1021/acs.langmuir.6b03177.

[15] A. Wheeler. “Reaction Rates and Selectivity in Catalyst Pores”. In: Advances in Catalysis. Ed. by W. Frankenburg et al. Vol. 3. New York, NY: Academic Press, 1951, pp. 249–327. DOI: 10.1016/S0360-0564(08)60109-1.

[16] F. A. L. Dullien. Porous Media: fluid Transport and Pore Structure. Second edition. New York, NY: Acedemic Press, 1979. ISBN: 9780323139335.

[17] C. J. Gommes et al. “Practical methods for measuring the tortuosity of porous materials from binary or gray-tone tomographic reconstructions”. In: AIChE J. 55.8 (2009), pp. 2000–2012. DOI: 10.1002/aic.11812.

[18] C. D’Agostino et al. “Hydrogen bonding network disruption in mesoporous catalyst supports probed by PFG-NMR diffusometry and NMR relaxometry”. In: J. Phys. Chem C 116.16 (2012), pp. 8975–8982. DOI: 10.1021/jp2123295.

[19] N. Robinson and C. D’Agostino. “NMR investigation into the influence of surface interactions on liquid diffusion in a mesoporous catalyst support”. In: Top. Catal. 63.3-4 (2020), pp. 319–327. DOI: 10.1007/s11244-019-01209-7. (Visited on 08/18/2022).

[20] B. C. Bukowski et al. “Connecting theory and simulation with experiment for the study of diffusion in nanoporous solids”. In: Adsorption 27.5 (2021), pp. 683–760. DOI: 10.1007/s10450-021-00314-y.

[21] C. N. Satterfield. Mass Transfer in Heterogeneous Catalysis. Cambridge: MIT Press, 1970.

[22] D. C. Martínez Casillas et al. “Diffusion of Water and Electrolytes in Mesoporous Silica with a Wide Range of Pore Sizes”. In: J. Phys. Chem. C 122.6 (2018), pp. 3638–3647. DOI: 10.1021/acs.jpcc.7b11555.

[23] F. L. E. Usseglio-Viretta et al. “Quantitative Relationships Between Pore Tortuosity, Pore Topology, and Solid Particle Morphology Using a Novel Discrete Particle Size Algorithm”. In: J. Electrochem. Soc. 167.10 (2020), p. 100513. DOI: 10.1149/1945-7111/ab913b.

[24] T. J. Rottreau et al. “Diffusion NMR characterization of catalytic silica supports: A tortuous path”. In: J. Phys. Chem. C 121.30 (2017), pp. 16250–16256. DOI: 10.1021/acs.jpcc.7b02929. (Visited on 08/18/2022).

[25] I. J. Chevallier-Boutell et al. “Non-negligible interactions of alkanes with silica mesopores affect self-diffusivity: Insights from first-principles calculations”. In: Microporous Mesoporous Mater 326 (2021), p. 111315. DOI: 10.1016/j.micromeso.2021.111315.

[26] L. G. Linck et al. “Limits imposed by liquid/surface interactions in the determination of tortuosity in mesopores”. In: Microporous Mesoporous Mater 305 (2020), p. 110351. DOI: 10.1016/j.micromeso.2020.110351.

[27] L. Shen and Z. Chen. “Critical review of the impact of tortuosity on diffusion”. In: Chem. Eng. Sci. 62.14 (2007), pp. 3748–3755. DOI: 10.1016/j.ces.2007.03.041.

[28] H. Kraus et al. “PoreMS: a software tool for generating silica pore models with user-defined surface functionalisation and pore dimensions”. In: Mol. Simul. 47.4 (2021), pp. 306–316. DOI: 10.1080/08927022.2020.1871478.

[29] H. Kraus and N. Hansen. PoreMS: 0.2.5. Version v0.2.5. 2021. DOI: 10.5281/zenodo.5803017.

[30] L. Zhuravlev. “The surface chemistry of amorphous silica. Zhuravlev model”. In: Colloids Surf. A Physicochem. Eng. Aspects 173.1 (2000), pp. 1–38. DOI: 10.1016/S0927-7757(00)00556-2.

[31] M. Ide et al. “Quantification of silanol sites for the most common mesoporous ordered silicas and organosilicas: Total versus accessible silanols”. In: Phys. Chem. Chem. Phys. 15.2 (2013), pp. 642–650. DOI: 10.1039/C2CP42811C.

[32] P. N. Wimalasiri et al. “Amorphous Silica Slab Models with Variable Surface Roughness and Silanol Density for Use in Simulations of Dynamics and Catalysis”. In: J. Phys. Chem. C 125.42 (2021), pp. 23418–23434. DOI: 10.1021/acs.jpcc.1c06580.

[33] R. L. C. Vink and G. T. Barkema. “Large well-relaxed models of vitreous silica, coordination numbers, and entropy”. In: Phys. Rev. B 67.24 (2003), p. 245201. DOI: 10.1103/PhysRevB.67.245201.

[34] H. Kraus, M. Högler, and N. Hansen. PoreAna: 0.2.3. Version v0.2.3. 2021. DOI: 10.5281/zenodo.5959496.

[35] M. P. Allen and D. J. Tildesley. Computer simulation of liquids. Second edition. Oxford, United Kingdom: Oxford University Press, 2017. ISBN: 9780198803195 9780198803201.

[36] I.-C. Yeh and G. Hummer. “System-Size dependence of diffusion coefficients and viscosities from molecular dynamics simulations with periodic boundary conditions”. In: J. Phys. Chem. B 108.40 (2004), pp. 15873–15879. DOI: 10.1021/jp0477147.

[37] G. Hummer. “Position-dependent diffusion coefficients and free energies from Bayesian analysis of equilibrium and replica molecular dynamics simulations”. In: New J. Phys. 7 (2005), p. 34. DOI: 10.1088/1367-2630/7/1/034.

[38] A. Ghysels et al. “Position-Dependent Diffusion Tensors in Anisotropic Media from Simulation: oxygen Transport in and through Membranes”. In: J. Chem. Theory Comput. 13.6 (2017), pp. 2962–2976. DOI: 10.1021/acs.jctc.7b00039.

[39] M. V. Smoluchowski. “Über Brownsche Molekularbewegung unter Einwirkung äußerer Kräfte und deren Zusammenhang mit der verallgemeinerten Diffusionsgleichung”. In: Ann. Phys. 353.24 (1916), pp. 1103–1112. DOI: 10.1002/andp.19163532408.

[40] A. Krämer et al. “Membrane permeability of small molecules from unbiased molecular dynamics simulations”. In: J. Chem. Phys. 153.12 (2020), p. 124107. DOI: 10.1063/5.0013429.

[41] C. J. Fennell, K. L. Wymer, and D. L. Mobley. “A fixed-charge model for alcohol polarization in the condensed phase, and its role in small molecule hydration”. In: J. Phys. Chem. B 118.24 (2014), pp. 6438–6446. DOI: 10.1021/jp411529h.

[42] A. M. Nikitin, Y. V. Milchevskiy, and A. P. Lyubartsev. “A new AMBER-compatible force field parameter set for alkanes”. In: J. Mol. Model. 20.3 (2014), p. 2143. DOI: 10.1007/s00894-014-2143-6.

[43] J. Wang et al. “Development and testing of a general amber force field”. In: J. Comput. Chem. 25.9 (2004), pp. 1157–1174. DOI: 10.1002/jcc.20035.

[44] D. L. Mobley et al. MobleyLab/FreeSolv: Version 0.52. Version v0.52. 2018. DOI: 10.5281/zenodo.1161245.

[45] J. L. F. Abascal and C. Vega. “A general purpose model for the condensed phases of water: TIP4P/2005”. In: J. Chem. Phys. 123.23 (2005), p. 234505. DOI: 10.1063/1.2121687.

[46] S. Girard and F. Müller-Plathe. “Molecular dynamics simulation of liquid tetrahydrofuran: on the uniqueness of force fields”. In: Mol. Phys. 101.6 (2003), pp. 779–787. DOI: 10.1080/0026897021000054817.

[47] Dortmund Data Bank. www.ddbst.com. 2018.

[48] F. Chen et al. “Density, viscosity, speed of sound, excess property and bulk modulus of binary mixtures of γ-butyrolactone with acetonitrile, dimethyl carbonate, and tetrahydrofuran at temperatures (293.15 to 333.15) K”. In: J. Mol. Liq. 209 (2015), pp. 683–692. DOI: 10.1016/j.molliq.2015.06.041.

[49] B. Coasne and J. T. Fourkas. “Structure and Dynamics of Benzene Confined in Silica Nanopores”. In: J. Phys. Chem. C 115.31 (2011), pp. 15471–15479. DOI: 10.1021/jp203831q. (Visited on 06/14/2021).

[50] T. S. Gulmen and W. H. Thompson. “Testing a Two-State Model of Nanoconfined Liquids: conformational Equilibrium of Ethylene Glycol in Amorphous Silica Pores”. In: Langmuir 22.26 (2006), pp. 10919–10923. DOI: 10.1021/la062285k.

[51] F. Ziegler et al. “Confinement Effects for Efficient Macrocyclization Reactions with Supported Cationic Molybdenum Imido Alkylidene *N*-Heterocyclic Carbene Complexes”. In: ACS Catal. 11.18 (2021), pp. 11570–11578. DOI: 10.1021/acscatal.1c03057.

[52] A. Butenuth et al. “Ab initio derived force-field parameters for molecular dynamics simulations of deprotonated amorphous-SiO2/water interfaces”. In: Phys. Status Solidi. B 249.2 (2012), pp. 292–305. DOI: 10.1002/pssb.201100786.

[53] F. Ziegler et al. “Olefin Metathesis in Confined Geometries: a Biomimetic Approach toward Selective Macrocyclization”. In: J. Am. Chem. Soc. 141.48 (2019), pp. 19014–19022. DOI: 10.1021/jacs.9b08776.

[54] H. Kraus and N. Hansen. “An atomistic view on the uptake of aromatic compounds by cyclodextrin immobilized on mesoporous silica”. In: Adsorption 28 (2022), pp. 125–136. DOI: 10.1007/s10450-022-00356-w.

[55] H. Kraus and N. Hansen. PoreSim: 0.1.1. Version v0.1.1. 2021. DOI: 10.5281/zenodo.5993763.

[56] M. J. Abraham et al. “GROMACS: high performance molecular simulations through multi-level parallelism from laptops to supercomputers”. In: SoftwareX 1-2 (2015), pp. 19–25. DOI: 10.1016/j.softx.2015.06.001.

[57] B. Hess et al. “GROMACS 4: algorithms for Highly Efficient, Load-Balanced, and Scalable Molecular Simulation”. In: J. Chem. Theory. Comput. 4.3 (2008), pp. 435–447. DOI: 10.1021/ct700301q.

[58] S. Nosé. “A molecular dynamics method for simulations in the canonical ensemble”. In: Mol. Phys. 52.2 (1984), pp. 255–268. DOI: 10.1080/00268978400101201.

[59] W. G. Hoover. “Canonical dynamics: equilibrium phase-space distributions”. In: Phys. Rev. A 31.3 (1985), pp. 1695–1697. DOI: 10.1103/physreva.31.1695.

[60] M. Parrinello and A. Rahman. “Crystal Structure and Pair Potentials: a Molecular-Dynamics Study”. In: Phys. Rev. Lett. 45.14 (1980), pp. 1196–1199. DOI: 10.1103/physrevlett.45.1196.

[61] M. Parrinello and A. Rahman. “Polymorphic transitions in single crystals: a new molecular dynamics method”. In: J. Appl. Phys. 52.12 (1981), pp. 7182–7190. DOI: 10.1063/1.328693.

[62] B. Hess et al. “LINCS: a linear constraint solver for molecular simulations”. In: J. Comp. Chem. 18.12 (1997), pp. 1463–1472. DOI: 10.1002/(sici)1096-987x(199709)18:12<1463::aid-jcc4>3.0.co;2-h.

[63] B. Hess. “P-LINCS: a Parallel Linear Constraint Solver for Molecular Simulation”. In: J. Chem. Theory Comput. 4.1 (2008), pp. 116–122. DOI: 10.1021/ct700200b.

[64] T. Darden, D. York, and L. Pedersen. “Particle mesh Ewald: An N log(N) method for Ewald sums in large systems”. In: J. Chem. Phys. 98.12 (1993), pp. 10089–10092. DOI: 10.1063/1.464397.

[65] U. Essmann et al. “A smooth particle mesh Ewald method”. In: J. Chem. Phys. 103.19 (1995), pp. 8577–8593. DOI: 10.1063/1.470117.

[66] S. Agrawal, M. Elmehlawy, and M. P. Hoepfner. “Effect of confinement on the density and diffusivity of organic molecules in single-digit nanopores relative to bulk fluid behavior”. In: J. Phys. Chem. C 125.20 (2021), pp. 11097–11106. DOI: 10.1021/acs.jpcc.1c00159.

[67] H. Hiraoka et al. “Self-diffusion of methanol under pressure”. In: Rev. Phys. Chem. Jpn. 28.2 (1958), pp. 61–63.

[68] M. Holz et al. “Experimental study of dynamic isotope effects in molecular liquids: detection of translation-rotation coupling”. In: J. Chem. Phys. 104.2 (1996), pp. 669–679. DOI: 10.1063/1.470863.

[69] J. R. Partington, R. F. Hudson, and K. W. Bagnall. “Self-diffusion of aliphatic alcohols”. In: Nature 169.4301 (1952), pp. 583–584. DOI: 10.1038/169583a0.

[70] W. S. Price, H. Ide, and Y. Arata. “Solution dynamics in aqueous monohydric alcohol systems”. In: J. Phys. Chem. A 107.24 (2003), pp. 4784–4789. DOI: 10.1021/jp027257z.

[71] R. E. Rathbun and A. L. Babb. “Self-diffusion in liquids. III. temperature dependence in pure liquids”. en. In: J. Phys. Chem. 65.6 (1961), pp. 1072–1074. DOI: 10.1021/j100824a520.

[72] K. Graupner and E. R. S. Winter. “Some measurements of the self-diffusion coefficients of liquids”. In: J. Chem. Soc. 0 (1952), pp. 1145–1150. DOI: 10.1039/JR9520001145. (Visited on 10/08/2021).

[73] P. S. Tofts et al. “Test liquids for quantitative MRI measurements of self-diffusion coefficient in vivo”. In: Magn. Reson. Med. 43.3 (2000), pp. 368–374. DOI: 10.1002/(SICI)1522-2594(200003)43:3<368::AID-MRM8>3.0.CO;2-B.

[74] A. F. Collings and R. Mills. “Temperature-dependence of self-diffusion for benzene and carbon tetrachloride”. In: T. Faraday Soc. 66 (1970), p. 2761. DOI: 10.1039/tf9706602761.

[75] D. Collins and H. Watts. “Viscosity and self-diffusion in benzene-cyclohexane mixtures”. In: Aust. J. Chem. 17.5 (1964), p. 516. DOI: 10.1071/CH9640516.

[76] H. Hiraoka, J. Osugi, and W. Jono. “Self-diffusion of benzene and diffusions of sulfur and iodine in benzene under pressure”. In: Rev. Phys. Chem. Jpn. 28.2 (1958), pp. 52–60.

[77] M. A. McCool, A. F. Collings, and L. A. Woolf. “Pressure and temperature dependence of the self-diffusion of benzene”. In: J. Chem. Soc. 68.0 (1972), p. 1489. DOI: 10.1039/f19726801489.

[78] N. K. Gaisin. “Investigation of molecular motion in liquid toluene by the spin echo method on deuterated samples”. In: J. Struct. Chem+ 12.6 (1972), pp. 899–906. DOI: 10.1007/BF00744152.

[79] O. Suárez-Iglesias et al. “Self-Diffusion in Molecular Fluids and Noble Gases: Available Data”. In: J. Chem. Eng. Data 60.10 (2015), pp. 2757–2817. DOI: 10.1021/acs.jced.5b00323.

[80] K. R. Harris. “Temperature and density dependence of the self-diffusion coefficient of n-hexane from 223 to 333 K and up to 400 MPa”. In: J. Chem. Soc. 78.7 (1982), p. 2265. DOI: 10.1039/f19827802265.

[81] J. W. Moore and R. M. Wellek. “Diffusion coefficients of n-heptane and n-decane in n-alkanes and n-alcohols at several temperatures”. In: J. Chem. Eng. Data 19.2 (1974), pp. 136–140. DOI: 10.1021/je60061a023.

[82] L. Devell et al. “Measurements of the self-diffusion of water in pure water, H2O-D2O mixtures and solutions of electrolytes.” In: Acta Chem. Scand. 16 (1962), pp. 2177–2188. DOI: 10.3891/acta.chem.scand.16-2177.

[83] K. Tanaka. “Measurements of self-diffusion coefficients of water in pure water and in aqueous electrolyte solutions”. In: J. Chem. Soc. Farad. T. 1 71.0 (1975), p. 1127. DOI: 10.1039/f19757101127.

[84] J. H. Wang. “Self-Diffusion Coefficients of Water”. In: J. Phys. Chem. US 69.12 (1965), pp. 4412–4412. DOI: 10.1021/j100782a510.

[85] I. C. Bourg and C. I. Steefel. “Molecular Dynamics Simulations of Water Structure and Diffusion in Silica Nanopores”. In: J. Phys. Chem. C 116 (2012), pp. 11556–11564. DOI: 0.1021/jp301299a.

[86] H. Thompson et al. “The Three-Dimensional Structure of Water Confined in Nanoporous Vycor Glass”. In: J. Phys. Chem. B 111.20 (2007), pp. 5610–5620. DOI: 10 . 1021 / jp0677905.

[87] A. Lerbret et al. “Water Confined in Cylindrical Pores: A Molecular Dynamics Study”. In: Food Biophys. 6 (2011), pp. 233–240. DOI: 10.1007/s11483-010-9191-y.

[88] A. A. Milischuk and B. M. Ladanyi. “Structure and dynamics of water confined in silica nanopores”. In: J. Chem. Phys. 135.17 (2011), p. 174709. DOI: 10.1063/1.3657408.

[89] M. Vögele and G. Hummer. “Divergent Diffusion Coefficients in Simulations of Fluids and Lipid Membranes”. In: J. Phys. Chem. B 120.33 (2016), pp. 8722–8732. DOI: 10.1021/acs.jpcb.6b05102.

[90] D. Dervin et al. “Probing the dynamics and structure of confined benzene in MCM-41 based catalysts”. In: Phys. Chem. Chem. Phys. 22.20 (2020), pp. 11485–11489. DOI: 10.1039/D0CP01196G. (Visited on 12/29/2022).

[91] A. Jani et al. “Dynamics of water confined in mesopores with variable surface interaction”. In: J. Chem. Phys. 154.9 (2021), p. 094505. DOI: 10.1063/5.0040705.

6. Conclusion and Outlook

By means of molecular simulations the gap between experiment and theory can be bridged. They play a valuable role in providing essentially exact results for problems in statistical mechanics which would otherwise only be soluble by approximate methods or might be even intractable. Molecular simulations have a long history in studies of fluid properties under confinement [1, 2], resulting in the explanation of observed phenomena such as the freezing of mixtures confined in silica nanopores [3] or the description of new phenomena such as rather high tangential pressures in confinement [4]. While such discover-driven activities help to obtain a deeper understanding of the behavior of fluids in mesoporous confinement, a gap exists in the field of data-driven projects which aim at high accuracy prediction of properties without or with little input from experiment. The existence of this gap is related to challenges in the validation of molecular simulations of complex systems [5] but also to the assumptions and approximations used in classical molecular simulations [6]. Both issues are related for confined fluids in mesoporous materials because experimental data are scarce. Therefore, the validation is often of indirect nature such that the effect of assumptions and approximations cannot be thoroughly tested.

The present work contributes to the effort of providing simulation tools for the prediction of physical properties of confined fluids relevant for liquid phase processes in mesoporous confinement as well as to showcase the challenges associated with the comparison of experiment and simulation even for supposedly simple properties such as self-diffusion coefficient and mean fluid density. In chapter 2 the open-source software tool PoreMS was introduced to facilitate rapid model building of functionalized silica pores for Monte Carlo or molecular dynamics simulation studies of confinement effects in applications relying on mesoporous silica. The introduction of PoreMS should stimulate systematic molecular simulations research on confinement effects in functionalized silica pores, as at present experimental advances relying on functionalized mesoporous silica materials are still largely empirically driven due to the lack of molecular-level information. In chapter 3, PoreMS was complemented by two additional program packages for preparing MD simulations of porous materials with GROMACS, PoreSim, and for analyzing the simulation trajectories, PoreAna, the latter providing results such as density and diffusion profiles, thereby reducing the overhead for system preparation to analysis. The selected case study of adsorption of aromatic molecules in cyclodextrin-functionalized silica mesopores shows that current moderate computational resources allow an atomistically resolved model (~ 65 000 atoms) to be propagated to the µs time scale and allows insight into the uptake process of solutes from an aqueous solution. Chapter 4 is concerned with studying the influence of the inner pore surface composition and the silanol force field parameters on radial density profiles. Moreover, the discretized Smoluchowski equation was implemented allowing diffusion profiles to be calculated along the z-axis of the simulation box. Finally, in chapter 5, the developed tool box was applied to study density and self-diffusion of 14 solvents inside a 5 nm silica mesopore.

Current challenges regarding the comparison of simulation and experiments are highlighted and different simulation protocols are discussed with respect to the occurrence of simulation artefacts and finite-size effects. In future work the molecular picture for reactant-solvent, reactant-surface, reactant-catalyst interactions at the single-pore level should be coupled with hierarchical transport analysis through realistic pore networks (3D physical reconstructions) and the model be expanded to a generalized reaction-transport scheme under spatial confinement. With the aid of computer simulations, macroscopic behavior can then be decomposed into intrinsic reactivity and adsorption/transport processes.

References

[1] S. Jiang and C. Hall. "Preface to the Tribute to Keith E. Gubbins, Pioneer in the Theory of Liquids Special Issue". In: *Langmuir* 33.42 (2017), pp. 11095–11101. DOI: 10.1021/acs.langmuir.7b03390.

[2] P. T. Cummings et al. "Keith E. Gubbins: a retrospective". In: *AIChE J.* 67.3 (2021). DOI: 10.1002/aic.17191.

[3] B. Coasne et al. "Freezing of mixtures confined in silica nanopores: experiment and molecular simulation". In: *J. Chem. Phys.* 133.8 (2010), p. 084701. DOI: 10.1063/1.3464279.

[4] K. E. Gubbins, Y. Long, and M. Sliwinska-Bartkowiak. "Thermodynamics of confined nano-phases". In: *J. Chem. Thermodyn.* 74 (2014), pp. 169–183. DOI: 10.1016/j.jct.2014.01.024.

[5] W. F. van Gunsteren et al. "Validation of Molecular Simulation: an Overview of Issues". In: *Angew. Chem. Int. Ed.* 57.4 (2018), pp. 884–902. DOI: 10.1002/anie.201702945.

[6] W. F. Gunsteren et al. "On the Effect of the Various Assumptions and Approximations used in Molecular Simulations on the Properties of Bio-Molecular Systems: overview and Perspective on Issues". In: *ChemPhysChem* 22.3 (2021), pp. 264–282. DOI: 10.1002/cphc.202000968.

A. Appendix

A.1. PoreMS: A software tool for generating silica pore models with user-defined surface functionalization and pore dimensions

Jupyter notebooks and necessary structure files for pore generation are provided via the Data Repository of the University of Stuttgart (DaRUS) under

`https://doi.org/10.18419/darus-1170`.

A.1.1. Calculating pore properties

The pore diameter is obtained as

$$d = \frac{2}{M} \sum_{i=1}^{M} s_i \tag{A.1.1}$$

where s_i denotes the shortest distance between a surface Si atom $i = 1, \ldots, M$ and the central axis of the pore. The pore surface roughness is calculated as standard deviation of these distances,

$$R_\mathrm{s} = \sqrt{\frac{1}{M} \sum_{i=1}^{M} \left\| s_i - \frac{d}{2} \right\|^2}. \tag{A.1.2}$$

The interior pore volume is calculated as

$$V_\mathrm{p} = \frac{\pi}{4} d^2 \cdot l \tag{A.1.3}$$

where l denotes the length of the pore. The interior surface area is obtained from

$$A_\mathrm{s,int} = \pi \cdot d \cdot l \tag{A.1.4}$$

while the exterior surface is calculated as

$$A_\mathrm{s,ext} = x \cdot y - \frac{\pi}{4} d^2 \tag{A.1.5}$$

where x and y denote the dimensions of the silica block in the respective directions.

A.1.2. Generating a catalytic pore using PoreMS version 0.2.0

This notebook illustrates how to create the described catalytic cylindric pore and functionalise the surface according to PoreMS version 0.2.0 which can be installed via

```
pip install porems==0.2.0
```

Alternatively, the development version can be installed directly from GitHub. Import the PoreMS package using

```
import porems as pms
```

Surface Molecules

Before generating the pore system, we will first create the molecules that are going to be attached on the interior and exterior pore surfaces.

The catalytic pore consists of three different types of molecules

- Catalyst - Interior surface
- Dimethoxydimethylsilyl (DMDMS) - Interior surface
- Trimethylsilyl (TMS) - Exterior surface

Structures and topologies are available on the corresponding darus repository of Ziegler et al. (2019).

To generate the molecules in the PoreMS needed format, the *Molecule* class will be utilized. In the following we will present three possible ways to create the molecule objects.

Importing Predefined Molecules

Trimethylsilyl or for short **TMS** is provided in the PoreMS package as a generic molecule and can be simply imported

```
tms = pms.gen.tms()
```

For easy access of the atom data, a representation function has been implemented. Therefore, molecules can be simply printed

```
display(tms)
```

	Residue	Name	Type	x	y	z
0	0		Si	8.702925e-02	0.150739	0.000000
1	0		O	8.702925e-02	0.150739	0.155000
2	0		Si	8.702925e-02	0.150739	0.310000
3	0		C	2.065877e-01	0.150739	0.452484
4	0		C	2.725000e-02	0.254280	0.452484
5	0		C	2.725000e-02	0.047198	0.452484
6	0		H	2.610877e-01	0.150739	0.546881
7	0		H	1.793377e-01	0.197937	0.546881
8	0		H	1.793377e-01	0.103541	0.546881
9	0		H	8.175000e-02	0.254280	0.546881
10	0		H	1.249001e-16	0.301478	0.546881

```
11          0          H   8.326673e-17   0.207081   0.546881
12          0          H   8.175000e-02   0.047198   0.546881
13          0          H   4.163336e-17   0.094397   0.546881
14          0          H   0.000000e+00   0.000000   0.546881
```

Additionally using the *Store* module, molecule objects can be converted to structure files

```
pms.Store(tms, "output/").gro()
pms.Store(tms, "output/").pdb()
```

Importing Structure Files

The **catalyst** molecule can be constructed by using a structural file as an input. Herefore, the structure file **catabm.gro** provided in the mentioned repository will be used.

```
catalyst = pms.Molecule("catalyst", "CAT", "catabm.gro")
```

Construct new molecule from scratch

Dimethoxydimethylsilyl or for short **DMDMS** will be constructed from scratch to present the functionalities of the *Molecule* module.

First, we initialize an empty molecule with a file name and short name

```
dmdms = pms.Molecule("dmdms", "DMS")
```

Atoms can be added to the molecule using the provided *add* function where atoms can be placed in the 3D-space using cartesian or spherical coordinates. We first define A dictionary containing bond lengths

```
b = {"sio": 0.155, "sic": 0.186, "ch": 0.109 ,"co": 0.123}
```

The starting atom of the molecule will be placed using cartesian coordinates of the origin point

```
dmdms.add("Si", [0, 0, 0])
```

Based on the first atom which has index **0**, the other atoms will be placed using spherical coordinates

```
dmdms.add("O", 0, r=b["sio"])
dmdms.add("Si", 1, r=b["sio"])

for i in range(3):
    if i == 0:
        dmdms.add("O", 2, r=b["sio"], theta=50, phi=120*i)
    else:
        dmdms.add("C", 2, r=b["sic"], theta=50, phi=120*i)

dmdms.add("C", 3, r=b["co"])
```

Finally, Hydrogens will be added

```
for i in range(4, 6+1):
    for j in range(3):
        dmdms.add("H", i, r=b["ch"], theta=30, phi=120*j)
```

Note that the order in which atoms are added, will be the order in the structure file.

Generate and Functionalise a Pore System

An empty pore is generated by initializing a new object with the desired properties

```
pore = pms.PoreCylinder([8, 8, 10], 4.8, 5.5)
```

Since the functionalisation is done iteratively, special placement, and molecules with a lower concentration on the surface have should be prioritized. The catalyst molecules are placed far enough apart so they do not interact or influence each other. Therefore, a point symmetrical placement is chosen, for which a special attachment function is used

```
pore.attach_special(mol=catalyst, mount=37, axis=[34, 22], amount=2,␣
 ↪symmetry="point", scale=0.8)
```

The *mount* atom id entry defines the Si atom which will be placed on the surface, whereas atom ids in the *axis* list define the main axis of the molecule which should be oriented perpendicular to the surface. The remaining two molecules **TMS** and **DMDMS** will be attached using the conventional attachment function

```
pore.attach(mol=dmdms, mount=0, axis=[1, 2], amount=5.54, site_type="in",␣
 ↪inp="molar", scale=0.4)
pore.attach(mol=tms,   mount=0, axis=[1, 2], amount=4.48, site_type="ex",␣
 ↪inp="molar", scale=0.4)
```

After finishing the surface functionalisation, the pore needs to be finalized, which fills empty binding sites with silanol groups creating the final structure

```
pore.finalize()
```

In order to show the properties of the generated pore, use the table function. This returns a dictionary of pandas data frames for pore properties **props**, allocation **alloc** and a table with all pore and allocation properties combined in a single **full** table.

```
display(pore.table(decimals=5)["full"])
```

```
                                          Interior  \
Silica block xyz-dimensions (nm)
Simulation box xyz-dimensions (nm)
Pore drilling direction                          z
Pore diameter (nm)                         4.80458
Surface roughness (nm)                     0.07988
Solvent reservoir z-dimension (nm)
Pore volume (nm^3)                       182.66136
Solvent reservoir volume (nm^3)
Surface area (nm^2)                      152.07254
```

Surface chemistry - Before Functionalization	
Number of single silanol groups	690
Number of geminal silanol groups	60
Number of siloxane bridges	0
Total number of OH groups	810
Overall hydroxylation (mumol/m^2)	8.84491
Surface chemistry - After Functionalization	
Number of CAT groups	2
CAT density (mumol/m^2)	0.02184
Number of DMS groups	466
DMS density (mumol/m^2)	5.08855
Number of DMSG groups	41
DMSG density (mumol/m^2)	0.44771
Number of TMS groups	0
TMS density (mumol/m^2)	0.00000
Number of TMSG groups	0
TMSG density (mumol/m^2)	0.00000
Bonded-phase density (mumol/m^2)	5.55810
Number of residual OH groups	301
Residual hydroxylation (mumol/m^2)	3.28681

	Exterior
Silica block xyz-dimensions (nm)	[8.09567, 7.89274, 10.07500]
Simulation box xyz-dimensions (nm)	[8.09567, 7.89274, 21.07500]
Pore drilling direction	
Pore diameter (nm)	
Surface roughness (nm)	0.00000
Solvent reservoir z-dimension (nm)	5.50000
Pore volume (nm^3)	
Solvent reservoir volume (nm^3)	2 * 351.43385
Surface area (nm^2)	2 * 45.76690
Surface chemistry - Before Functionalization	
Number of single silanol groups	394
Number of geminal silanol groups	34
Number of siloxane bridges	0
Total number of OH groups	462
Overall hydroxylation (mumol/m^2)	8.38146
Surface chemistry - After Functionalization	
Number of CAT groups	0
CAT density (mumol/m^2)	0.00000
Number of DMS groups	0
DMS density (mumol/m^2)	0.00000
Number of DMSG groups	0
DMSG density (mumol/m^2)	0.00000
Number of TMS groups	227
TMS density (mumol/m^2)	4.11816
Number of TMSG groups	19
TMSG density (mumol/m^2)	0.34469
Bonded-phase density (mumol/m^2)	4.46286

```
Number of residual OH groups                                  216
Residual hydroxylation (mumol/m^2)                        3.91860
```

Note that the molecule name with the added **G** letter stands for the geminal variant of the molecule.

At this point the pore generation is completed and what is left is converting the programs data structure into a readable file-format using the functionalities of the *Store* module. For this a store function is provided that creates a structure file in the GROMACS format, a main topology containing the number of atoms, a topology for the grid (silicon and oxygen) and basic surface groups (single and geminal silanol and siloxane bridges) and a pickle file of the pore object and pore system. The object files can be used to extract pore properties during later analysis

```
pore.store("output/cata/")
```

For additional construction abilities e.g. choosing a different drilling axis or defining a different drilling inclination of the pore shape, we suggest using the delivered constructor classes as templates to construct more complex pore forms.

For further information, more thorough variable descriptions and functionalities like adding siloxane bridges for adjusting the hydroxylation degree, we refer to the documentation website of the GitHub repository.

A.1.3. Generating an RPLC pore using PoreMS version 0.2.0

This notebook illustrates how to create the described RPLC pore and functionalise the surface according to PoreMS version 0.2.0 which can be installed via

```
pip install porems==0.2.0
```

Alternatively, the development version can be installed directly from GitHub. Import the PoreMS package using

```
import porems as pms
```

Surface Molecules

Before generating the pore system, we will first create the molecules that are going to be attached on the interior and exterior pore surfaces.

The catalytic pore consists of three different types of molecules

- Dimethyloctadecylsilane (C18)
- Trimethylsilyl (TMS)

To generate the molecules in the PoreMS needed format, the *Molecule* class will be utilized. In the following we will present two possible ways to create the molecule objects.

Importing Predefined Molecules

Trimethylsilyl or for short **TMS** is provided in the PoreMS package as a generic molecule and can be simply imported. Additionally, if for example a unified atom forcefield is to be utilized, the hydrogen atoms can be removed setting the *is_hydro* flag to *False*

```
tms = pms.gen.tms(is_hydro=False)
```

For easy access of the atom data, a representation function has been implemented. Therefore, molecules can be simply printed

```
display(tms)
```

	Residue	Name	Type	x	y	z
0	0		Si	5.977925e-02	0.103541	0.000000
1	0		O	5.977925e-02	0.103541	0.155000
2	0		Si	5.977925e-02	0.103541	0.310000
3	0		C	1.793377e-01	0.103541	0.452484
4	0		C	8.326673e-17	0.207081	0.452484
5	0		C	0.000000e+00	0.000000	0.452484

Additionally, using the *Store* module, molecule objects can be converted to structure files

```
pms.Store(tms, "output/").gro()
pms.Store(tms, "output/").pdb()
```

Importing Structure Files

The **C18** molecule can be constructed by using a structural file as an input. Herefore, the structure file **c18.gro** is also provided in the supporting information

```
c18 = pms.Molecule("c18", "C18", "c18.gro")
```

Generate and Functionalise a Pore System

In the following the iterative work process of creating the desired RPLC pore will be illustrated.

An empty pore is generated by initializing a new object with the desired properties and finalized with the finalize function.

```
pore = pms.PoreCylinder([16, 16, 10], 9, 5.5)

pore.finalize()
```

To show the properties of the generated pore, use the table function. This returns a dictionary of pandas data frames for pore properties **props**, allocation **alloc** and a table with all pore and allocation properties combined in a single **full** table.

```
display(pore.table(decimals=5)["full"])
```

```
                                          Interior  \
Silica block xyz-dimensions (nm)
Simulation box xyz-dimensions (nm)
Pore drilling direction                          z
Pore diameter (nm)                         9.01719
Surface roughness (nm)                     0.07598
Solvent reservoir z-dimension (nm)
Pore volume (nm^3)                       643.39469
Solvent reservoir volume (nm^3)
Surface area (nm^2)                      285.40803
Surface chemistry - Before Functionalization
    Number of single silanol groups           1234
    Number of geminal silanol groups           177
    Number of siloxane bridges                   0
    Total number of OH groups                 1588
    Overall hydroxylation (mumol/m^2)      9.23940
Surface chemistry - After Functionalization
    Bonded-phase density (mumol/m^2)       0.00000
    Number of residual OH groups              1588
    Residual hydroxylation (mumol/m^2)     9.23940

                                                                  Exterior
Silica block xyz-dimensions (nm)          [16.19167, 15.78574, 10.07500]
Simulation box xyz-dimensions (nm)        [16.19167, 15.78574, 21.07500]
Pore drilling direction
Pore diameter (nm)
Surface roughness (nm)                                            0.00000
Solvent reservoir z-dimension (nm)                                5.50000
```

```
Pore volume (nm^3)
Solvent reservoir volume (nm^3)                          2 * 1405.78671
Surface area (nm^2)                                       2 * 191.73707
Surface chemistry - Before Functionalization
    Number of single silanol groups                                1700
    Number of geminal silanol groups                                 53
    Number of siloxane bridges                                        0
    Total number of OH groups                                      1806
    Overall hydroxylation (mumol/m^2)                           7.82062
Surface chemistry - After Functionalization
    Bonded-phase density (mumol/m^2)                            0.00000
    Number of residual OH groups                                   1806
    Residual hydroxylation (mumol/m^2)                          7.82062
```

In order to be able to better characterize such pores, it is desirable to have the same hydroxylation degree on the interior and exterior surface. The *hydro* parameter in the initialization function defines the wanted hydroxylation degree on the interior (first list entry) and exterior surface (second list entry). The program will then try to achieve this hydroxylation degree by adding randomly distributed siloxane bridges on the surface. If the value is left 0, nothing will be done.

```
pore = pms.PoreCylinder([16, 16, 10], 9, 5.5, hydro=[7.821, 0])

pore.finalize()

display(pore.table(decimals=5)["full"])
```

```
                                          Interior  \
Silica block xyz-dimensions (nm)
Simulation box xyz-dimensions (nm)
Pore drilling direction                          z
Pore diameter (nm)                         9.01568
Surface roughness (nm)                     0.07625
Solvent reservoir z-dimension (nm)
Pore volume (nm^3)                       643.17959
Solvent reservoir volume (nm^3)
Surface area (nm^2)                      285.36032
Surface chemistry - Before Functionalization
    Number of single silanol groups           1054
    Number of geminal silanol groups           145
    Number of siloxane bridges                 122
    Total number of OH groups                 1344
    Overall hydroxylation (mumol/m^2)      7.82105
Surface chemistry - After Functionalization
    Bonded-phase density (mumol/m^2)       0.00000
    Number of residual OH groups              1344
    Residual hydroxylation (mumol/m^2)     7.82105

                                          Exterior
```

```
Silica block xyz-dimensions (nm)              [16.19167, 15.78574, 10.07500]
Simulation box xyz-dimensions (nm)            [16.19167, 15.78574, 21.07500]
Pore drilling direction
Pore diameter (nm)
Surface roughness (nm)                                                0.00000
Solvent reservoir z-dimension (nm)                                    5.50000
Pore volume (nm^3)
Solvent reservoir volume (nm^3)                             2 * 1405.78671
Surface area (nm^2)                                          2 * 191.75842
Surface chemistry - Before Functionalization
    Number of single silanol groups                                    1700
    Number of geminal silanol groups                                     53
    Number of siloxane bridges                                            0
    Total number of OH groups                                          1806
    Overall hydroxylation (mumol/m^2)                               7.81974
Surface chemistry - After Functionalization
    Bonded-phase density (mumol/m^2)                                0.00000
    Number of residual OH groups                                       1806
    Residual hydroxylation (mumol/m^2)                              7.81974
```

Since the functionalisation is done iteratively molecules should be prioritized based on importance. In our case, it is important to achieve the concentration of 2.91 $\frac{\mu\text{mol}}{\text{m}^2}$ of the **C18** chains on the interior and exterior surface

```
pore = pms.PoreCylinder([16, 16, 10], 9, 5.5, hydro=[7.821, 0])

pore.attach(mol=c18, mount=0, axis=[0, 1], amount=2.91, site_type="in",␣
 ↪inp="molar")
pore.attach(mol=c18, mount=0, axis=[0, 1], amount=2.91, site_type="ex",␣
 ↪inp="molar")

pore.finalize()

display(pore.table(decimals=5)["full"])
```

```
                                          Interior  \
Silica block xyz-dimensions (nm)
Simulation box xyz-dimensions (nm)
Pore drilling direction                          z
Pore diameter (nm)                         9.01013
Surface roughness (nm)                     0.07561
Solvent reservoir z-dimension (nm)
Pore volume (nm^3)                       642.38776
Solvent reservoir volume (nm^3)
Surface area (nm^2)                      285.18461
Surface chemistry - Before Functionalization
    Number of single silanol groups           1048
    Number of geminal silanol groups           148
    Number of siloxane bridges                 122
```

```
    Total number of OH groups                    1344
    Overall hydroxylation (mumol/m^2)         7.82587
Surface chemistry - After Functionalization
    Number of C18 groups                          435
    C18 density (mumol/m^2)                   2.53293
    Number of C18G groups                          64
    C18G density (mumol/m^2)                  0.37266
    Bonded-phase density (mumol/m^2)          2.90559
    Number of residual OH groups                  845
    Residual hydroxylation (mumol/m^2)        4.92028
```

```
                                                                  Exterior
Silica block xyz-dimensions (nm)          [16.19167, 15.78574, 10.07500]
Simulation box xyz-dimensions (nm)        [16.19167, 15.78574, 21.07500]
Pore drilling direction
Pore diameter (nm)
Surface roughness (nm)                                            0.00000
Solvent reservoir z-dimension (nm)                                5.50000
Pore volume (nm^3)
Solvent reservoir volume (nm^3)                       2 * 1405.78671
Surface area (nm^2)                                    2 * 191.83701
Surface chemistry - Before Functionalization
    Number of single silanol groups                            1700
    Number of geminal silanol groups                             53
    Number of siloxane bridges                                    0
    Total number of OH groups                                  1806
    Overall hydroxylation (mumol/m^2)                       7.81654
Surface chemistry - After Functionalization
    Number of C18 groups                                        646
    C18 density (mumol/m^2)                                 2.79595
    Number of C18G groups                                        26
    C18G density (mumol/m^2)                                0.11253
    Bonded-phase density (mumol/m^2)                        2.90848
    Number of residual OH groups                                1134
    Residual hydroxylation (mumol/m^2)                      4.90806
```

Note that the molecule name with the added **G** letter stands for the geminal variant of the molecule.

Finally **TMS** is added to the surface so that the bonded phase coverage degree is the same on both surfaces and equal to 46% $\left(3.60\ \frac{\mu\text{mol}}{\text{m}^2}\right)$ of the surface hydroxylation

```
pore = pms.PoreCylinder([16, 16, 10], 9, 5.5, hydro=[7.821, 0])

pore.attach(mol=c18, mount=0, axis=[0, 1], amount=2.91, site_type="in",␣
 ↪inp="molar")
pore.attach(mol=c18, mount=0, axis=[0, 1], amount=2.91, site_type="ex",␣
 ↪inp="molar")
```

```
pore.attach(mol=tms, mount=0, axis=[1, 2], amount=3.60-2.91,␣
 ↪site_type="in", inp="molar")
pore.attach(mol=tms, mount=0, axis=[1, 2], amount=3.60-2.91,␣
 ↪site_type="ex", inp="molar")

pore.finalize()

display(pore.table(decimals=5)["full"])
```

	Interior \
Silica block xyz-dimensions (nm)	
Simulation box xyz-dimensions (nm)	
Pore drilling direction	z
Pore diameter (nm)	9.01606
Surface roughness (nm)	0.07548
Solvent reservoir z-dimension (nm)	
Pore volume (nm^3)	643.23398
Solvent reservoir volume (nm^3)	
Surface area (nm^2)	285.37239
Surface chemistry - Before Functionalization	
Number of single silanol groups	1060
Number of geminal silanol groups	142
Number of siloxane bridges	122
Total number of OH groups	1344
Overall hydroxylation (mumol/m^2)	7.82072
Surface chemistry - After Functionalization	
Number of C18 groups	433
C18 density (mumol/m^2)	2.51962
Number of C18G groups	67
C18G density (mumol/m^2)	0.38987
Number of TMS groups	107
TMS density (mumol/m^2)	0.62263
Number of TMSG groups	11
TMSG density (mumol/m^2)	0.06401
Bonded-phase density (mumol/m^2)	3.59613
Number of residual OH groups	726
Residual hydroxylation (mumol/m^2)	4.22458

	Exterior
Silica block xyz-dimensions (nm)	[16.19167, 15.78574, 10.07500]
Simulation box xyz-dimensions (nm)	[16.19167, 15.78574, 21.07500]
Pore drilling direction	
Pore diameter (nm)	
Surface roughness (nm)	0.00000
Solvent reservoir z-dimension (nm)	5.50000
Pore volume (nm^3)	
Solvent reservoir volume (nm^3)	2 * 1405.78671
Surface area (nm^2)	2 * 191.75302
Surface chemistry - Before Functionalization	

```
    Number of single silanol groups                          1700
    Number of geminal silanol groups                           53
    Number of siloxane bridges                                  0
    Total number of OH groups                                1806
    Overall hydroxylation (mumol/m^2)                     7.81996
Surface chemistry - After Functionalization
    Number of C18 groups                                      653
    C18 density (mumol/m^2)                               2.82748
    Number of C18G groups                                      19
    C18G density (mumol/m^2)                              0.08227
    Number of TMS groups                                      150
    TMS density (mumol/m^2)                               0.64950
    Number of TMSG groups                                       9
    TMSG density (mumol/m^2)                              0.03897
    Bonded-phase density (mumol/m^2)                      3.59822
    Number of residual OH groups                              975
    Residual hydroxylation (mumol/m^2)                    4.22174
```

At this point the pore generation is completed and what is left is converting the programs data structure into a readable file-format using the functionalities of the *Store* module. For this a store function is provided that creates a structure file in the GROMACS format, a main topology containing the number of atoms, a topology for the grid (silicon and oxygen) and basic surface groups (single and geminal silanol and siloxane bridges) and a pickle file of the pore object and pore system. The object files can be used to extract pore properties during later analysis

```
pore.store("output/rplc/")
```

For additional construction abilities e.g. choosing a different drilling axis or defining a different drilling inclination of the pore shape, we suggest using the delivered constructor classes as templates to construct more complex pore forms.

For further information, more thorough variable descriptions and functionalities like special placement of molecules, we refer to the documentation website of the GitHub repository.

A.2. An atomistic view on the uptake of aromatic compounds by cyclodextrin immobilized on mesoporous silica

Configuration files of the equilibrated pore and bulk systems, corresponding topologies and simulation parameter files are provided via the Data Repository of the University of Stuttgart (DaRUS) under

`https://doi.org/10.18419/darus-2154`.

A.2.1. Binding free energy calculated by rate constants

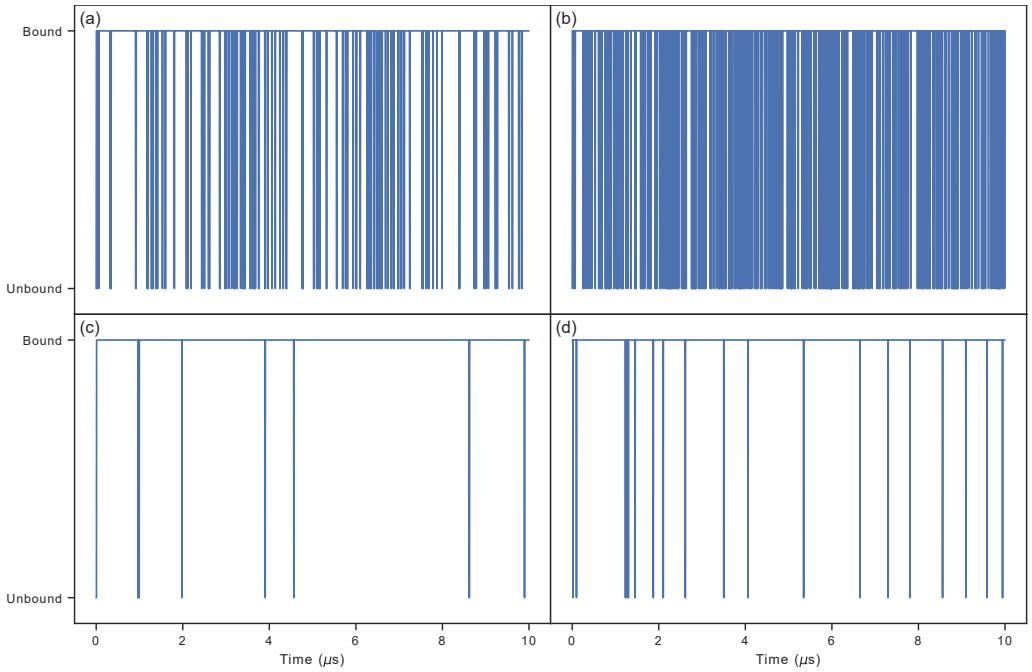

Figure A.2.1.: Bound and unbound instances over simulation time for (a), (b) benzene and (c), (d) *p*-nitrophenol at (a), (c) 298 K and (b), (d) 350 K.

Table A.2.1.: Binding free enthalpy ΔG (kJ mol^{-1}), association k_{on} (dm^3 mol^{-1} s^{-1}) and dissociation k_{off} (s^{-1}) rates at different temporal cut-offs (ps) for *p*-nitrophenol (pnp) and benzene (ben) at a temperature of T = 350 K. The chosen spatial cut-offs for differentiating between bound and unbound states was 0.7 nm for both guest molecules.

Cut-off	ΔG^{pnp}	k_{on}^{pnp}	k_{off}^{pnp}	ΔG^{ben}	k_{on}^{ben}	k_{off}^{ben}
0	-24.22	3.76e+10	9.11e+06	-14.11	7.61e+09	5.97e+07
100	-18.28	1.87e+09	3.50e+06	-14.71	1.50e+09	9.54e+06
200	-18.19	1.80e+09	3.47e+06	-14.49	1.36e+09	9.33e+06
300	-17.97	1.65e+09	3.44e+06	-14.34	1.26e+09	9.16e+06
400	-17.86	1.59e+09	3.43e+06	-14.19	1.19e+09	9.07e+06
500	-17.69	1.49e+09	3.42e+06	-14.08	1.12e+09	8.90e+06
600	-17.47	1.37e+09	3.40e+06	-13.93	1.06e+09	8.81e+06
700	-17.28	1.28e+09	3.39e+06	-13.79	9.92e+08	8.69e+06
800	-17.22	1.26e+09	3.38e+06	-13.68	9.47e+08	8.59e+06
900	-17.16	1.23e+09	3.38e+06	-13.58	9.01e+08	8.46e+06
1000	-17.01	1.16e+09	3.34e+06	-13.46	8.58e+08	8.41e+06

A.2.2. Biding free enthalpy calculated by double-decoupling

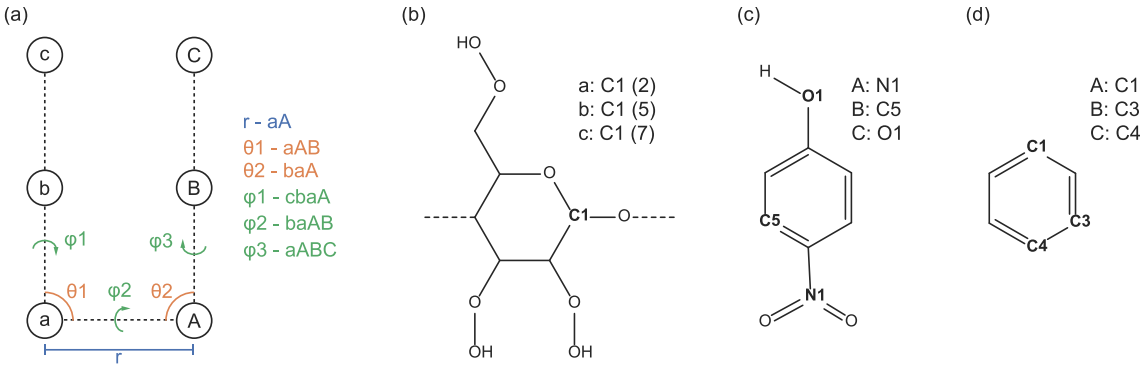

Figure A.2.2.: (a) Chosen restraint lengths, angles, and dihedrals according to Boresch and Karplus [1] with (b) chosen atoms of the cyclodextrin molecule, where the brackets denote the glucopyranose number, (c) chosen atoms of the *p*-nitrophenol ligand, and (d) chosen atoms of the benzene ligand.

Table A.2.2.: Binding free enthalpy $\Delta G^{\mathrm{M}}_{\mathrm{u}\to\mathrm{b}}$ (kJ mol^{-1}) calculated by double decoupling for β-cyclodextrin (bCD) with benzene (BEN) and *p*-nitrophenol (*p*-NP) respectively at two different temperatures T (K). Additionally, free enthalpy contributions along the thermodynamic cycle (Fig. 2, main text) are shown.

	T	$-\Delta G^{\mathrm{M}}_{\mathrm{hyd}}$	$-\Delta G^{\mathrm{M}}_{\mathrm{u}\to\mathrm{b}}$		$\Delta G^{\mathrm{M}\to\mathrm{M}'}_{\mathrm{b}\to\mathrm{tor}}$		$-\Delta G^{\mathrm{M}'}_{\mathrm{tor}}$	
			conf1	conf2	conf1	conf2	conf1	conf2
bCD+BEN	298	3.23	13.12		45.41		29.06	
	350	−0.10	12.15		44.73		32.68	
bCD+*p*-NP	298	35.35	24.09	23.42	87.28	86.58	27.84	27.81
	350	31.06	22.61	21.37	84.98	83.74	31.31	31.31

A.2.3. Cyclodextrin Parametrization for the Pore Surface

Parametrization of the cyclodextrin molecule connected to a silica surface as shown in Fig. 3 of the main text was carried out with AmberTools20 [2]. Silicon atoms which are not natively available in AmberTools, were exchanged with carbon atoms since both have similar bond parameters, and unsaturated atoms were saturated with hydrogen atoms. Additionally in the case of the structure used by Huq et al. (L1 linker), the ion bond of oxygen and sodium was replaced with a hydroxy group. In order to resemble the experimental [3] situation with an ionic linker balanced by a sodium cation, the hydrogen atom `H8` bound to `O1` was changed to a dummy atom and the negative partial charges of `O1`, `N2`, `N3`, `N4` of the tail structure and `O6` of the cyclodextrin were slightly increased in magnitude such that the entire structure beyond the `Si1`-atom has a net charge of −1.32 *e*. Similarly the charges of `N1`, `O1`, `C4` of the second linker [4] and

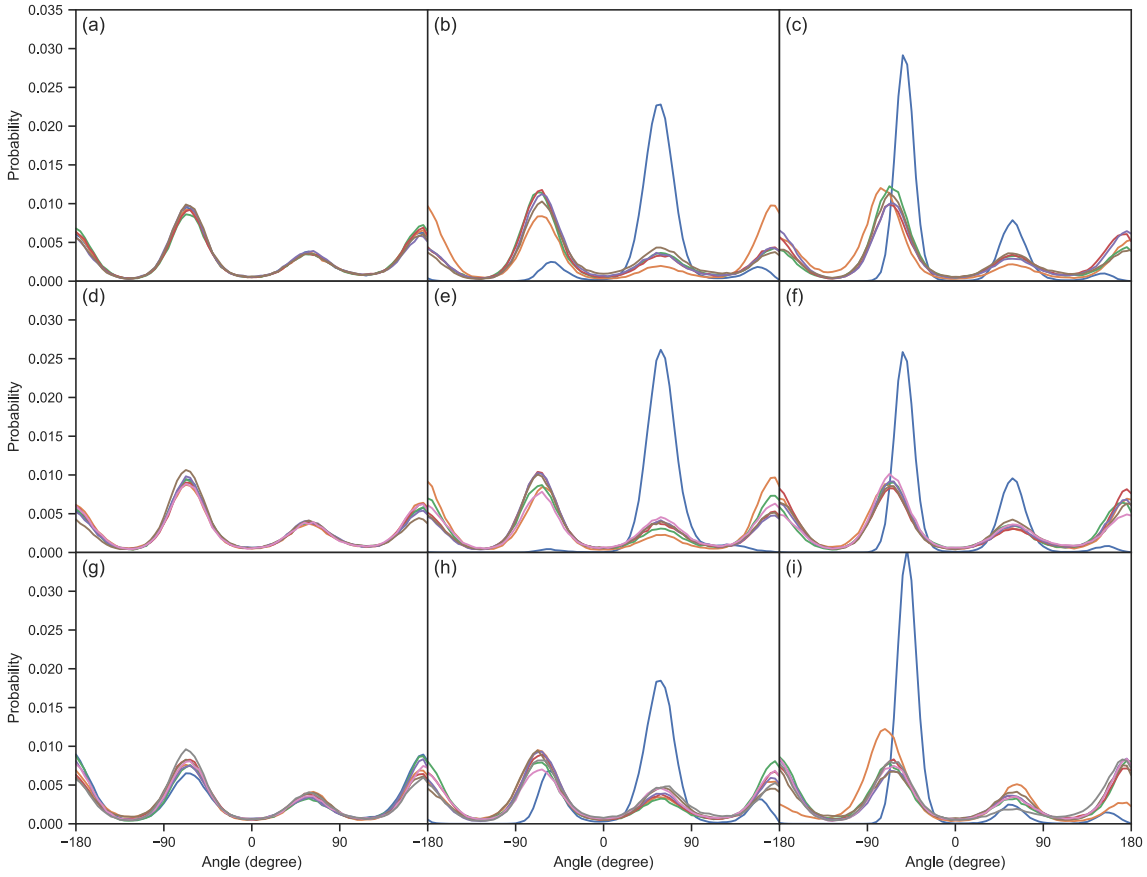

Figure A.2.3.: Distributions of the individual dihedral angles H6O-O6-C6-H61 for the native (a) α-, (d) β- and (g) γ-cyclodextrin. The different colours denote the different glucopyranose units. The second column shows the distribution of six dihedral angles H6O-O6-C6-H61 for (b) α-, (e) β- and (h) γ-cyclodextrin connected with the L1 linker[3]. The blue line represents the distribution of the C5(tail)-O6-C6-H61 dihedral angle. Analogously the third column shows the distributions for (c) α-, (f) β- and (i) γ-cyclodextrin but for the L2 linker[4] with the blue line representing the distribution of the C4(tail)-O6-C6-H61 dihedral angle.

O6 of the cyclodextrin were altered to compensate for the positive charge of 0.32 *e* induced by the silicon atom.

Table A.2.3.: Bond parameters with bond length b_0 (nm) and force constant k_b (kJ mol^{-1} nm^{-1}). Angle parameters with angle θ_0 (deg) and force constant k_θ (kJ mol^{-1} rad^{-2}). Dihedral parameters with angle ϕ_s (deg), force constant k_ϕ (kJ mol^{-1}) and multiplicity M. Column F denotes the corresponding GROMACS function type.

	Atom 1	Atom 2			F	b_0	k_b	
L1 [3]	C5-Tail	O6-CD			1	0.13696	315138.88	
L2 [4]	C4-Tail	O6-CD			1	0.13584	327021.44	
	Atom 1	Atom 2	Atom 3		F	θ_0	k_θ	
L1 [3]	N2-Tail	C5-Tail	O6-CD		1	119.72005	608.26992	
	C5-Tail	O6-CD	C6-CD		1	117.96005	523.16736	
	N4-Tail	C5-Tail	O6-CD		1	119.72005	608.26992	
L2 [4]	N1-Tail	C4-Tail	O6-CD		1	109.22005	630.27776	
	C4-Tail	O6-CD	C6-CD		1	115.98005	529.52704	
	O1-Tail	C4-Tail	O6-CD		1	123.25005	630.27776	
	Atom 1	Atom 2	Atom 3	Atom 4	F	ϕ_s	k_ϕ	M
L1 [3]	C4-Tail	N2-Tail	C5-Tail	O6-CD	1	180.00	20.08320	2
	N2-Tail	C5-Tail	O6-CD	C6-CD	1	180.00	3.76560	2
	C5-Tail	O6-CD	C6-CD	C5-CD	1	0.00	1.60387	3
	C6-Tail	N4-Tail	C5-Tail	O6-CD	1	180.00	20.08320	2
	N4-Tail	C5-Tail	O6-CD	C6-CD	1	180.00	3.76560	2
	C5-Tail	O6-CD	C6-CD	H61-CD	1	0.00	1.60387	3
	C5-Tail	O6-CD	C6-CD	H62-CD	1	0.00	1.60387	3
L2 [4]	C4-Tail	O6-CD	C6-CD	C5-CD	1	180.00	3.34720	1
	C4-Tail	O6-CD	C6-CD	C5-CD	1	0.00	1.60247	3
	O1-Tail	C4-Tail	O6-CD	C6-CD	1	180.00	5.85760	1
	O1-Tail	C4-Tail	O6-CD	C6-CD	1	180.00	11.2968	2
	N1-Tail	C4-Tail	O6-CD	C6-CD	1	180.00	11.2968	2
	H7-Tail	N1-Tail	C4-Tail	O6-CD	1	180.00	10.4600	2
	C3-Tail	N1-Tail	C4-Tail	O6-CD	1	180.00	10.4600	2
	C4-Tail	O6-CD	C6-CD	H61-CD	1	0.00	1.60387	3
	C4-Tail	O6-CD	C6-CD	H62-CD	1	0.00	1.60387	3

A.2.4. Grid Parameters for the Pore Simulation

Table A.2.4.: Lennard-Jones parameter and charges of the grid atoms (Si, O_{Si}) and silanol atoms (SI, O_H, H) as reported by Gulmen and Thompson [5].

Atom	σ (nm)	ϵ (kJ mol^{-1})	q ($\lvert e \rvert$)
Si	0.2500	0.000 418 4	1.28
O_{Si}	0.2700	1.912 088 0	−0.64
O_H	0.3070	0.711 280 0	−0.74
H	0.1295	0.001 530 1	0.42

A.2.5. Adsorption Isotherms

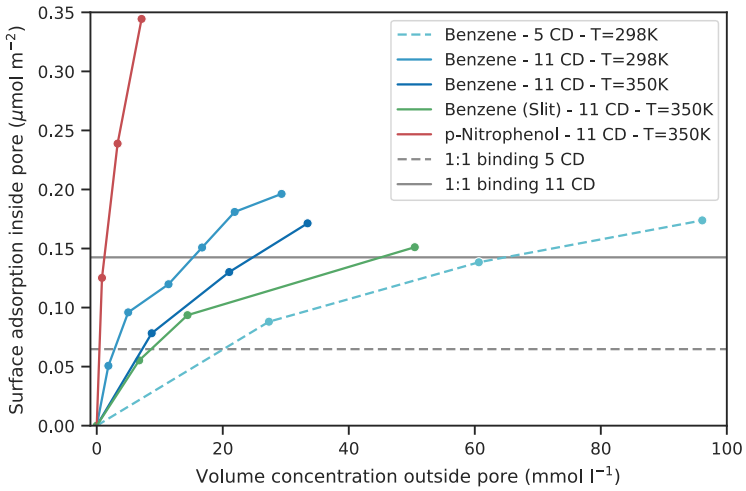

Figure A.2.4.: Excess adsorption isotherms of pore simulations utilizing the L2-variant [4] cyclodextrin functionalized surface with varying amounts of benzene in a cylindrical pore (blues) and a slit pore (green) and the L1-variant [3] cyclodextrin with p-nitrophenol (red). Simulation were run for 1 µs at temperatures $T = 298\,\mathrm{K}$ and $T = 350\,\mathrm{K}$, and a cyclodextrin surface amount of 5 molecules (dashed lines) and 11 molecules (solid lines) on the surface. The grey lines represent a hypothetical maximum of 1:1 binding with 5 (dashed line) and 11 (solid line) cyclodextrin molecules respectively.

A.3. Axial Diffusion in Liquid Saturated Cylindrical Silica Model Pores

A.3.1. Grid Parameters for the Pore Simulation

Table A.3.1.: Lennard-Jones parameter reported by Coasne et al. [6] and charges of the grid atoms (Si, O_{Si}) and silanol atoms (SI, O_H, H) as reported by Gulmen and Thompson [5].

Atom	σ (nm)	ϵ (kJ mol^{-1})	q ($\lvert e \rvert$)
Si	0.4550	0.167 869 3	1.28
O_{Si}	0.3210	0.957 353 5	−0.64
O_H	0.3210	0.957 353 5	−0.74
H	0.2750	0.112 189 9	0.42

A.3.2. Experimental data

The quality of the experimental density data at a temperature of $T_{295} = 295\,\mathrm{K}$ was evaluated by comparing neighboring temperatures due to a scarce amount of data for some components. Figure A.3.1 shows that the experimental data at T_{295} only have a slight deviation to the curve connecting the neighboring mean density values at T_{293} and T_{298}.

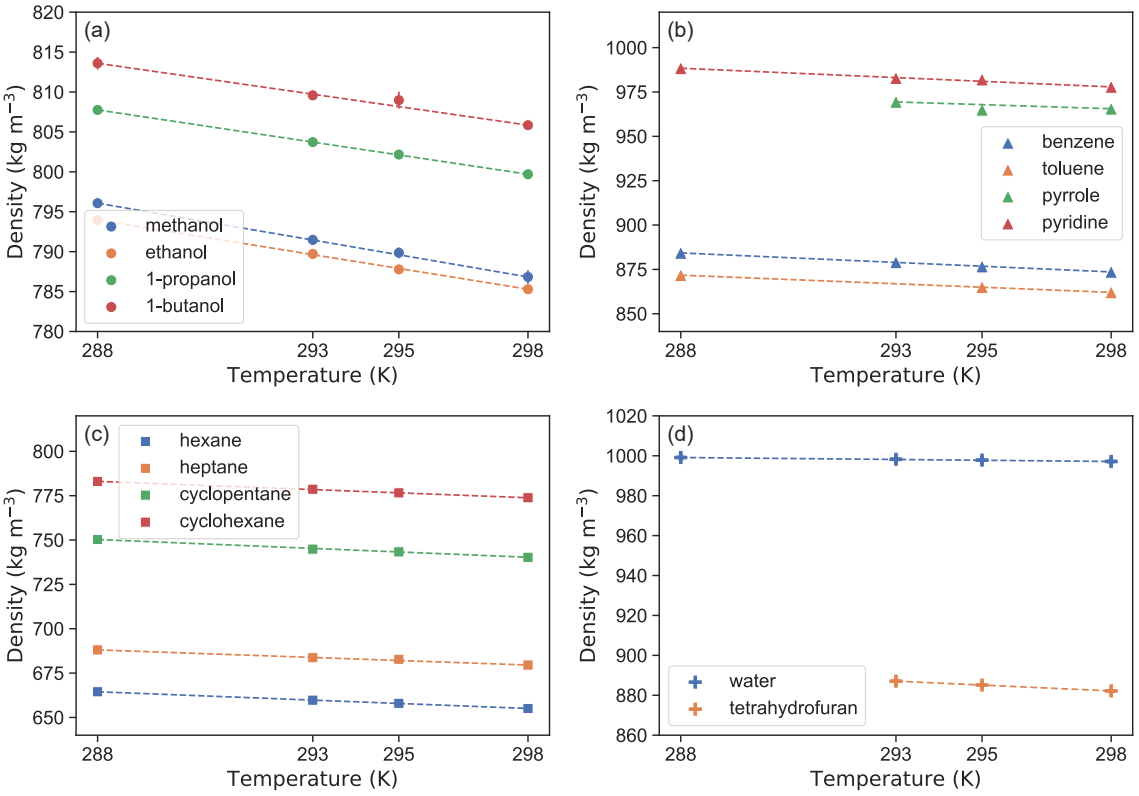

Figure A.3.1.: Visualization of experimental density data at different temperatures for (a) alcohols, (b) aromatics, (c) alkanes, and (d) water and tetrahydrofuran.

A comparison between the self diffusion coefficients determined by Agrawal et al.[7] and the average value from other references is made. The self diffusion coefficients at a temperature of T_{295} were partially interpolated between existing values in order to enable a comparison with Agrawal et al. [7]. Figure A.3.2 shows experimental the self diffusion coefficients at different temperatures for the molecules under consideration.

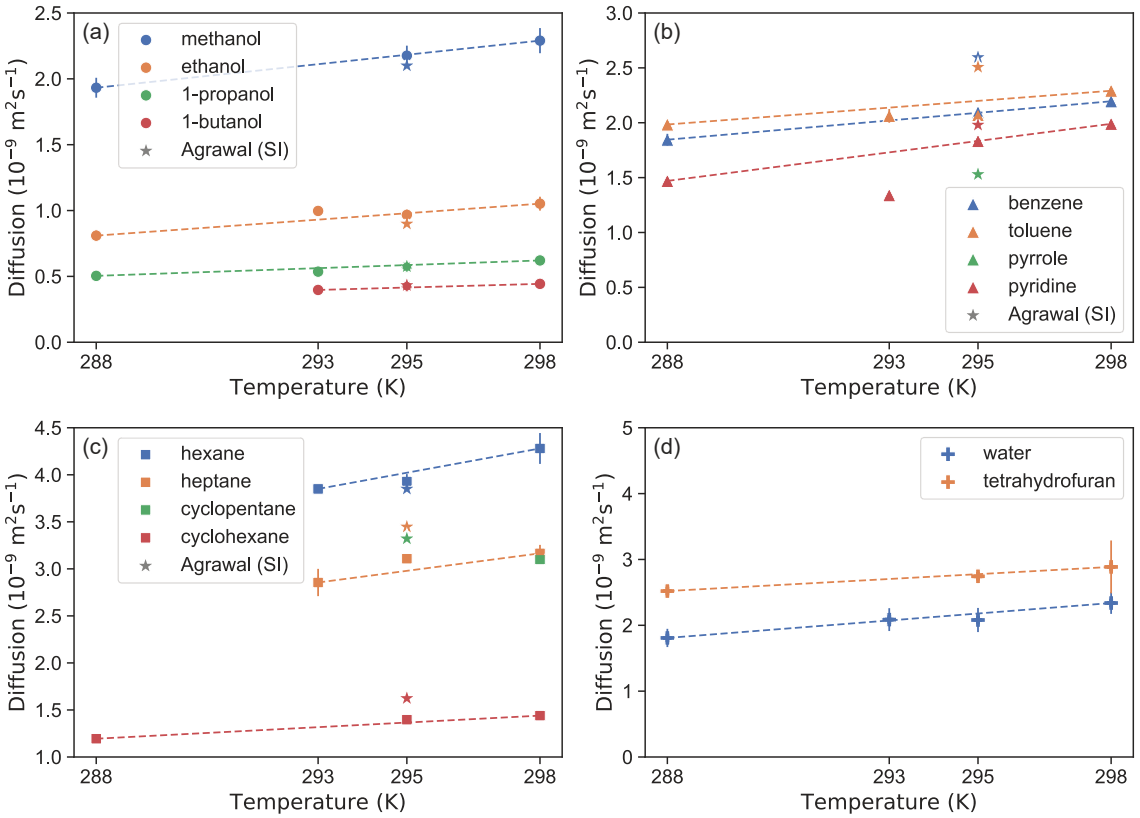

Figure A.3.2.: Visualization of experimental data of Agrawal et al. [7] (triangle) compared with other references (bullet) [8–22] at different temperatures for (a) alcohols, (b) aromatics, (c) alkanes, and (d) water and tetrahydrofuran.

It can be seen that the diffusion coefficients of Agrawal et al.[7] show a large deviation, especially for aromatics and alkanes. Therefore, the values from Agrawal et al.[7] were only included into the averaged value at T_{295} if for one the deviation to the other experimental values is reasonable, and if the coefficient does not exceed or fall below the experimental values at the higher and lower temperatures respectively. This is only the case for the alcohols. In case of the aromatics and alcohols, the diffusion coefficients from Agrawal et al.[7] are only considered for pyrrole and cyclopentane due to the lack of other experimental data at the target temperature.

A.3.3. Bulk Simulation - Diffusion Coefficients

Table A.3.2.: Self diffusion coefficients D ($10^{-9}\,m^2\,s^{-1}$) at a temperature of $T = 295\,K$ from MD simulations for different molecule numbers calculated using the Einstein equation (4) (E), and the Smoluchowski equation (7) (S). Due to dependence of the coefficients to the box size, the self-diffusion was extrapolated towards an infinite system size for both methods.

Number	Molecule	D_E^{NpT}	D_E^{NVT}	D_S	Molecule	D_E^{NpT}	D_E^{NVT}	D_S
1000	methanol	1.68	1.64	1.67	ethanol	0.49	0.49	0.59
5000		1.77	1.79	1.80		0.55	0.54	0.63
10 000		1.78	1.84	1.84		0.56	0.54	0.64
∞		1.88	2.01	1.99		0.62	0.59	0.69
1000	1-propanol	0.26	0.23	0.32	1-butanol	0.14	0.14	0.23
5000		0.26	0.26	0.35		0.15	0.15	0.24
10 000		0.26	0.26	0.36		0.15	0.15	0.23
∞		0.27	0.29	0.39		0.16	0.16	0.24
1000	benzene	2.03	1.96	1.98	toluene	1.89	2.00	2.00
5000		2.14	2.08	2.09		2.03	2.02	2.00
10 000		2.13	2.10	2.14		2.02	2.06	2.05
∞		2.24	2.24	2.27		2.16	2.08	2.06
1000	pyrrole	0.70	0.62	0.63	pyridine	1.10	1.11	1.15
5000		0.70	0.70	0.70		1.17	1.15	1.17
10 000		0.71	0.70	0.70		1.17	1.17	1.18
∞		0.71	0.79	0.78		1.24	1.22	1.20
1000	hexane	3.26	3.31	3.29	heptane	2.29	2.36	2.35
5000		3.48	3.52	3.52		2.49	2.50	2.56
10 000		3.46	3.47	3.47		2.52	2.54	2.57
∞		3.68	3.67	3.70		2.74	2.68	2.79
1000	cyclopentane	2.71	2.76	2.80	cyclohexane	1.24	1.25	1.26
5000		2.87	2.94	2.95		1.31	1.29	1.30
10 000		2.94	2.95	2.96		1.32	1.37	1.36
∞		3.14	3.14	3.13		1.40	1.44	1.42
2000	water	1.98	1.94	1.98	tetrahydro-	1.63	1.60	1.61
4000	(tip4p2005)	2.01	2.03	2.03	furan	1.65	1.64	1.63
8000		2.06	2.05	2.05	(GAFF2)	1.65	1.61	1.65
∞		2.21	2.25	2.17		1.69	1.65	1.72

A.3.4. Bulk Simulation - Somulchowski Approach

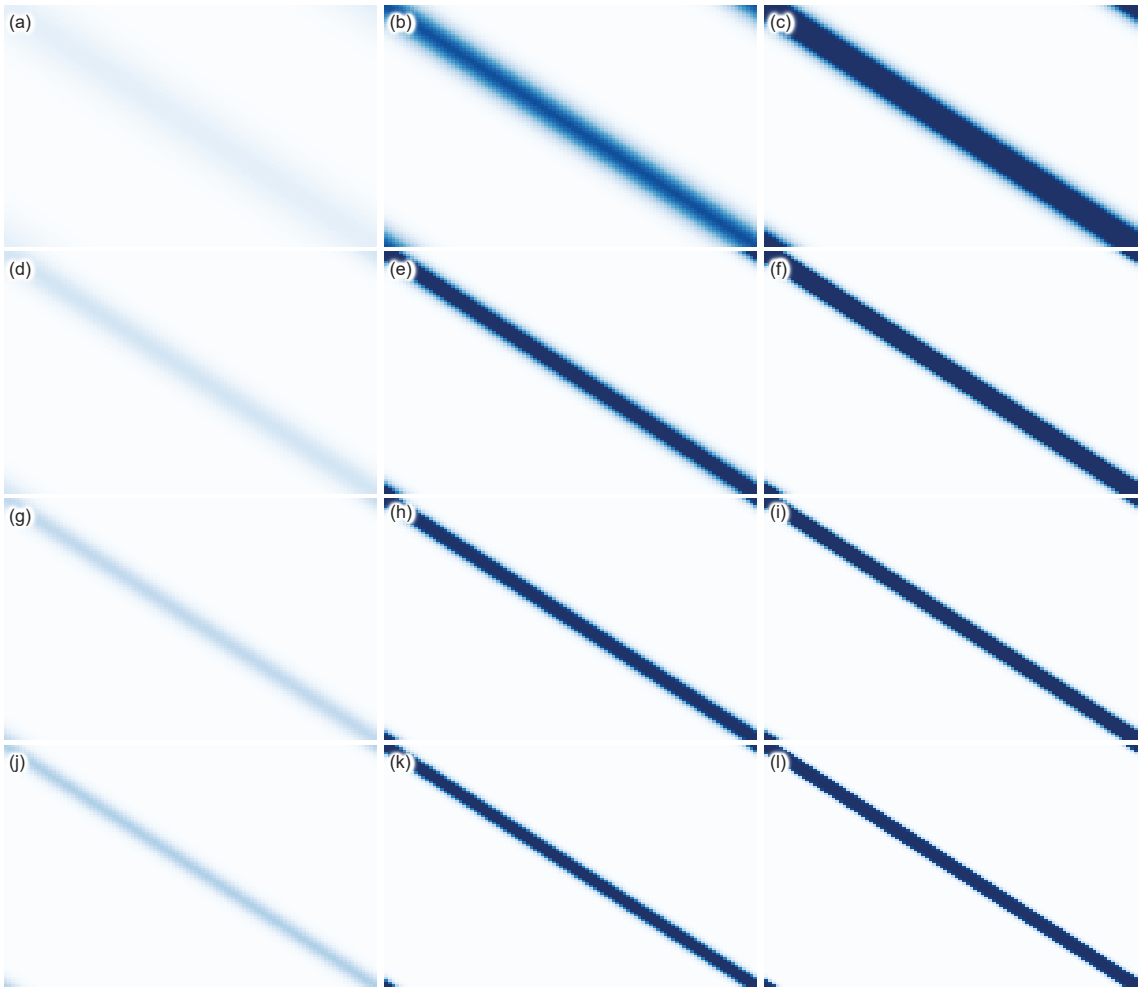

Figure A.3.3.: Visualization of the transition matrix for a lag time of 20 ps of simulations with (a, d, g, j) 1000 molecules, (b, e, h, k) 5000 molecules and (c, f, i, l) 10000 molecules for (a, b, c) methanol, (d, e, f) ethanol, (g, h, i) 1-propanol and (j, k, l) 1-butanol.

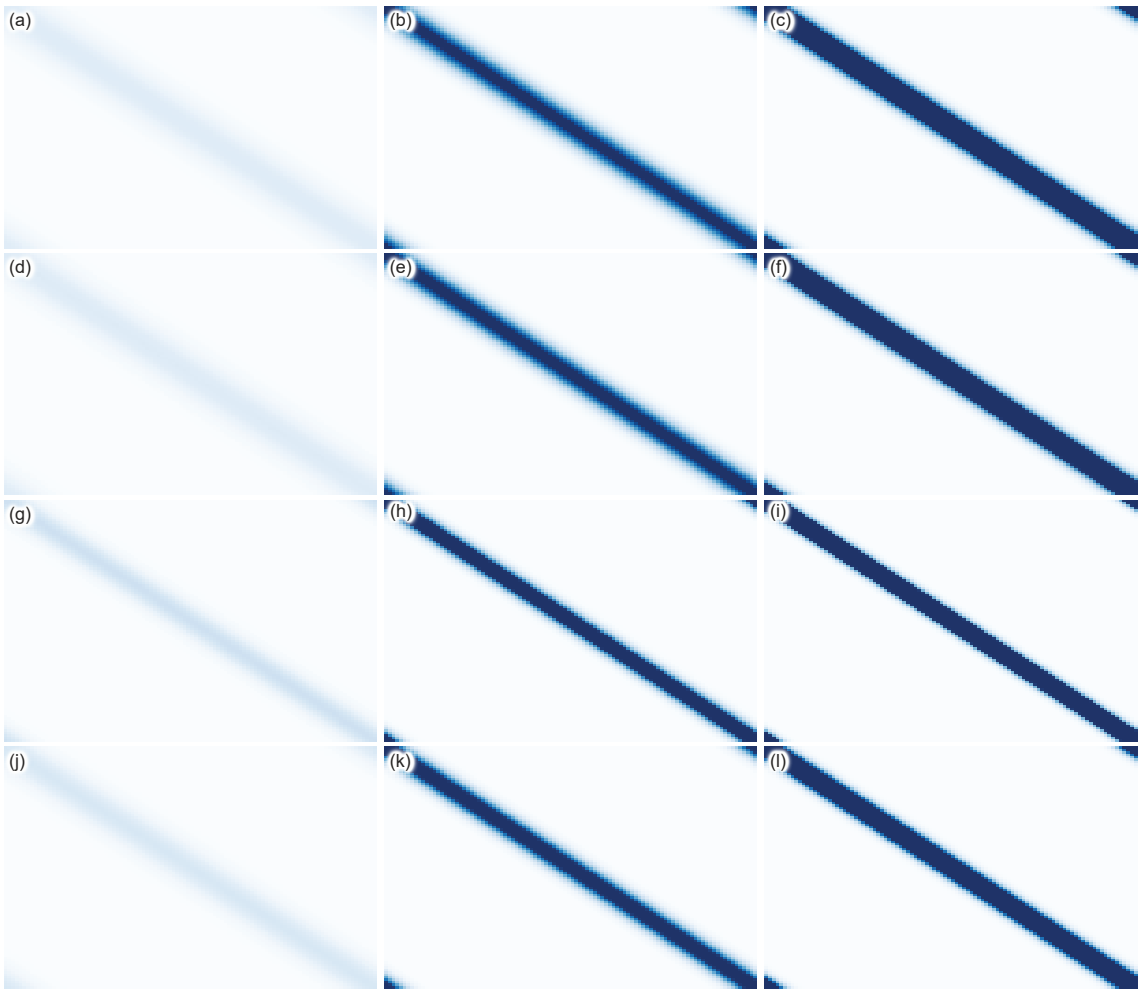

Figure A.3.4.: Visualization of the transition matrix for a lag time of 20 ps of simulations with (a, d, g, j) 1000 molecules, (b, e, h, k) 5000 molecules and (c, f, i, l) 10000 molecules for (a, b, c) benzene, (d, e, f) toluene, (g, h, i) pyrrole and (j, k, l) pyridine.

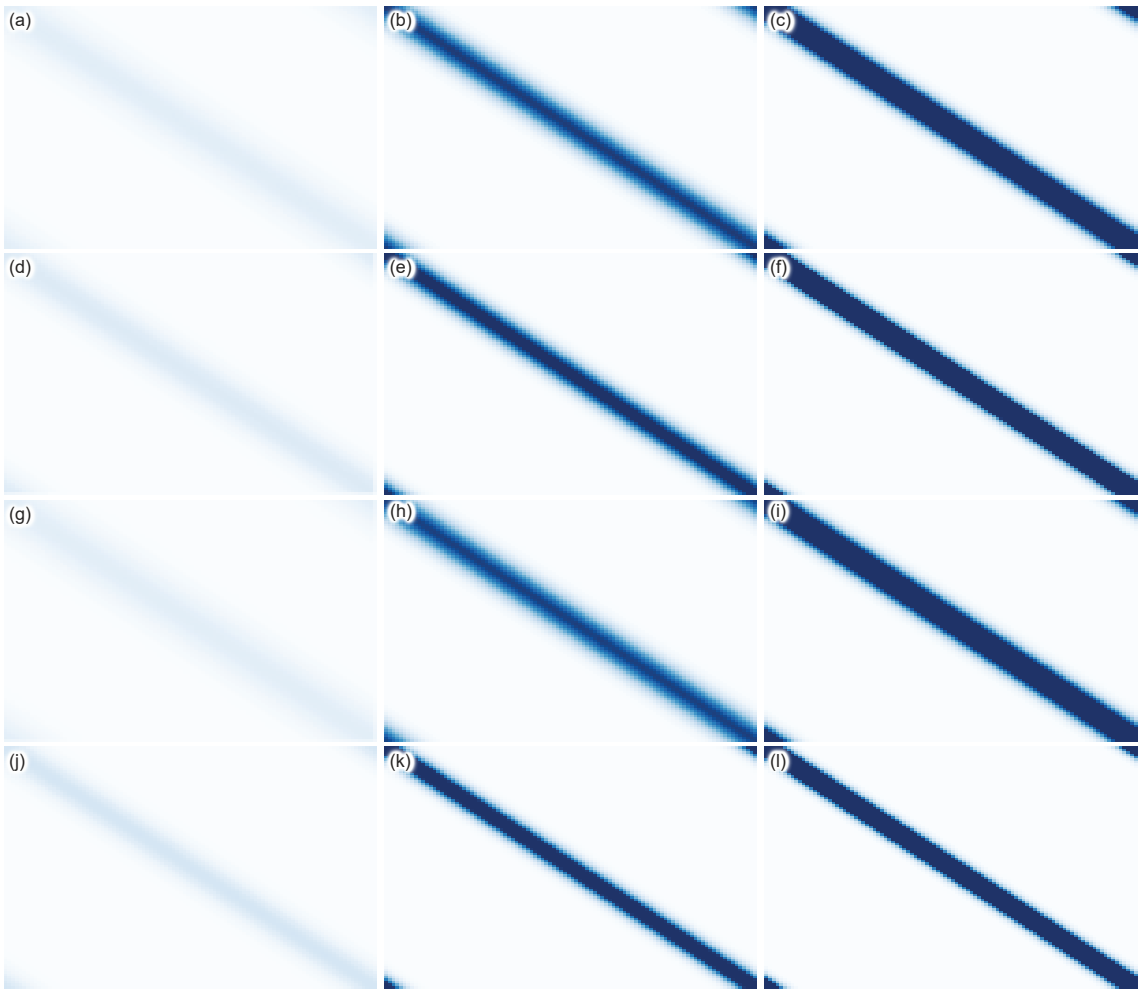

Figure A.3.5.: Visualization of the transition matrix for a lag time of 20 ps of simulations with (a, d, g, j) 1000 molecules, (b, e, h, k) 5000 molecules and (c, f, i, l) 10000 molecules for (a, b, c) hexane, (d, e, f) heptane, (g, h, i) cyclopentane and (j, k, l) cyclohexane.

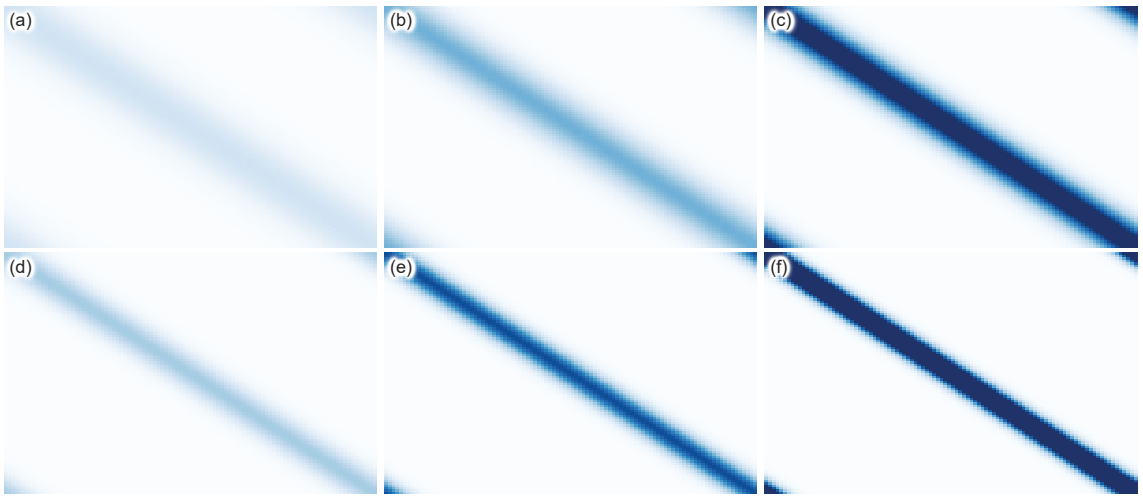

Figure A.3.6.: Visualization of the transition matrix for a lag time of 20 ps of simulations with (a, d) 1000 molecules, (b, e) 5000 molecules and (c, f) 10000 molecules for (a, b, c) water and (d, e, f) tetrahydrofuran.

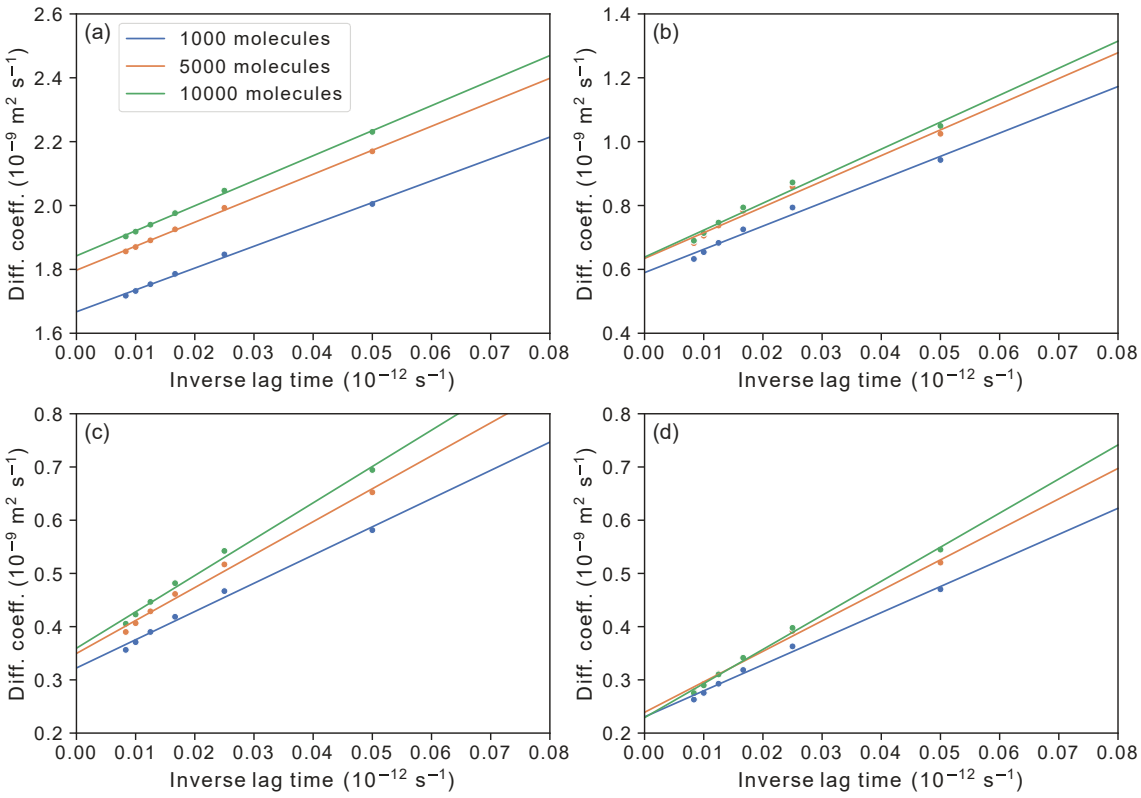

Figure A.3.7.: Visualization of the extrapolation of the self-diffusion coefficients for different system sizes towards an infinite lag time for (a) methanol, (b) ethanol, (c) 1-propanol and (d) 1-butanol.

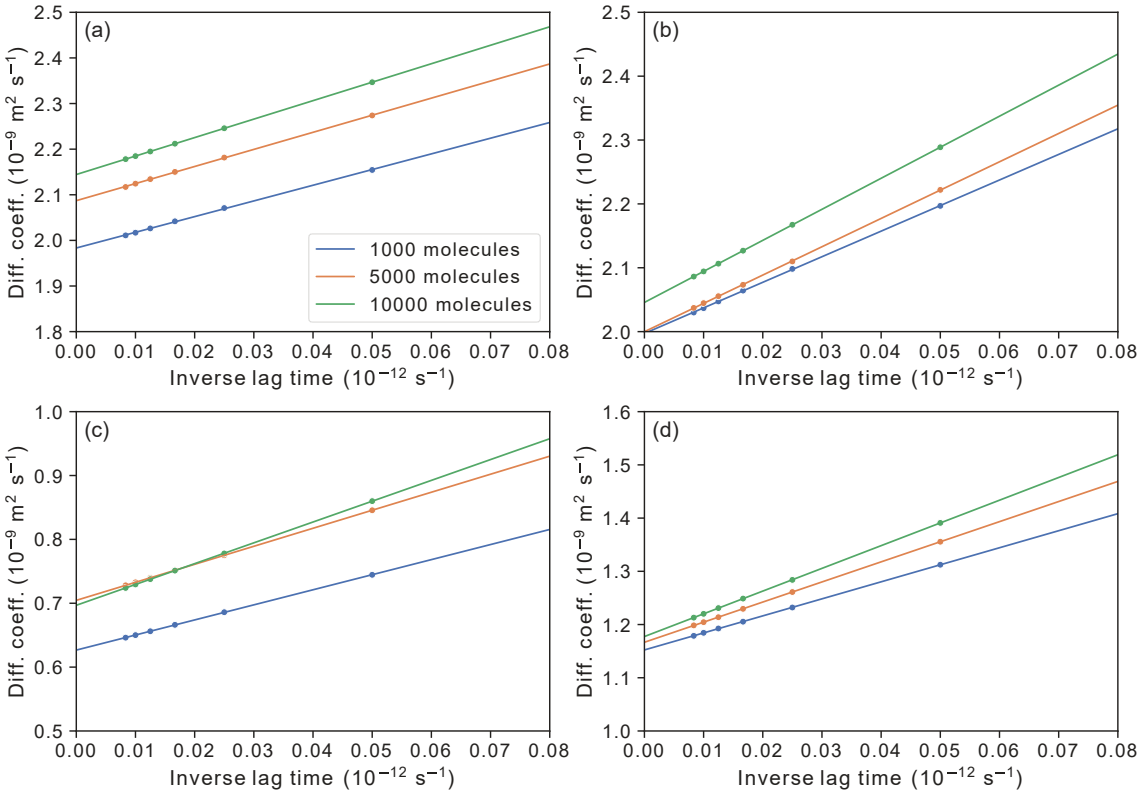

Figure A.3.8.: Visualization of the extrapolation of the self-diffusion coefficients for different system sizes towards an infinite lag time for (a) benzene, (b) toluene, (c) pyrrole and (d) pyridine.

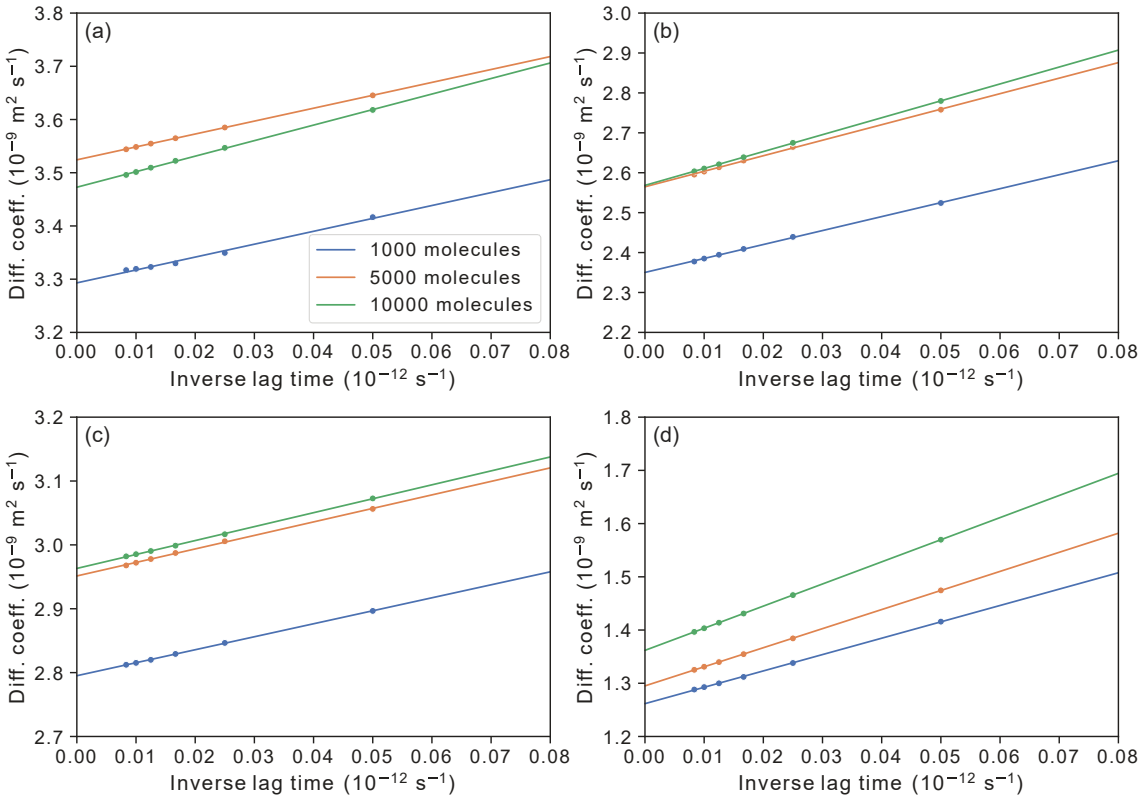

Figure A.3.9.: Visualization of the extrapolation of the self-diffusion coefficients for different system sizes towards an infinite lag time for (a) hexane, (b) heptane, (c) cyclopentane and (d) cyclohexane.

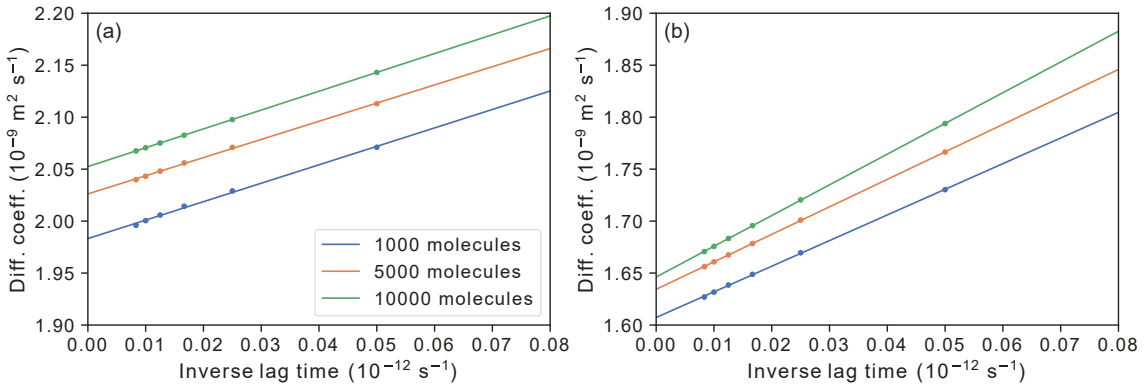

Figure A.3.10.: Visualization of the extrapolation of the self-diffusion coefficients for different system sizes towards an infinite lag time for (a) water and (b) tetrahydrofuran.

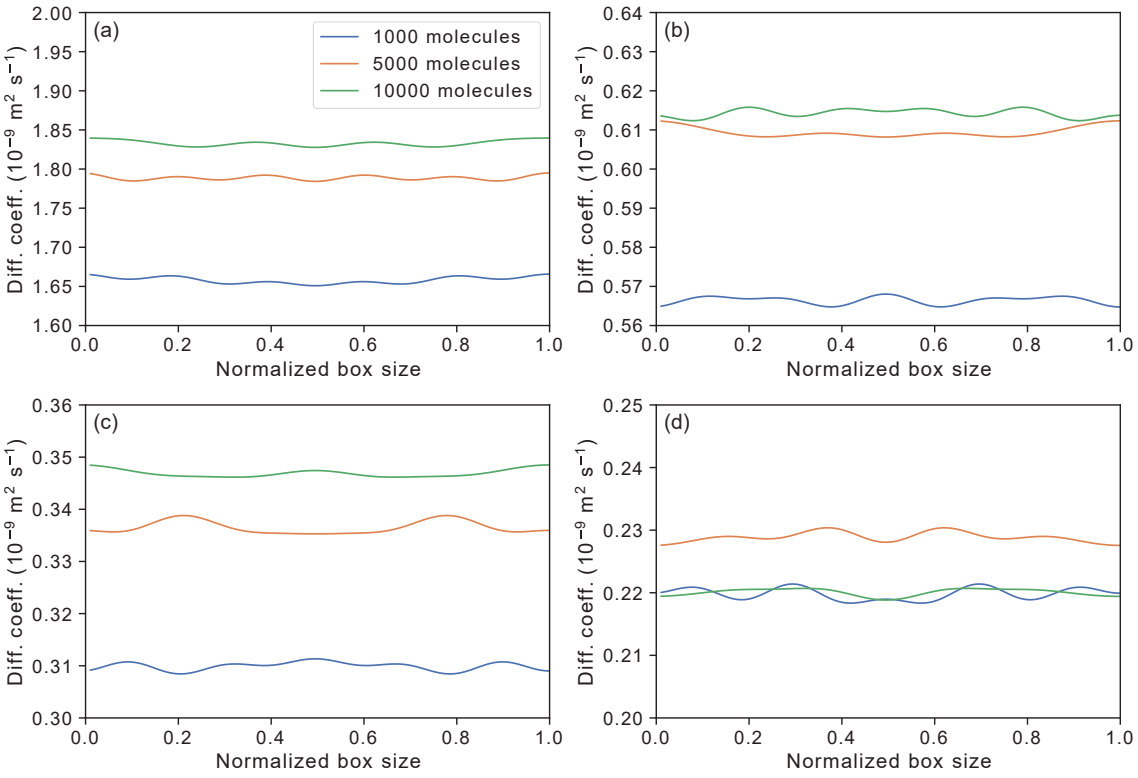

Figure A.3.11.: Visualization of the diffusion profile along the simulation box for different system sizes for (a) methanol, (b) ethanol, (c) 1-propanol and (d) 1-butanol.

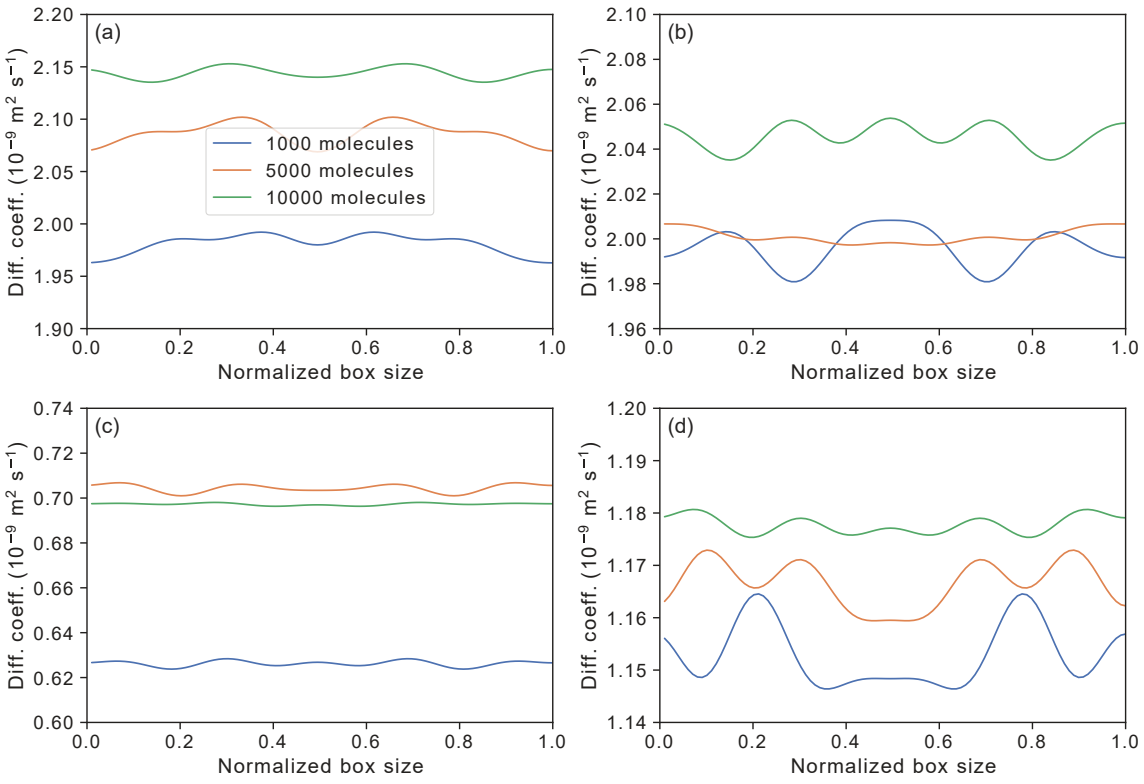

Figure A.3.12.: Visualization of the diffusion profile along the simulation box for different system sizes for (a) benzene, (b) toluene, (c) pyrrole and (d) pyridine.

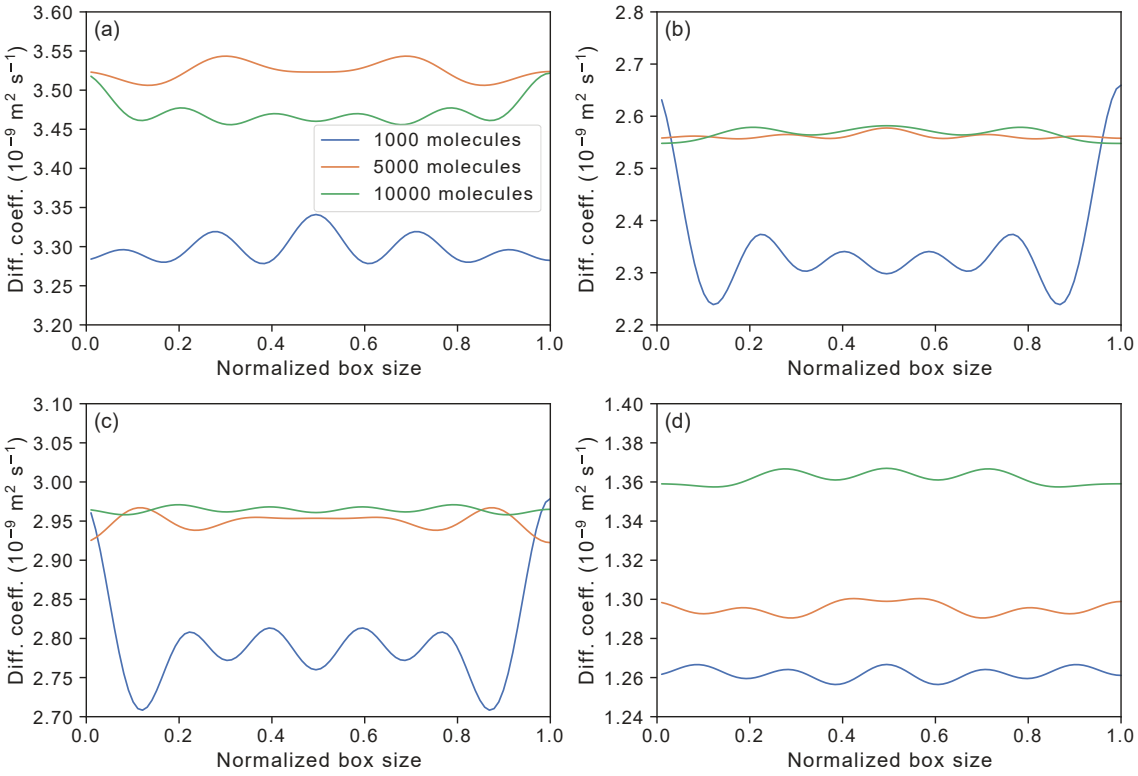

Figure A.3.13.: Visualization of the diffusion profile along the simulation box for different system sizes for (a) hexane, (b) heptane, (c) cyclopentane and (d) cyclohexane.

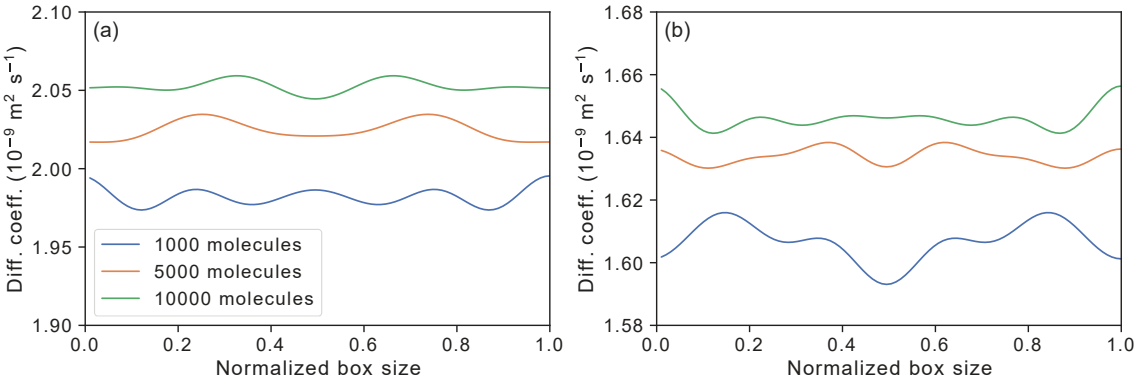

Figure A.3.14.: Visualization of the diffusion profile along the simulation box for different system sizes for (a) water and (b) tetrahydrofuran.

A.3.5. Bulk Simulations - Elongated system

Due to finite size effects, the diffusion coefficient varies with different dimensions of simulation systems. In addition, Vögele and Hummer showed that by considering a rectangular system where one side longer than the other two, the diffusion coefficient in that longer side is significantly lower [23]. Analogously, the same effect would be visible in a pore system, which has a similar composition. Therefore, the pore diffusion in the reservoir area, calculated by the Smoluchowski method in one direction, should be compared to the similar one dimension coefficient of pure solution with the same system size.

Table A.3.3.: Density ρ ($\mathrm{kg\,m^{-3}}$) and diffusion coefficient D ($10^{-9}\,\mathrm{m^2\,s^{-1}}$) of NVT simulations at a temperature of $T = 295\,\mathrm{K}$, of a cubic system (cubic) and a rectangular system (rect) calculated by the Einstein method (E) and the Smoluchowski method (S). The diffusion was calculated as a mean value of all dimensions and extrapolated towards an infinite system size. The z superscript, denotes the diffusion coefficient only for the longer side (z-dimension) of the rectangular system.

Molecule	ρ_{cubic}	ρ_{rect}	$D_{\mathrm{cubic,E}}$	$D_{\mathrm{cubic,S}}$	$D_{\mathrm{rect,E}}$	$D^{z}_{\mathrm{rect,E}}$	$D^{z}_{\mathrm{rect,S}}$
methanol	787.90	788.24	2.01	1.99	1.94	1.77	1.75
ethanol	792.55	792.50	0.59	0.69	0.58	0.54	0.63
1-propanol	799.33	799.04	0.29	0.39	0.27	0.25	0.36
1-butanol	803.30	803.11	0.16	0.24	0.16	0.15	0.22
benzene	867.58	868.82	2.24	2.27	2.30	2.06	2.02
toluene	851.57	849.56	2.08	2.06	2.09	1.91	1.98
pyrrole	1000.37	999.67	0.79	0.78	0.77	0.70	0.69
pyridine	988.26	987.74	1.22	1.20	1.24	1.17	1.13
hexane	665.99	666.68	3.67	3.70	3.64	3.31	3.28
heptane	691.56	691.81	2.68	2.79	2.68	2.43	2.38
cyclopentane	743.21	743.52	3.14	3.13	3.10	2.83	2.84
cyclohexane	772.35	772.78	1.44	1.42	1.38	1.29	1.24
water	997.83	997.93	2.25	2.17	2.14	2.05	2.03
tetrahydrofuran	887.09	887.89	1.65	1.72	1.78	1.62	1.56

The compound diffusion coefficients (mean value of all dimensions) shown in table A.3.3, is consisted for the cubic and rectangular system. The slight difference can be accounted to the small difference in density. The diffusion of the longer side of the rectangular system is much lower than the mean value, which is consistent with the observation of Vögele and Hummer [23]. A visual comparison of the effect of elongated boxes can be seen in figure A.3.15.

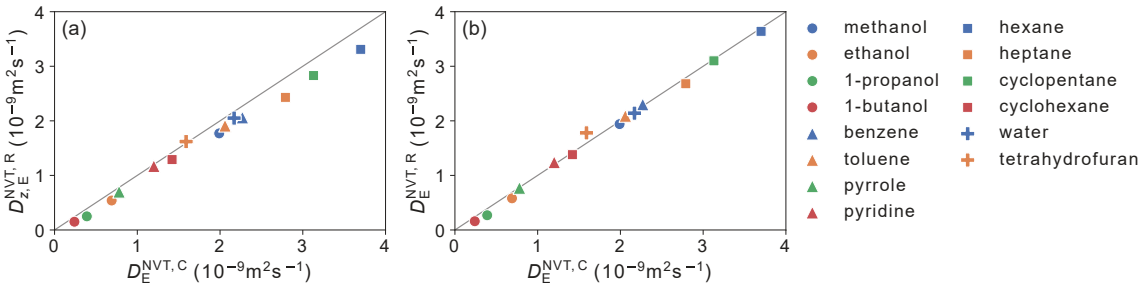

Figure A.3.15.: Correlation of diffusion coefficient D (10^{-9} m^2 s^{-1}) calculated in a cubic (cubic) and rectangular (rect) box calculated using the Einstein method for alcohols (methanol, ethanol, 1-propanol, 1-butanol) (circle), aromatics (benzene, toluene, pyrrole, pyridine) (triangle), alkanes (hexane, heptane, cyclopentane cyclohexane) (square), and water and tetrahydrofuran (plus). (a) Comparison of the compound diffusion with the one dimensional diffusion, and (b) comparison of the compound diffusion of both cubic and rectangular systems.

A.3.6. Pore Simulation - Density

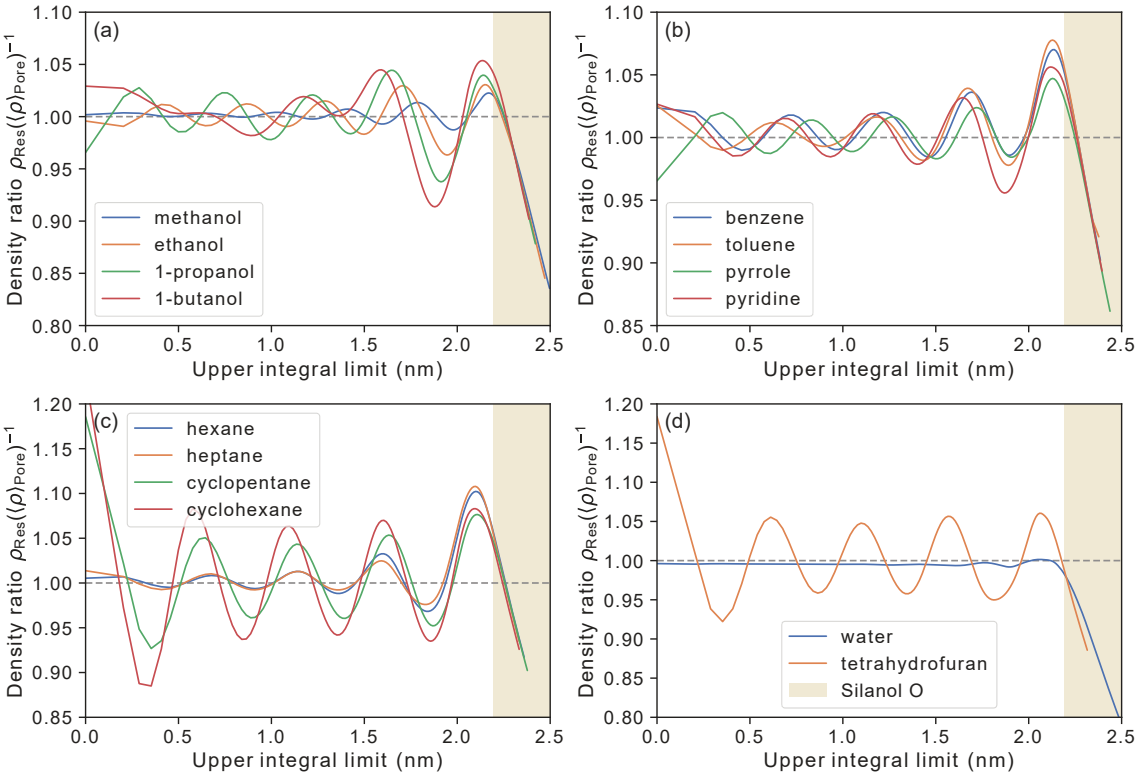

Figure A.3.16.: Integration of the radial density profiles over the radius within the pore divided by the reservoir density of (a) methanol, ethanol, 1-propanol, 1-butanol, (b) benzene, toluene, pyrrole, pyridine, (c) hexane, heptane, cyclopentane cyclohexane, and (d) water and tetrahydrofuran. The shaded area denotes the configurational space of the silanol oxygen atoms.

Table A.3.4.: Maximal ratio of the integrated pore density ρ_{Pore} ($\mathrm{kg\,m^{-3}}$) and the reservoir density ρ_{Res} ($\mathrm{kg\,m^{-3}}$) of the pore simulation from figure A.3.16. The integration cut-off for reaching the Gibbs dividing interface, i.e. a ratio of zero, is listed under r_{int} (nm). In addition, the radius of gyration R_{gyr} (nm) of the different molecules, determined from the bulk simulation is shown.

Molecule	$\left(\frac{\rho_{\mathrm{Pore}}}{\rho_{\mathrm{Res}}}\right)^{\mathrm{max}}_{\mathrm{Sim}}$	r_{int}	R_{gyr}
methanol	1.02	2.255	0.085
ethanol	1.03	2.250	0.120
1-propanol	1.04	2.255	0.152
1-butantol	1.05	2.265	0.186
benzene	1.07	2.265	0.151
toluene	1.08	2.265	0.177
pyrrole	1.05	2.255	0.128
pyridine	1.06	2.265	0.147
hexane	1.10	2.265	0.217
heptane	1.11	2.265	0.244
cyclopentane	1.19	2.265	0.143
cyclohexane	1.23	2.250	0.161
water	1.00	2.100	0.031
tetrahydrofuran	1.18	2.180	0.138

A.3.7. Pore Simulation - Somulchowski Approach

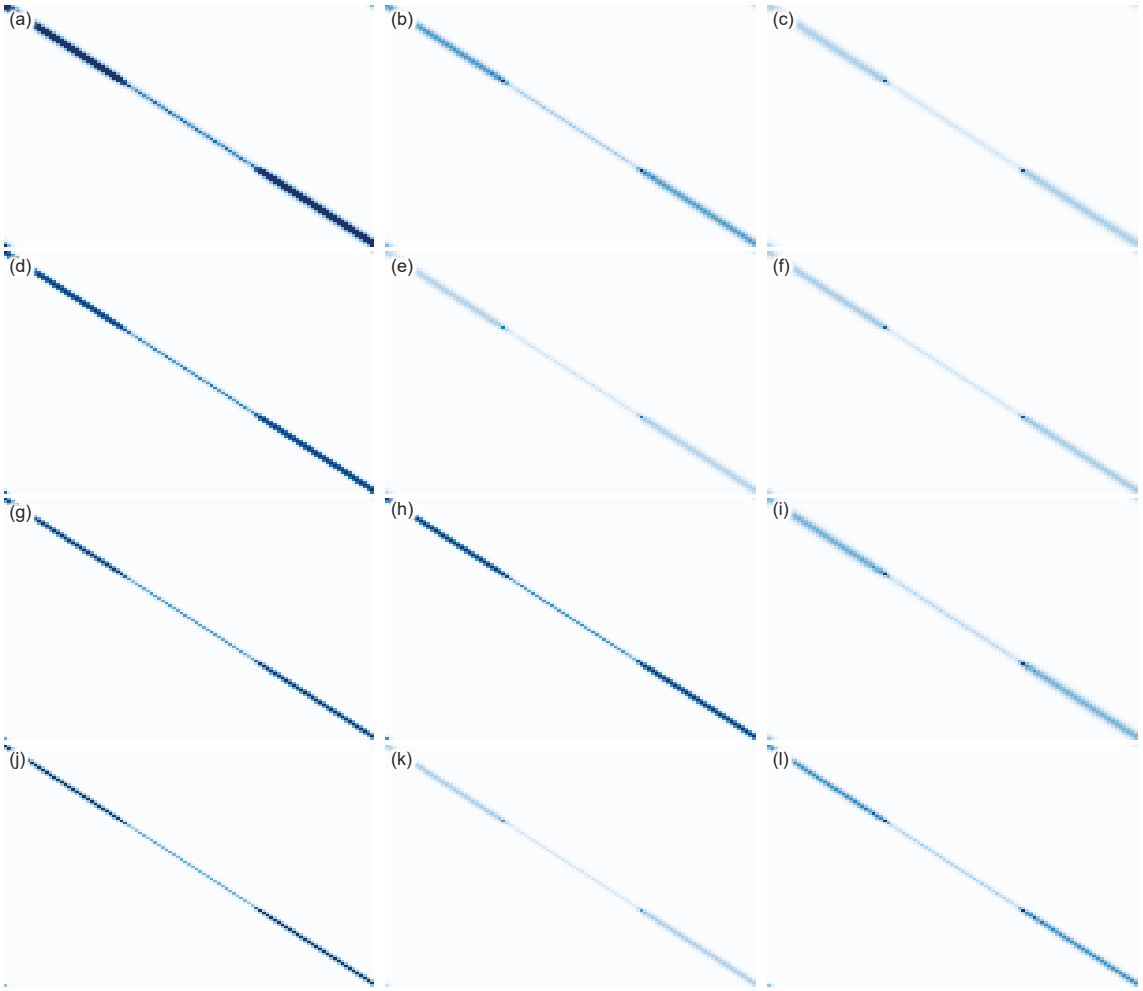

Figure A.3.17.: Visualization of the transition matrix for a lag time of 20 ps of pore simulation simulations with alcohols - (a) methanol, (d) ethanol, (g) 1-propanol, and (j) 1-butanol - aromatics - (b) benzene, (e) toluene, (h) pyrrole, and (k) pyridine - and alkanes - (c) hexane, (f) heptane, (i) cyclopentane, and (l) cyclohexane.

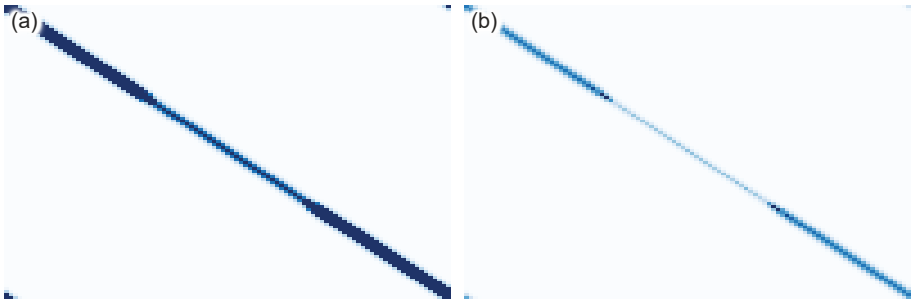

Figure A.3.18.: Visualization of the transition matrix for a lag time of 20 ps of pore simulation simulations with (a) water and (b) tetrahydrofuran.

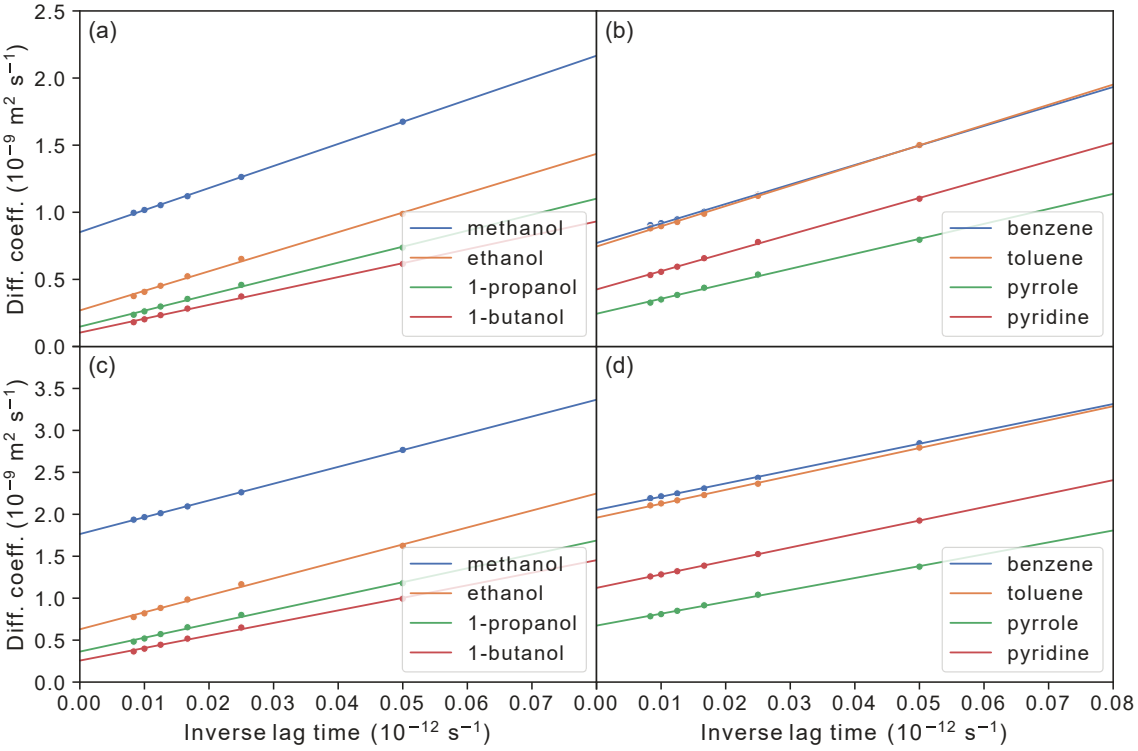

Figure A.3.19.: Visualization of the extrapolation of the self-diffusion coefficients for different system sizes towards an infinite lag time for (a, c) alcohols and (b, d) aromatics within (a, b) the pore section and (c, d) the bulk phase.

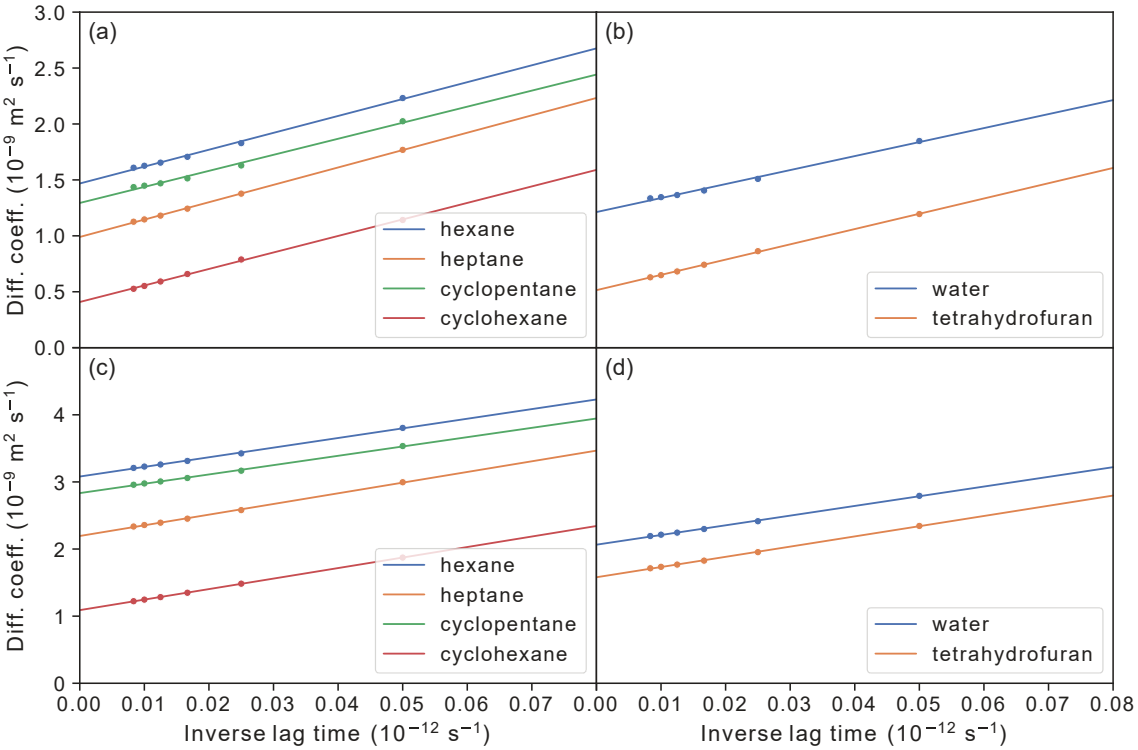

Figure A.3.20.: Visualization of the extrapolation of the self-diffusion coefficients for different system sizes towards an infinite lag time for (a, c) alkanes and (b, d) water and tetrahydrofuran within (a, b) the pore section and (c, d) the bulk phase.

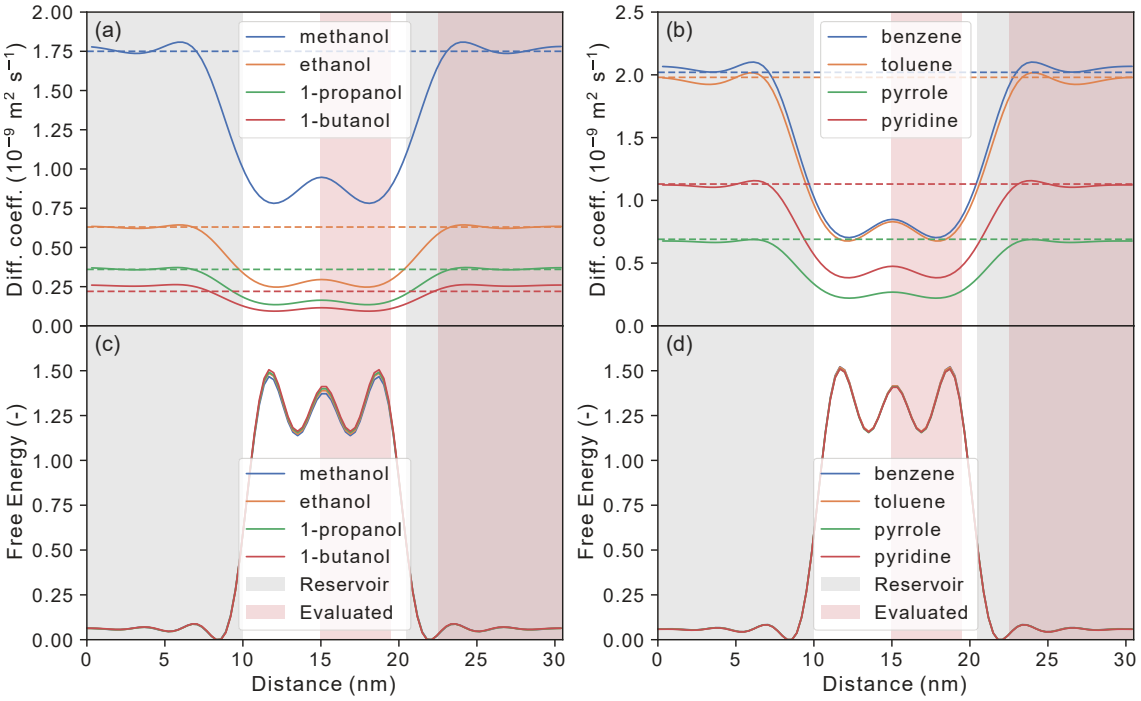

Figure A.3.21.: Visualization of the (a, b) diffusion profile and (c, d) free energy profile along the simulation box for (a, c) alcohols and (b, d) aromatics. Shaded areas mark the evaluated (red) and reservoir (gray) areas.

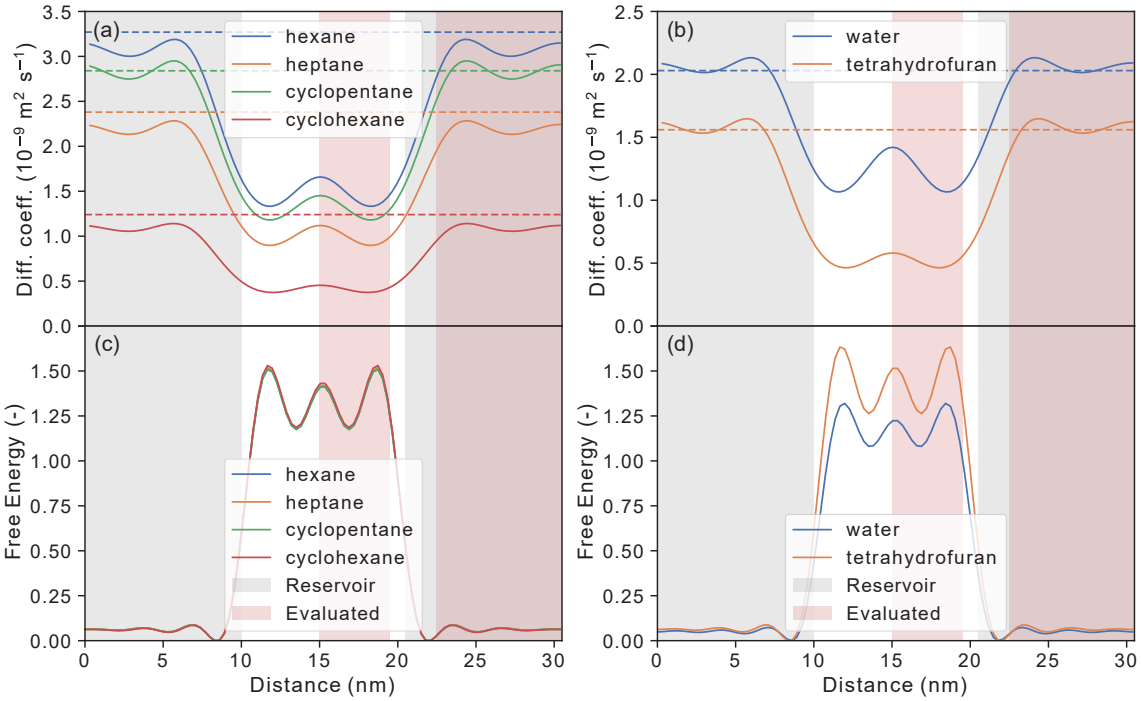

Figure A.3.22.: Visualization of the (a, b) diffusion profile and (c, d) free energy profile along the simulation box for (a, c) alkanes and (b, d) water and tetrahydrofuran. Shaded areas mark the evaluated (red) and reservoir (gray) areas.

A.3.8. Pore Simulation - Diffusion comparison

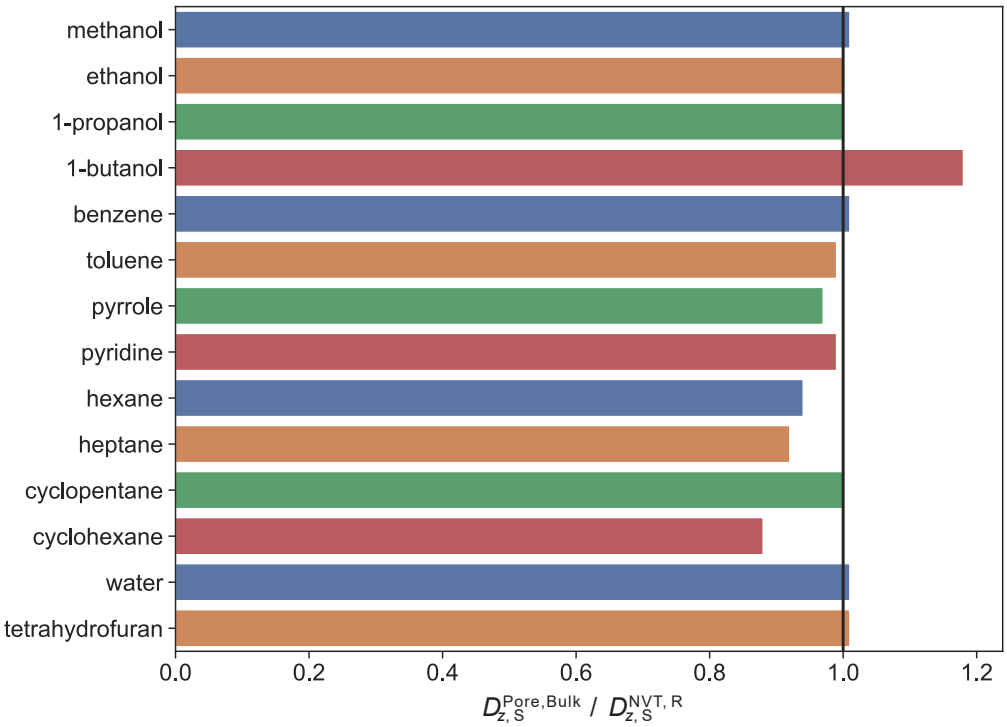

Figure A.3.23.: Comparison of the axial diffusion coefficients (D) within the bulk phase of the pore simulations and the diffusion from the NVT simulations of a rectangular (R) simulation box of the same dimensions. The axial diffusion was determined along the z-axis using the Smoluchowski (S) method.

References

[1] S. Boresch et al. “Absolute Binding Free Energies: a Quantitative Approach for Their Calculation”. In: *J. Phys. Chem. B* 107.35 (2003), pp. 9535–9551. DOI: 10.1021/jp0217839.

[2] D. A. Case et al. *AMBER 2020*. 2020.

[3] R. Huq, L. Mercier, and P. J. Kooyman. “Incorporation of Cyclodextrin into Mesostructured Silica”. In: *Chem. Mater.* 13.12 (2001), pp. 4512–4519. DOI: 10.1021/cm010171i.

[4] I. Trofymchuk, N. Roik, and L. Belyakova. “Structural Variety and Adsorptive Properties of Mesoporous Silicas with Immobilized Oligosaccharide Groups”. In: *Nanoscale Res. Lett.* 12.1 (2017), p. 307. DOI: 10.1186/s11671-017-2072-2.

[5] T. S. Gulmen and W. H. Thompson. “Testing a Two-State Model of Nanoconfined Liquids: conformational Equilibrium of Ethylene Glycol in Amorphous Silica Pores”. In: *Langmuir* 22.26 (2006), pp. 10919–10923. DOI: 10.1021/la062285k.

[6] B. Coasne and J. T. Fourkas. “Structure and Dynamics of Benzene Confined in Silica Nanopores”. In: *J. Phys. Chem. C* 115.31 (2011), pp. 15471–15479. DOI: 10.1021/jp203831q. (Visited on 06/14/2021).

[7] S. Agrawal, M. Elmehlawy, and M. P. Hoepfner. “Effect of confinement on the density and diffusivity of organic molecules in single-digit nanopores relative to bulk fluid behavior”. In: *J. Phys. Chem. C* 125.20 (2021), pp. 11097–11106. DOI: 10.1021/acs.jpcc.1c00159.

[8] D. Collins and H. Watts. “Viscosity and self-diffusion in benzene-cyclohexane mixtures”. In: *Aust. J. Chem.* 17.5 (1964), p. 516. DOI: 10.1071/CH9640516.

[9] A. F. Collings and R. Mills. “Temperature-dependence of self-diffusion for benzene and carbon tetrachloride”. In: *T. Faraday Soc.* 66 (1970), p. 2761. DOI: 10.1039/tf9706602761.

[10] *Dortmund Data Bank*. www.ddbst.com. 2018.

[11] N. K. Gaisin. “Investigation of molecular motion in liquid toluene by the spin echo method on deuterated samples”. In: *J. Struct. Chem+* 12.6 (1972), pp. 899–906. DOI: 10.1007/BF00744152.

[12] K. R. Harris. “Temperature and density dependence of the self-diffusion coefficient of n-hexane from 223 to 333 K and up to 400 MPa”. In: *J. Chem. Soc.* 78.7 (1982), p. 2265. DOI: 10.1039/f19827802265.

[13] H. Hiraoka et al. “Self-diffusion of methanol under pressure”. In: *Rev. Phys. Chem. Jpn.* 28.2 (1958), pp. 61–63.

[14] H. Hiraoka, J. Osugi, and W. Jono. “Self-diffusion of benzene and diffusions of sulfur and iodine in benzene under pressure”. In: *Rev. Phys. Chem. Jpn.* 28.2 (1958), pp. 52–60.

[15] M. Holz et al. “Experimental study of dynamic isotope effects in molecular liquids: detection of translation-rotation coupling”. In: *J. Chem. Phys.* 104.2 (1996), pp. 669–679. DOI: 10.1063/1.470863.

[16] M. A. McCool, A. F. Collings, and L. A. Woolf. “Pressure and temperature dependence of the self-diffusion of benzene”. In: *J. Chem. Soc.* 68.0 (1972), p. 1489. DOI: 10.1039/f19726801489.

[17] J. W. Moore and R. M. Wellek. “Diffusion coefficients of n-heptane and n-decane in n-alkanes and n-alcohols at several temperatures”. In: *J. Chem. Eng. Data* 19.2 (1974), pp. 136–140. DOI: 10.1021/je60061a023.

[18] J. R. Partington, R. F. Hudson, and K. W. Bagnall. “Self-diffusion of aliphatic alcohols”. In: *Nature* 169.4301 (1952), pp. 583–584. DOI: 10.1038/169583a0.

[19] W. S. Price, H. Ide, and Y. Arata. “Solution dynamics in aqueous monohydric alcohol systems”. In: *J. Phys. Chem. A* 107.24 (2003), pp. 4784–4789. DOI: 10.1021/jp027257z.

[20] R. E. Rathbun and A. L. Babb. “Self-diffusion in liquids. III. temperature dependence in pure liquids”. en. In: *J. Phys. Chem.* 65.6 (1961), pp. 1072–1074. DOI: 10.1021/j100824a520.

[21] P. S. Tofts et al. “Test liquids for quantitative MRI measurements of self-diffusion coefficient in vivo”. In: *Magn. Reson. Med.* 43.3 (2000), pp. 368–374. DOI: 10.1002/(SICI)1522-2594(200003)43:3<368::AID-MRM8>3.0.CO;2-B.

[22] K. Graupner and E. R. S. Winter. “Some measurements of the self-diffusion coefficients of liquids”. In: *J. Chem. Soc.* 0 (1952), pp. 1145–1150. DOI: 10.1039/JR9520001145. (Visited on 10/08/2021).

[23] M. Vögele and G. Hummer. “Divergent Diffusion Coefficients in Simulations of Fluids and Lipid Membranes”. In: *J. Phys. Chem. B* 120.33 (2016), pp. 8722–8732. DOI: 10.1021/acs.jpcb.6b05102.